FABRICATION AND CHARACTERIZATION OF OPTICAL SLAB AND CHANNEL WAVE-GUIDES BY ION EXCHANGE

BY

JAMES D. REID, B. ENG. (CONCORDIA)

Department of Electrical Engineering
McGill University, Montreal

A thesis submitted to the Faculty of Graduate Studies and Research in partial fulfillment of the requirements for the degree of

Master of Engineering

FABRICATION AND CHARACTERIZATION OF OPTICAL WAVEGUIDES BY ION EXCHANGE

ELECTRICAL JAMES D. REID, B. Eng. (CONCORDIA) M. ENG.

ABSTRACT

Slab guides, channel guides and related devices formed by the ion-exchange process are promising integrated optical structures, in that they can be fabricated simply and economically.

This thesis is concerned with the analysis and fabrication of slab and channel waveguides, made by ion exchange in either $AgNO_3$, dilute $AgNO_3$ or KNO_3 salt melts. A tutorial presentation of the exchange mechanism is given, and theoretical calculations involving the characterization of the resulting inhomogeneous guides in terms of their refractive index profile and dispersive properties have been performed. The analytical methods employed in the characterization were based on the well-known WKB approximation method, as well as the more exact staircase approximation.

Theoretical design considerations of channel guides and of a directional coupler fabricated by the ion exchange process are also included. These structures form the fundamental building blocks in integrated optics.

Experimental work has also been carried out in order to (I) characterize slab guides exchanged in $AgNO_3$, dilute $AgNO_3$ and KNO_3, and (II) fabricate channel guides exchanged in dilute $AgNO_3$ and KNO_3. Reasonably good agreements have been obtained between the theoretical calculations and experimental model index measurements for the slab guides.

RESUME

Les dispositifs tels les guides d'onde planaires, les guides d'ondes en canaux, et autres qui sont fabriqués à partir d'un procédé d'échange d'ions, sont prometteurs puisque cette méthode est simple et peu onéreuse.

Le sujet de cette thèse est l'analyse et la fabrication des guides d'onde planaires et en canaux fabriqués par échange d'ions dans des solutions salines de $AgNO_3$, de $AgNO_3$ dilué ou de KNO_3. La physique des mécanismes d'échange est présentée ainsi que les calculs théoriques concernant la caractérisation des propriétés inhomogènes des guides résultants, c'est-à-dire le profil de l'indice de réfraction et les propriétés de dispersion.

Les méthodes analytiques utilisées pour la caractérisation sont basées sur la méthode WKB bien connue et aussi la méthode plus exacte d'approximation en escalier.

L'analyse des guides d'ondes en canaux est aussi incluse. Ces structures sont reconnues comme étant les structures fondamentales en optique intégrée.

Des expérience ont aussi été menées dans le but de (I) Caractériser les guides d'onde planaires fabriqués dans l'$AgNO_3$, l'$AgNO_3$ dilué, et le KNO_3, (II) fabriquer des guides d'onde en canaux dans les solutions d'$AgNO_3$ diluées et de KNO_3.

L'écart entre les résultats théoriques et les résultats obtenus expérimentalement est satisfaisant, dans le cas des guides d'ondes planaires.

ACKNOWLEDGEMENTS

I would like to acknowledge the guidance extended to me by my supervisor, Dr. G.L. Yip.

I am also deeply grateful for the help I received from Dr. J. Finak and Mr. M. Bélanger. Their kind patience and suggestions helped me overcome many obstacles directly related to the realization of this thesis.

In appreciation of the support and encouragement of my friends and collegues, I would like to specifically acknowledge Mr. J.F. Ostiguy, Dr. I. Shih, Mr. H. Ibisoglu, Mr. D. Kiddie, Mr. G. Gizmopoloud, Mr. O. Avellanada and Mr. M. Yao.

Mr. J. Feldvari and his staff were instrumental in assisting me in the installation of the ion exchange apparatus, and their technical expertise is gratefully acknowledged.

I would also like to thank Caroline and my family for their encouragement and understanding, and I dedicate this work to them.

The research reported here was supported by an NSERC strategic grant (1980-1981) as well as an NSERC regular operating grant (1980-1983).

TABLE OF CONTENTS

CHAPTER I

INTRODUCTION

1.1 Overview

The field of integrated optics has been intensely pursued by researchers, since its conception in 1969. S.E. Miller (1), one of the founders of the concept of "miniature laser circuits" in the form of dielectric waveguides, proposed several integrated optical devices based on one fundamental circuit element; the channel guide. In his introductory paper, he outlined the photoli[redacted] process involved in the fabrication of channel guides, and then provided models for a laser, an electrooptic phase modulator, a directional coupler and several filters, all of which have been experimentally realized in laboratories, world-wide.

Following suit, in the same year that Miller coined the phrase "integrated optics", E. Marcatilli (2) presented his theoretical considerations on channel guides and directional couplers while J.E. Goell (3) developed a circular-harmonic computer analysis of dielectric channel guides. It was evident from the papers presented in this era, that integrated optical circuitry would penetrate

the signal processing domain, and eventually vie with micro-electronics on various levels; spectral analysis, optical signal communication and even computer hardware.

This thesis is concerned with dielectric slab and channel guides formed by the ion exchange process. Having discussed the origins of this field, consider the ion exchange process, a process which is fundamental to this thesis.

1.2 Ion-exchange

Ion-exchange is a process which has been under investigation for many decades. One of the earliest studies dates back to 1910, when Schulze (4) examined the diffusion of silver ions into glass from a silver nitrate melt (a eutectic mixture of $AgNO_3$ and $NaNO_3$). This process has been utilized by the glass manufacturers for the strengthening of glassware and was studied in this light by Burggraaf and Cornelissen (5). R. Doremus (6) derived relations between various parameters involved in the interdiffusion of two ions in glass and stated "When a common soft glass is placed into a melt or solution containing monovalent ions, these ions exchange with the sodium ions in the glass".

The first reported investigation into refractive index changes produced in glass by ion exchange was carried out by French and Pearson (7) in 1969. This study was fundamental in the conception of light guiding by the ion exchange process, and applications such as the production of glass fibers with a high index core and low index cladding were suggested. One of the earlier reports on the use of ion exchange for the formation of optical slab waveguides was made by Giallorenzi et al (8) in 1972. They obtained low loss guides with high index guiding films by exchanging in silver, potassium and thallium melts. Following these preliminary observations, many studies were performed on ion exchanged waveguides. Exhaustive investigations have been carried out on silver ion exchanged guides (9-12) as well as the examination of the effects of melt dilution (13), field assisted exchanges (14,15) and Li-K eutectics for fast fabrication (16).

1.3 Chapter Synopsis

Following this introductory chapter, the fundamentals of the ion exchange mechanism are introduced in Chapter II and the process is shown to behave much as a diffusion process (6,9). Solutions to the concentration dependent diffusion equation are presented (17), and the theory

behind diluted melts (13) is discussed.

Chapter III provides theoretical insight into inhomogeneous slab waveguides with discussions on the methods employed by Kirchoff (18), Marcuse (19), Yip & Colombini (20) while the main treatment is based on work by Brekhovskikh (21) This chapter also includes the WKB method for refractive index profiling of inhomogeneous slab guides (22) as well as two methods for determining the dispersion characteristics of graded index slab guides; (1) a WKB analysis based on Hocker and Burns (23) and (2) the step-approximation method (20).

Experimental fabrication procedures and results for ion-exchanged slab guides are covered in Chapter IV. The necessary apparatus, preparation conditions, fabrication steps and measurement processes are discussed. The refractive index profile for all data including $AgNO_3$, dilute $AgNO_3$ and KNO_3 melts under conditions of varying temperature and time are presented along with a comparison of theoretical and experimental dispersion curves.

Chapter V covers channel waveguides by ion exchange. Some theoretical results based on work by Marcatilli (2) are included and are compared to results derived by the effective index method (24,25). The dispersion characteris-

ties are plotted for typical KNO_3-exchanged channel guides with an aspect ratio of 2 and hence both of the above-mentioned methods are shown to be in good agreement. Selected field plots of the transverse electric fields are included and experimental results and procedures for obtaining various channel configurations are presented. Most of the discussions are based on work by Hocker & Burns (25), Hocker (26), Simova et al (27) and Gallagher (28).

Finally, in Chapter VI, the conclusion is reached and some general discussions about the work done and future investigations are considered.

In addition, a number of aspects, although quite pertinent to this study, were nevertheless better treated as appendices, are attached (diffusion theory, discussions on computer software, derivation of the profiling equation, use of Newton's Rings for alignment etc.).

CHAPTER II

THE ION EXCHANGE MECHANISM

2.1 Introduction

Reports on the study or use of ion exchange date back to the late nineteen fiftys where this mechanism was employed to strengthen glass by placing the surface under tension. The basic analysis of this mechanism was presented by Burggraff (5) (glass strengthening) and by Doremus (6) (diffusion approach).

Essentially, the ion exchange or migration mechanism is a diffusion process. When a common soft glass such as a soda-lime composition is placed into a melt or solution containing monovalent ions, these ions exchange with the sodium ions in the glass (Fig. 2.1). The rate at which this process proceeds is controlled by the diffusion of the ions from the melt into the glass and vice versa. Any ions leaving the ion exchanger (glass substrate) are replaced by an equivalent amount of counter ions from the melt, in keeping with the electroneutrality requirement.

It is a well established fact (6) that ions from

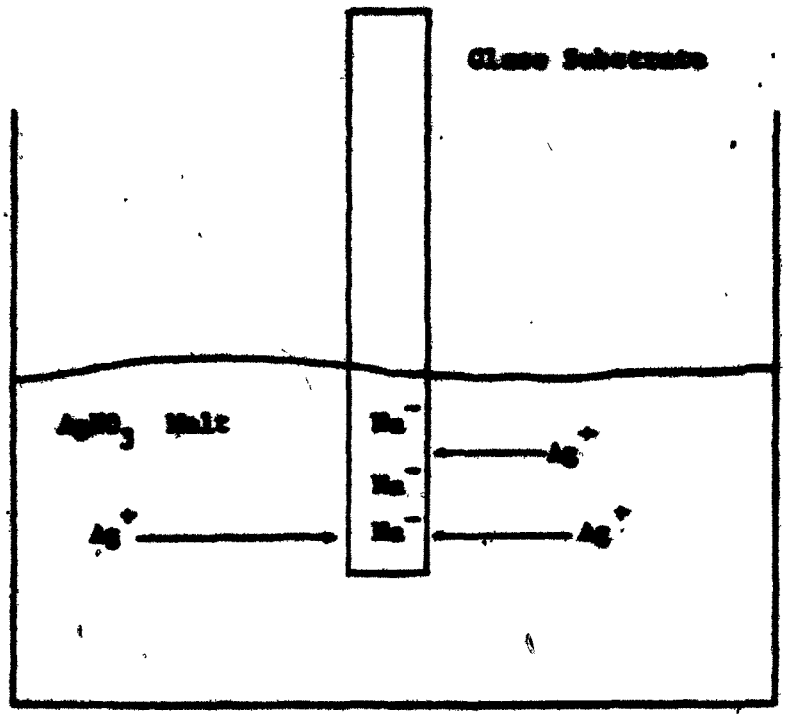

Fig. 2.1 The Ion Exchange Mechanism based on the Double Diffusion Process.

the exchanger and ions from the melt are completely exchangeable, reside in similar lattice sites and diffuse by the same mechanism. The stoichiometry of ion exchange requires that the fluxes of the two exchanging counter ions be equal in magnitude even though they may possess different mobilities. While the faster ions tend to diffuse at a faster rate, any excess flux of an ion precipitates a net transfer of electric charge and thus produces an electric field which slows the faster ion and accelerates the slower ion to equalize the fluxes (Fig. 2.1). Hence electroneutrality is preserved. Sections 2.2 & 2.3 are based on previous work by Stewart et al (9), (13).

2.2 Double Diffusion Process

Consider the specific double diffusion process that occurs when a soda-lime substrate is immersed in a molten $AgNO_3$ salt bath. It is convenient to define an interdiffusion coefficient; (9)

$$D = \frac{D_A D_B}{N_A D_A + N_B D_B}, \quad N_A = \frac{C_A}{C_A + C_B}, \quad N_B = \frac{C_B}{C_A + C_B} \qquad (2.1)$$

D_A, D_B, diffusivity coefficient of Na and Ag respectively

C_A, C_B, concentration of Na and Ag respectively.

It is evident that the interdiffusion coefficient is dependent on the concentration of the melt. Expressing the coefficient as a function of the silver concentration, we obtain:

$$D(C_B) = \frac{D_B}{(1 - a(C_B/C_o))} \qquad (2.2)$$

$$a = (D_A - D_B) / D_A$$

C_o = surface concentration of silver

In order to determine the silver concentration profile, we need to solve the diffusion equation. There exists a relationship between the impurity concentration profile and the actual refractive index profile obtained after ion exchange. According to Burggraff (5) since Na ions are physically larger than Ag ions (and diffuse 12 times faster), the lattice structure of the exchanged region is altered. The surface of the glass is placed in a state of compression. Due to the compressed state of the exchanged layer and the fact that the polarizability of the electrons has been altered, the refractive index of the glass will increase. This is highly desirable for obtaining light guides since an elevated refractive index is necessary for the confinement of

light. Thus, by solving the pertinent diffusion equation, we obtain information on the impurity concentration, and hence the refractive index change within the substrate.

In view of the fact that the interdiffusion coefficient is concentration dependent, we must express the diffusion equation as follows:

$$\frac{\partial C_B}{\partial t} = \frac{\partial}{\partial x}\left[D(C_B)\frac{\partial C_B}{\partial x}\right] \tag{2.3}$$

x: depth from the melt-glass interface into the glass

The boundary conditions for our diffusion problem are those of a constant source diffusion situation;

$$\left.\begin{aligned} C_B(o,t) &= C_o \,. \qquad C_B(\infty,t) = 0 \\ C_B(x,o) &= 0 \end{aligned}\right\} \tag{2.4}$$

If the diffusion coefficient was constant, we could expect a simple solution expressed in terms of the complementary error function (31);

$$C_B(x,t) = C_o \operatorname{erfc} \frac{x}{\sqrt{D_B t}} \tag{2.5}$$

Since this is not the case, we resort to a solution via the infinite power series method (17) and we can express the silver concentration with respect to the surface concentration of silver (C_o) as:

$$\frac{C_B}{C_o}(x,t) = 1 - \left[\frac{2(1-\alpha)^{3/2}}{\alpha} \cdot \sqrt{\frac{2}{\mu}}\right] \frac{x}{2\sqrt{D_B t}} - \left[\frac{4(1-\alpha)^2}{\alpha^2}\right] \left(\frac{x}{2\sqrt{D_B t}}\right)^2 +$$

$$\frac{2(\mu-4)\,(1-\alpha)}{3\alpha\mu}^{5/2} \sqrt{\frac{2}{\mu}} \left(\frac{x}{2\sqrt{D_B t}}\right)^3 + \ldots\ldots \tag{2.6}$$

where μ is determined from α via the following relation:

$$\ln(1-\alpha) = -2 \int_0^1 (\theta_1^2 - \mu \ln \theta_1^2)^{-1/2}\, d\theta_1 \tag{2.7}$$

which is well tabulated (17).

The infinite series solution (2.6) is then related to the following polynomial profile, to present a more manageable solution:

$$n(x) = n_o - \Delta n_s \left[(x/d) + b(x/d)^2 \right] \tag{2.8}$$

$$\Delta n_s = n_o - n_{bulk}$$

n_o: surface index

The variable d is called the diffusion length and is related to D and time; (4)

$$d = 2\sqrt{Dt} \tag{2.9}$$

Rewrite (2.8) as:

$$\frac{\Delta n(x)}{\Delta n_s} = 1 - \left(\frac{x}{\sqrt{Dt}}\right) - b\left(\frac{x}{\sqrt{Dt}}\right)^2 \tag{2.10}$$

$$\Delta n(x) = n(x) - n_b$$

with the polynomial profile written in the form of (2.10), the coefficients of the x and x^2 terms in (2.6) are the same as those of (2.10) when:

$$D_B = \frac{2(1-a)^3}{\mu a^2} D , \qquad a = \frac{2b}{(2b + 1)}$$

Thus (2.10) is a valid solution of the diffusion equation for our particular boundary conditions. Stewart et al (9) graph for comparative purposes, both the theoretical silver conc. & the 2nd order polynomial index profile (Fig. 2.2).

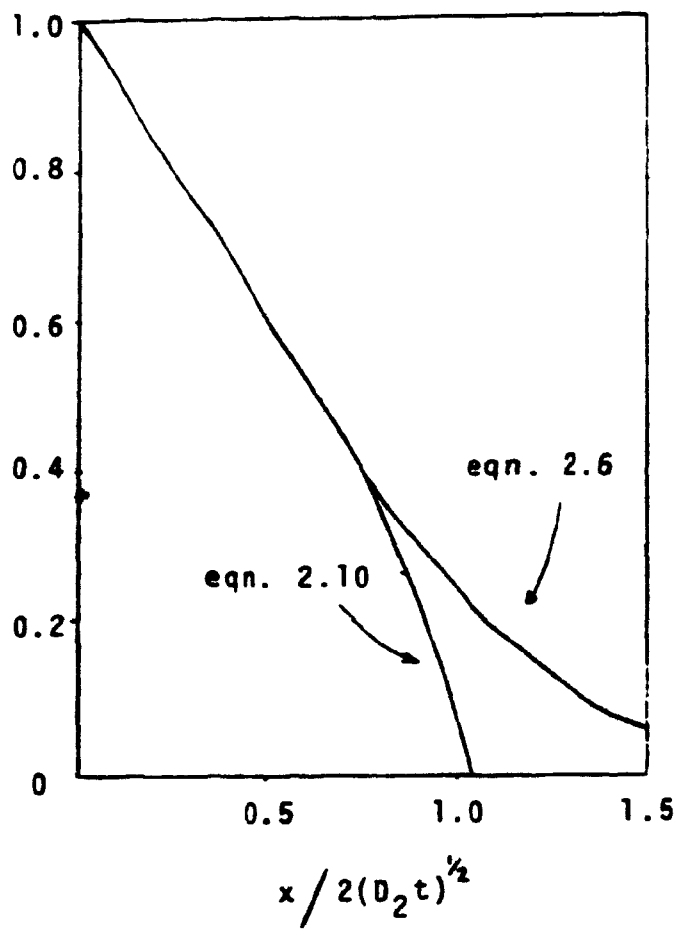

Figure 2.2 Comparison of Equations 2.6 & 2.10

We see a deviation exists at low values of (C_2/C_o) due to the fact that the series solution is truncated after three terms to provide a second order polynomial profile.

2.3 Diluted Melts

There are many disadvantages in the use of a pure $AgNO_3$ melt for ion exchanged waveguide fabrication, provoking a study of diluted melts; (13)

- large change in surface index, hence poor repeatability,
- to make single mode channel guides, small widths of a few microns are necessary, complicating the fabrication process,
- high silver concentrations are present in the glass, yielding colloidal crystals which stain the glass and increase guide loss,
- pure silver nitrate is expensive, even with commercial grade quality.

By diluting the melt with $NaNO_3$, the above problems are avoided and the Ag concentration can be controlled at the surface and throughout the film.

The exchange process at the glass-melt interface is represented by (13)

$$\bar{Na}^{+} \text{ (glass)} + Ag^{+} \text{ (melt)} =$$

$$\bar{Ag}^{+} \text{ (glass)} + Na^{+} \text{ (melt)} \qquad (2.11)$$

An equilibrium constant associated with the glass melt interface is defined as:

$$K_{AB} = \frac{\bar{a}_B a_A}{\bar{a}_A a_B} \qquad (2.12)$$

$\bar{a}_A$, $\bar{a}_B$ are the thermodynamic activities of sodium and silver in the glass, respectively.

a_A, a_B are the thermodynamic activities of sodium and silver in the melt, respectively.

According to regular solution theory (13), the diluted silver nitrate melt can be represented by the following:

$$\ln \frac{a_B}{a_A} = \ln \frac{n_B}{n_A} - \frac{\Omega}{RT} (1 - 2n_A) \qquad (2.13)$$

E: net interaction energy of the ions

= 3.5×10^3 J/mole for Ag-Na systems

m_A: mole fraction $NaNO_3$

m_B: mole fraction $AgNO_3$

R: gas constant

T: absolute temp.

In the glass phase we have: (32)

$$\frac{\bar{a}_B}{\bar{a}_A} = (\bar{N}_B/\bar{N}_A)^{\gamma} \qquad \gamma\text{: constant} > 1 \qquad (2.14)$$

$\bar{N}_A$, $\bar{N}_B$ mole fractions of sodium and silver ions at the glass surface.

Combining equations 2.12, 2.13 and 2.14 we derive the following relation:

$$\ln (m_B/m_A) - \frac{E}{RT}(1 - 2m_A) = \gamma \ln \left(\frac{\bar{N}_B}{\bar{N}_A}\right) - \ln K_{AB} \qquad (2.15)$$

If we assume that all sodium ions are replaced with silver ions at the glass-melt interface in the undiluted $AgNO_3$ case, and that Δn is proportional to the Ag^+ concentration, we can write (2.15) as:

$$\ln(m_B/m_A) - \frac{E}{RT}(1 - 2m_A) = \gamma \ln \left[\Delta n_{sp}/(\Delta n_{sp} - \Delta n_{sd})\right] - \ln K_{AB} \qquad (2.16)$$

Δn_{sp}: surface index charge with a pure $AgNO_3$ melt.

Δn_{sd}: surface index charge with a diluted $AgNO_3$ melt.

We now redefine the interdiffusion coefficient (2.2) for the case of diluted melts. Recall equation (2.1), and consider that it can be rewritten in the following form:

$$D_{AB} = \frac{D_B}{1-\alpha(C_s/C_o)\cdot(C_B/C_s)} = \frac{D_B}{1-\alpha(\Delta n_s/\Delta n_{sp})c} \qquad (2.17)$$

where $\alpha = (D_A-D_B)/D_A$, $c = C_B/C_s$

C_s : surface concentration of silver

Co : sodium concentration in the unexchanged substrate.

Equation (2.18) governs the dependence of D_{AB} on the silver concentration.

$$\alpha' = \alpha(\Delta n_s/\Delta n_{sp}) \qquad (2.18)$$

By further dilution of the melt, according to (2.18), the profile depth is reduced, along with a change in the form of the profile. For a very dilute melt, α' approaches zero

and D_{AB} approaches D_B and the solution of the diffusion equation becomes:

$$C = \text{erfc}\ (x/2\sqrt{D_B t}) \qquad (2.19)$$

as expected from the previous result.

Potassium ion-exchange has been reported by some researchers (6-8), and the physics of the exchange corresponds to the theory presented in this chapter, provided the substrate is of aluminosilicate glass composition. It is not known if the guides formed in soda-lime glass by KNO_3 conform to the theory presented herein, and this topic will not be pursued theoretically speaking, in spite of the fact that all KNO_3 ion-exchanged guides as well as $AgNO_3$ (pure and diluted) exchanged guides were made with soda-lime glass.

CHAPTER III

THEORY OF INHOMOGENEOUS SLAB WAVEGUIDES

3.1 Introduction

Inhomogeneous slab guides have been analyzed by various methods over the past decade. Several theoretical models are examined here and the conditions for guidance are considered before fabrication procedures for slab guides are discussed.

H. Kirchoff (18) performed an exact analysis to obtain solutions of Maxwell's equations for the inhomogeneous slab guide. D. Marcuse (19) used a piecewise linear approximation based on the WKB* method, to characterize the TE modes of the graded index slab waveguide. A numerical method, established on invariant imbedding and the transverse impedance concept by Kuester & Chang (34) was employed to analyze the guiding characteristics of the asymmetric slab guide. More recently, the WKB approximation has been exploited (23), (35) for guides having monotonically, slowly varying refractive index profiles.

Yip and Colombini (20) used both the WKB and staircase approximation to analyze a symmetric slab

(*Wentzel-Kramers - Brillioun)

waveguide. Agreement in the dispersion characteristics generated by both methods is quite good, except for minor deviation near the cut-off frequency of any particular mode.

3.2 Propagation in inhomogeneous media

In view of the fact that ion-exchanged waveguides conform to the properties of diffused guides, it is evident that the refractive index will be an inhomogeneous one. In an inhomogeneous waveguide, the transvere wavenumber k, exhibits a dependence on position, taken to be the x-direction (36).

A ray representation of wave propagation in this media is depicted in Fig. 3.1.

In the neighbourhood of x_t (the turning point), the ray model falls apart due to the fact that the WKB approximation predicts a singularity in the field expressions at the turning point. The total phase change experienced by the wave as it travels from the air-guide interface to the turning point and back again is given by (21):

$$\phi = 2k_o \int_0^{x_t} n_1(x) \cos\theta \, dx \qquad (3.1)$$

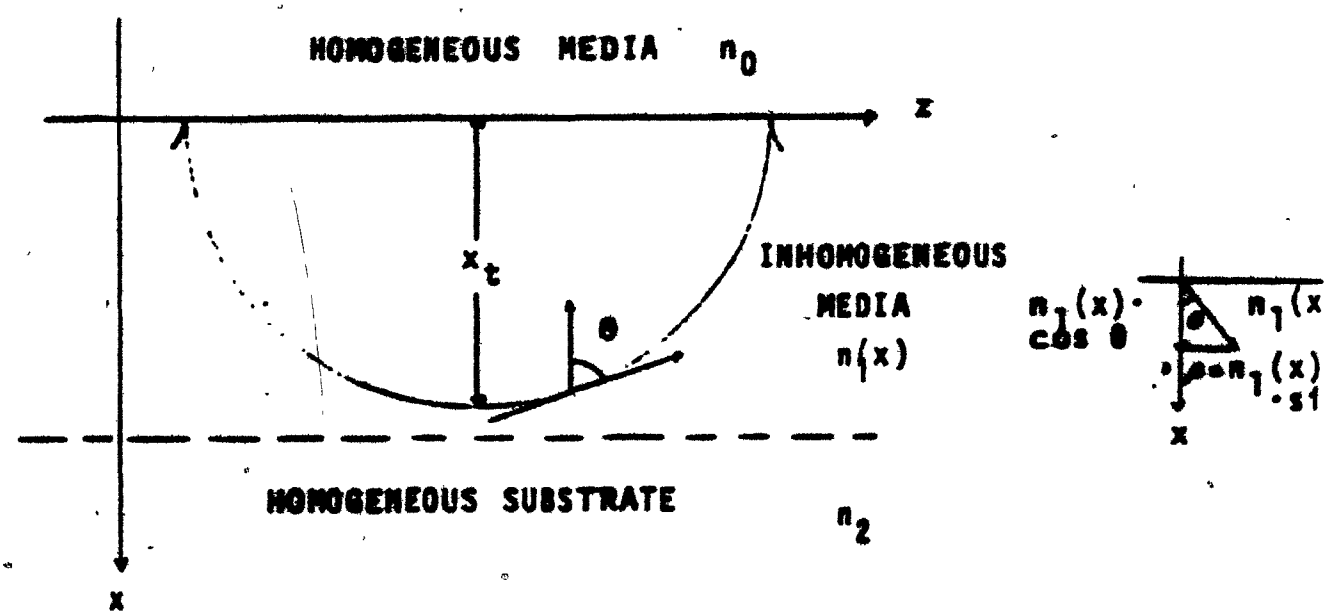

Fig. 3.1 Inhomogeneous Slab Waveguide Ray Model.

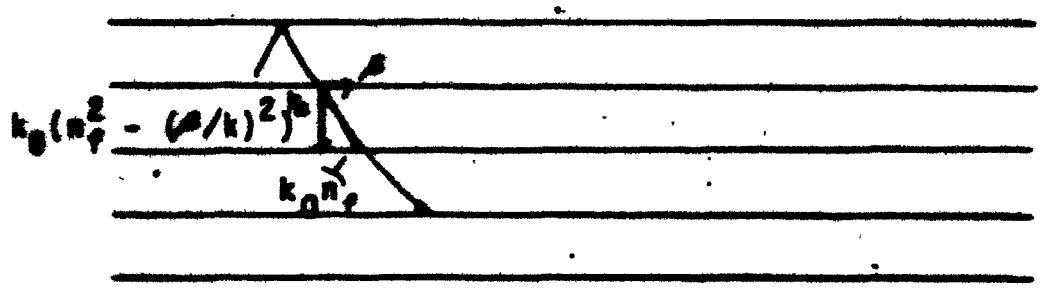

Fig. 3.2 Orientation of Wavevectors in Layered Homogeneous Media.

By applying the WKB approximation, solutions to the wave equation for the slab guide,

$$\frac{\partial^2 E_Y}{\partial x^2} - (\beta^2 - n^2 k_o^2) E_Y = 0 \tag{3.2}$$

$k_o = \omega\sqrt{\mu_o \varepsilon_o}$, β: axial propagation constant

may be obtained. The WKB approximation is stated in the following equation:

$$2k_o \int_{x_{t_1}}^{x_{t_2}} (n_1^2(x) - (\beta/k_o)^2)^{\frac{1}{2}} \, dx = 2\phi_{12} + 2\phi_{10} + 2m\pi \tag{3.3}$$

$$m = 0,1,2...$$

note that $k_o^2 n^2(x) = k_o^2 n_1^2(x) \cos^2\theta = k_o^2 \cdot n_1^2(x) - \beta^2$ (3.4)

The turning points x_{t_1} and x_{t_2} are determined by (3.4) and by the fact that at a turning point $\theta = 90^o$.

$$n_1(x_{t_1}) = n_1(x_{t_2}) = \beta/k_o \tag{3.5}$$

The turning point x_{t_1}, occurs at the air-guide boundary, and the phase change here is governed by the Fresnel formula:

$$2\phi_{10} = 2\tan^{-1}\gamma \left[\frac{(\beta/k_o)^2 - 1}{n_1^2(0) - (\beta/k_o)^2}\right]^{\frac{1}{2}} \tag{3.6}$$

For TE modes $\gamma = 1$, and for TM modes $\gamma = n_1^2(0)$. In the case of a buried mode, between two given turning points, the phase change $2\phi_{10}$ is approximately $\pi/2$ for both polarizations. The

phase change at the guide-substrate interface is always $2\phi_{12} = \pi/2$.

Note that equation (3.3) is valid provided the refractive index profile is slowly varying and this condition is applicable to ion-exchanged waveguides. By analyzing wave propagation in layered homogeneous media (21), we can present the guided wave solutions for inhomogeneous slab waveguides. We start by manipulating Maxwell's equations in a charge-free inhomogeneous medium.

$$\nabla^2 \underline{E} + k\underline{E}^2 + \nabla((1/\varepsilon)\underline{E}\cdot\nabla\varepsilon) \qquad (3.7)$$

$k = \omega\sqrt{\mu_0 \varepsilon}$ $\qquad$ ε, a function of position.

If harmonic time dependence, $e^{j\omega t}$ is assumed, and if we consider the following equations, (3.7) can be reduced to the standard form;

$$\underline{E} = -\nabla\phi - \partial\underline{A}/\partial t \qquad (3.8)$$

$$(\underline{B} = \nabla \times \underline{A}) \qquad (3.9)$$

Maxwell's equations are satisfied provided

$$\phi = \nabla\cdot((\partial\underline{A}/\partial t)/k^2) \qquad (3.10)$$

and

$$\nabla^2\underline{A} + k^2\underline{A} - (2/k)\ (\nabla\cdot\underline{A})(\nabla k) = 0 \qquad (3.11)$$

Assume that the wavenumber k is a function of depth or the x coordinate only, and that the axes are oriented such that $\underline{A}$ is independent of y. If $\underline{A}$ is y directed (TE polarized), equation 3.11 reduces to

$$\nabla^2\underline{A}_y + k^2\underline{A}_y = 0 \qquad (3.12)$$

If $\underline{A}$ is TM polarized, equation (3.11) becomes

$$\nabla^2\psi + (k^2 + k''/k - 2k'^2/k^2)\ \psi = 0 \qquad (3.13)$$

where $\psi = A_x/k$

Let $k(x) = (k^2 + k''/k - 2k'^2/k^2)^{\frac{1}{2}}$ be the effective wavenumber. ($' = d/dx$, $'' = \partial^2/\partial x^2$). Employing this notation, the problem of propagation in inhomogeneous media is reduced to the solution of the following wave equation;

$$\nabla^2 \psi + k^2(x)\psi = 0 \tag{3.14}$$

If the effective wavenumber $k(x)$ is assumed to be slowly varying, k' & k'' can be neglected and a solution to (3.14) is expressed as:

$$\psi(x,z) = X(x) \; e^{-j\beta z} \tag{3.15}$$

with $X(x)$ to be determined from:

$$\frac{\partial^2 X}{\partial x^2} + (k^2(x) - \beta^2) X = 0 \tag{3.16}$$

According to Brekhovskikh (21), if one considers plane waves propagating normal to the layered media, order of magnitude estimates lead to a solution;

$$\psi(x) = 1/\sqrt{k(x)} \left[A_1 e^{-j \int_{x_0}^{x} k dx} + A_2 e^{j \int_{x_0}^{x} k dx}\right] \tag{3.17}$$

consider $\int_{x_0}^{x} k dx$ as the phase change of a wave travelling from an arbitrary point x_0 to some other point x. We can see from the bracketed term in (3.17) that we have wave propagation in the positive and negative x directions. If ψ is taken to be E_y and consider only TE modes, (3.17) becomes

$$E_y = 1/(k\cos\theta)^{\frac{1}{2}} \left[C_1 e^{-j \int_{x_0}^{x} k\cos\theta dx} + C_2 e^{j \int_{x_0}^{x} k\cos\theta dx}\right] e^{-j\beta z}$$

$k\cos\theta = (k^2 - \beta^2)^{\frac{1}{2}}$ for oblique incidence. (3.18)

Because K and cosθ are slowly varying functions of position, they are taken as constants. The magnetic fields for this case are:

$$H_x = -\beta/\omega\mu \; E_y \,, \quad H_z = j/\omega\mu \frac{dE_y}{dx} \qquad (3.19)$$

It is now clear from equation (3.18) that the WKB approximation becomes invalid at a turning point. By substituting $\theta = 90^{\circ}$ in equation (3.18), the solution for E_y becomes infinite. Hence the WKB approximation falls apart in the neighborhood of a turning point. Via a study of total reflection of waves in layered inhomogeneous media, it has been shown by Brekhovskikh (21) that the phase change in the neighborhood of a turning point is $\pi/2$.

3.3 A WKB method for index profiles

To comprehend the guidance characteristics of ion-exchanged waveguides, it is important to be able to define their refractive index profiles. Ion-exchanged waveguides are essentially diffused guides conforming to Fickian diffusion laws, so we expect smooth, inhomogeneous refractive index profiles, varying with respect to the guide depth.

White and Heidrich (22) have used the WKB approximation to derive simple equations that predict the shape of the refractive index profile from measured effective mode

indices of a planar optical guide. Their technique involves the solution of the inverted Sturm-Liouville eigenvalue problem. Since the amount of input data is finite, (i.e. a finite set of mode indices) the refractive index profile, n(z), z being the depth coordinate, is estimated in terms of straight line segments. The WKB approximation transposes the solution of the Sturm-Liouville system;

$$(r(z)F') + (q(z) + \lambda p(z))\, F = 0 \qquad (3.20)$$

boundary conditions: $k_1 F + k_2 F' = 0 \quad (z = a)$

$I_1 F + I_2 F' = 0 \quad (z = b)$

solution: $E_y = F(z)\, e^{j(k_x x - \omega t)}$

to the solution of the equation

$$\int_0^{z_m} (n^2(z) - n_m^2)^{\frac{1}{2}}\, dz = \frac{4m - 1}{8} \qquad (3.21)$$

$$m = 1, 2, 3 \ldots M$$

$$n(z_m) = n_m, \quad z_o = 0, \; n_o = n(0)$$

As previously mentioned, since (3.21) employs the WKB approximation, n(z) must decrease monotonically and be slowly varying. Equation (3.21) also assumes that the phase shift experienced by a ray at the surface has an average value of $\pi/2$ and a value of $\pi/4$ at z_m, the turning point.

In order to derive (3.21), consider the sum of all phase shifts incurred by an incident wave, in travelling

from the air-guide interface to the turning point and back again as in Fig. 3.1. As stated above, the phase shift at the turning point is $\phi_{12} = -\pi/4$ and the phase shift at the air-guide interface is governed by the Fresnel formula, and was calculated as $\phi_{10} = -\pi/2$.

One of the conditions for guidance requires that the total transverse phase shift of a light ray be a multiple of 2π. If the phase shift experienced by the ray when travelling from the air-guide interface to the guide-substrate interface is calculated and added to the ϕ_{12} and ϕ_{10} phase shifts, the sum must total to $2m\pi$, m integer.

The total transverse phase shift can be calculated by dividing the inhomogeneous region into several thin homogeneous layers and adding the phase shift incurred at each layer.

The transverse component of the wavevector is expressed as $k_o\sqrt{n_f^2-(\beta/k_o)^2}$ or equivalently $k_o\sqrt{n_f^2-N_{eff}^2}$. Summing all the phase shifts incurred at every layer we write:

$$k_o \int_o^{z_m} (n^2(z) - N_{eff}^2)^{\frac{1}{2}}\, dz \qquad (3.22)$$

where z_m is the turning point defined by $n(z_m) = N_{eff}$. Hence the phase relationship becomes:

$$2k_o \int_o^{z_m} (n^2(z) - N_{eff}^2)^{\frac{1}{2}} dz = 2m\pi - 2\phi_{10} - 2\phi_{12} \qquad (3.23)$$

But since $2\phi_{10} = -\pi$ and $2\phi_{12} = -\pi/2$

$$k_o \int_o^{z_m} (n^2(z) - N_{eff}^2)^{\frac{1}{2}} d\bar{z} = m\pi + \pi/2 + \pi/4 \qquad (3.24)$$

Normalizing z to λo where $\bar{z} = z/\lambda o$, and dividing both sides by 2π;

$$\int_o^{\bar{z}_m} (n^2(\bar{z}) - N_{eff}^2)^{\frac{1}{2}} d\bar{z} = m\pi + \tfrac{1}{4} + 1/8 \qquad (3.25)$$

where $m = 0,1,2...$

Since m starts from 1 in equation (3.21), we subtract 2π from the RHS of (3.25) and hence (3.21) has been derived.

Given the effective mode indices n_m, we calculate the values of z_m (hence approximating $n(\bar{z})$) by rewriting (3.21) as a sum of integrals

$$\sum_{k=1}^{M} \int_{\bar{z}_{k-1}}^{\bar{z}_k} (n^2(\bar{z}) - n_m^2)^{\frac{1}{2}} d\bar{z} = \frac{4m - 1}{8} \qquad (3.26)$$

The origin of the profile-determining algorithm lies in the WKB approximation, requiring smooth, slowly varying index profiles. This can be interpreted by assuming $n(\bar{z})$ as a piecewise linear function:

$$n(\bar{z}) = n_k + \frac{(n_{k-1} - n_k)}{(\bar{z}_k - \bar{z}_{k-1})} (\bar{z}_k - \bar{z}) \tag{3.27}$$

where $\bar{z}_{k-1} \leq \bar{z} \leq \bar{z}_k$ and $n(z) + n_m$ is replaced by

$$(n_{k-1} + n_k/2) + n_m \tag{3.28}$$

After substitution and simplification (see Appendix C) an expression for $\bar{z}_m$ can be derived, representing the normalized depth for a given refractive index value.

$$\bar{z}_m = 3/2 \left(\frac{3n_m - n_{m-1}}{2}\right)^{-\frac{1}{2}} (n_{m-1} - n_m)^{-\frac{1}{2}} \left[\frac{4m - 1}{8} - \frac{2}{3} \sum_{k=1}^{M-1} \left(\frac{n_k + n_{k-1} + 2n_m}{2}\right)^{\frac{1}{2}} \times \frac{\bar{z}_k - \bar{z}_{k-1}}{n_{k-1} - n_k} \left[(n_{k-1} - n_m)^{3/2} - (n_k - n_m)^{3/2}\right]\right] + \bar{z}_{m-1} \tag{3.29}$$

where $m = 2,3,4,\ldots M$

Equation (3.29) will give the next value of $\bar{z}_m$, given the previous point and the effective index value. To start the algorithm, use the following expression for $\bar{z}_1$ (m=1);

$$\bar{z}_1 = \frac{9}{16} \left(\frac{n_o + 3n_1}{2}\right)^{-\frac{1}{2}} (n_o - n_1)^{-\frac{1}{2}}, \; m = 1 \tag{3.30}$$

By using (3.29) and (3.30) and a set of effective index values, one can write an algorithm to approximate the refractive index profile. Since the algorithm is based on the WKB approximation,

we expect less accuracy in the index profile near the surface where information on the lower order modes is required. This requires that the surface index n_o must be approximated as closely as possible. This can be estimated by plotting the RHS of the WKB integral

$$k_o \int_o^{z_t} (n^2(\bar{z})-N_{eff}^2)^{\frac{1}{2}}\, d\bar{z} = m\pi + \pi/4 + \phi_{10} \qquad (3.31)$$

versus the set of experimentally measured effective mode indices as per Stewart et Al (9). The index value will be estimated as the point where this curve intersects the x axis. (See Fig. 3.3.)

With this starting value of n_o, the algorithm can proceed and a complete set of data points $(\bar{z}_m, n(\bar{z}_m))$ can be obtained. Armed with these data points, a minimisation procedure can be followed so that the ideal value of n_o is known. The determination of n_o is dependent on minimizing the sum of the areas of the triangles described by the following set of points: $(n_k, \bar{z}_k)$, $(n_{k+1}, \bar{z}_{k+1})$, $(n_{k+2}, \bar{z}_{k+2})$ for all $k = 0, 1, \ldots M-2$. Thus for each set of data points $(n_m, \bar{z}_m)$ generated by a given starting value of n_o, this calculation of triangular areas is performed. Then the surface index n_o is incremented slightly and the process is repeated. The set of data points yielding the smallest sum of triangular areas is deemed the best approximation to the refractive index profile.

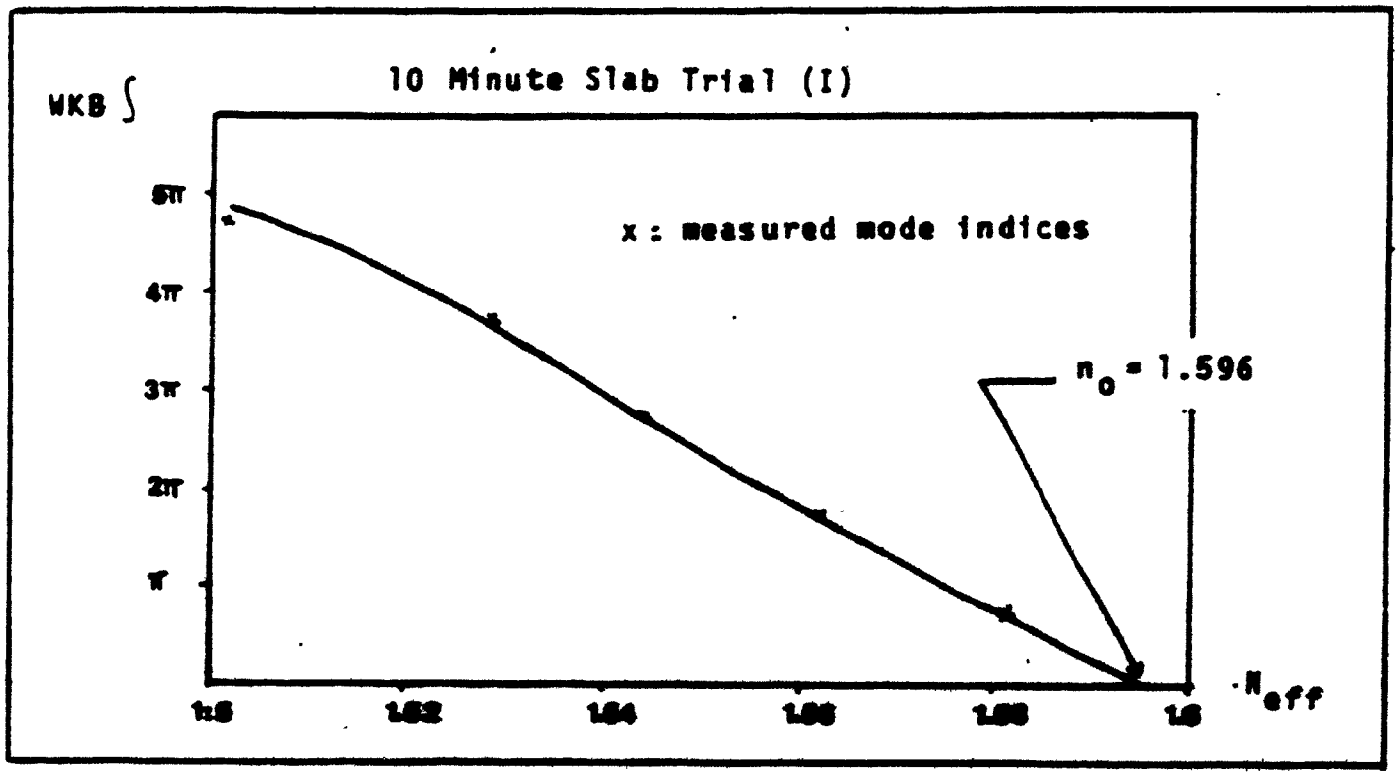

Fig. 3.3 Surface Index Evaluation by the WKB Method for an $AgNO_3$ exchange (10 min., 245 °C)

The routine is very sensitive to the initial estimate for n_o. If the estimate is not close to the actual value, the routine will oscillate, yielding poor results. It can be noted that the uncertainty in n_o is most critical for the first mode and is decreasingly important thereafter. This correlates with the fact that the WKB method is weakest for the determination of turning points corresponding to extreme order modes.

Another point worth mentioning is the fact that this profiling algorithm requires a multimode waveguide, yielding numerous N_{eff} values. If the waveguide being considered only supports 2 or 3 modes, the accuracy of the resulting profile becomes questionable.

3.4 WKB method for dispersion curves

To gain a physical understanding of the dispersion characteristics of ion-exchanged waveguides, we must solve the dispersion equation.

By considering zig-zag wave propagation or the ray model, we can gain an insight in the derivation of the dispersion relation. The guided modes are discreet, and only those which undergo a phase shift of 2 mπ (m integer) are allowed.

In this section, the agreement between exact and approximate theoretical dispersion curves is to be compared. Theoretical curves for inhomogeneous media for both $AgNO_3$ and KNO_3 parameters are generated via computer algorithms. Consider the inhomogeneous waveguide analysis:

Inhomogeneous Index

The derivation of the WKB expression for the dispersion equation for inhomogeneous proceeds as follows: (see Hocker & Burns (25)). The total phase change experienced by the wave as it travels from the air-guide interface to the turning point and back again is:

$$\phi = 2k_o \int_0^{x_t} n(x) \cos\theta \, dx \tag{3.32}$$

Refer to Fig. 3.1 for the parameter definition. As stated in Section 3.2 of this chapter, the phase change in the presence of a turning point is $\pi/2$ and the phase change at the air-guide interface is $2\phi_{10}$ or in normalized quantities: $2 \tan^{-1} \left[(b + a)/(1 - b)\right]$.

Adding all the phase shifts incurred as a wave travels one complete period, we write the inhomogeneous dispersion equation in normalized form. Equation (3.32) can be rewritten as:

$$2k_o \int_0^{x_t} (k_o n^2(x) - \beta^2)^{\frac{1}{2}} \, dx \tag{3.33}$$

and normalized to:

$$2V \int_0^{x_t} (n(x) - b)^{\frac{1}{2}} \, dx \tag{3.34}$$

Since we deal with inhomogeneous media, we must renormalize V,b and a in terms of the parameter, n_s:

$$V = k_o d \sqrt{(n_s^2 - n_b^2)} \tag{3.35}$$

$$b = (N^2 - n_b^2) / (n_s^2 - n_b^2) \tag{3.36}$$

$$a = (n_b^2 - n_c^2) / (n_s^2 - n_b^2) \tag{3.37}$$

with the following nomenclature:

n_b = bulk index, n_c = cover index,

n_s = surface index, N = effective index.

The final form of the dispersion equation, expressed in normalized quantities is as follows:

$$2V \int_0^{x_t} (n(x) - b)^{\frac{1}{2}} \, dx = (2m + \tfrac{1}{2})\pi + 2\tan^{-1} \left[(b+a)/(1-b)^{\frac{1}{2}}\right] \tag{3.38}$$

The above relation can be solved numerically and software was designed employing the IMSL routine DCADRE, based on an iterative Rhomberg integration routine (refer to Appendix B). The required input to the program includes a function describing the diffusion profile n(x) and the appropriate asymmetry measure a. The restriction on n(x) is that it must vary between 0 and 1 and it must be a slowly varying, monotonically decreasing function. Also, n(x) must be represented in an analytical expression. If this is not possible, and n(x) can only be expressed on a point by point basis (as in the case of the WKB generated refractive index profile by Heidrich & White), the IMSL integration routine cannot be used. Instead, an integration algorithm based on Simpson's rule can be employed to solve equation (3.38).

Basically, the value of b is incremented and the corresponding turning point x_t is solved such that:

$$n(x_t) = b \tag{3.39}$$

With the knowledge of x_t, the required integral is calculated by either method mentioned above and the program solves for V.

The comparison between the dispersion curves for inhomogeneous slab guides generated by WKB theory and the experimentally generated curves is once again possible by using

equations (3.35) - (3.37). The N_{eff} values for a particular slab guide are normalized so they can be located in the b-V plane, the predominant parameter being n_s. Rather than relying on an approximate value for n_s, as generated by the profiling algorithm, a more refined value is necessary. Starting with the value of n_s from the refractive index profile (by Heidrich & White's method) and employing (3.38) along with any two measured effective mode indices, a more exact value of Δn_s ($\Delta n_s = n_s - n_b$) and hence n_s can be determined.

The dispersion curves calculated for an inhomogeneous profile (Gaussian) for the two asymmetry measures: $AgNO_3$ and KNO_3 are presented in Fig. 3.4 and 3.5 respectively.

3.5 Dispersion curves by the step approximation method

The step or staircase approximation can be considered as a brute force method giving exact results, opposed to the approximate results yielded by the WKB method. The crux of the method involves approximating an inhomogeneous medium by several homogeneous layers, the greater the number of layers, the better the approximation. Since we are interested in characterizing asymmetric waveguides, conforming to the situation of ion-exchanged guides, a Gaussian profile will

Gaussian Diffusion Profile ($AgNO_3$)

Figure 3.4

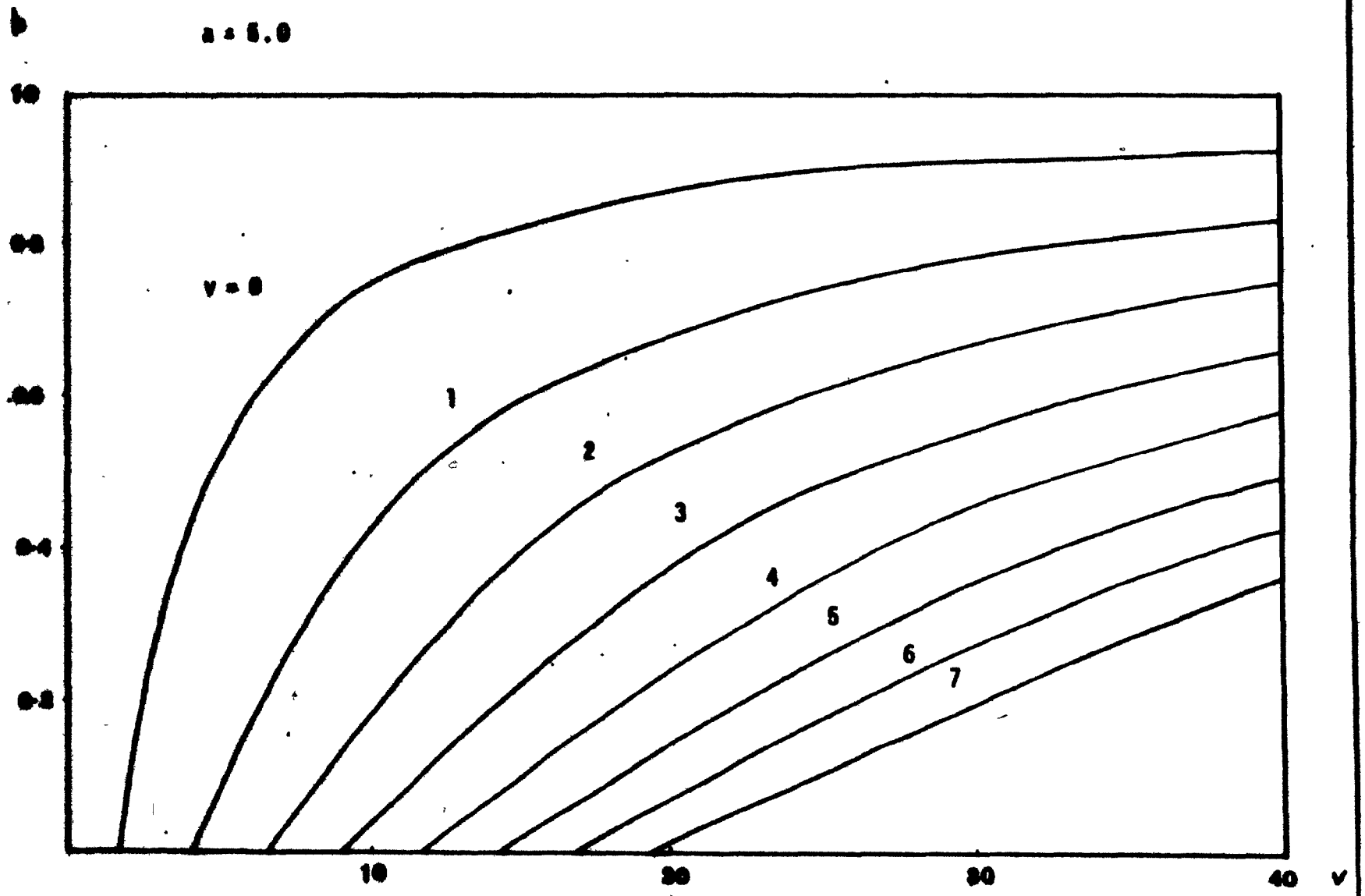

Gaussian Diffusion Profile (KNO_3)

Figure 3.5

a = 32.5

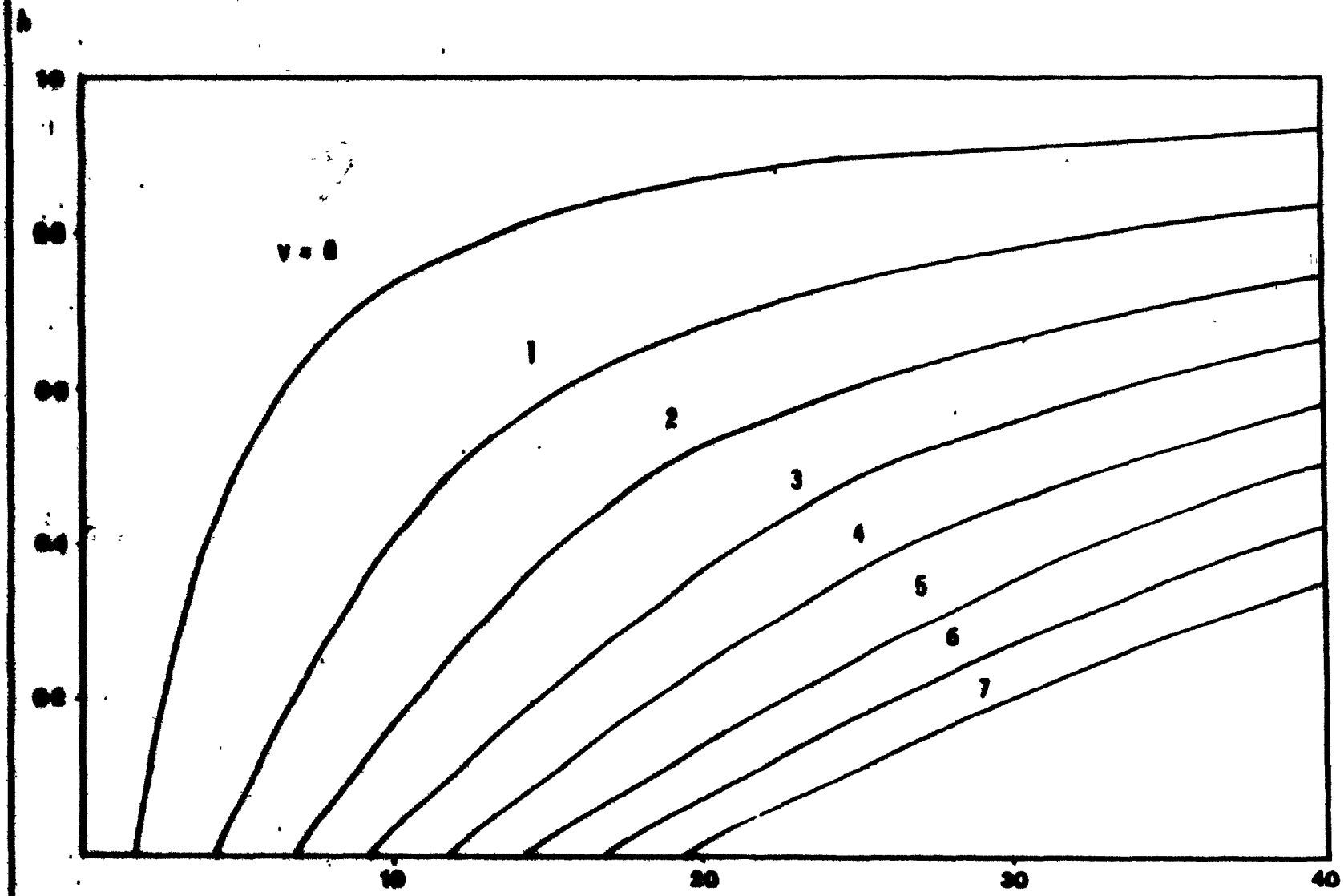

provide a suitable example for the quantization procedure. Consider the refractive index profile in Fig. 3.6, subdivided for analysis.

If we assume an infinite slab guide such that $d/dy = 0$ then we can consider TE modes

<u>TE modes</u> $(E_x = E_z = H_y = 0)$

Assume the usual travelling wave term: $e^{j(\omega t-\beta t)}$. From Maxwell's equations $\nabla \times E = -\mu_o \partial H/\partial t$

$$\nabla \times H = \epsilon_o n^2 dE/\partial t \qquad (3.40)$$

and the fact that $\partial/\partial y = 0$, we derive the one dimensional reduced wave equation for the Ey component.

$$\partial^2 Ey/\partial x^2 + (n^2k^2 - \beta^2)Ey = 0 \qquad (3.41)$$

$$k = 2\pi/\lambda_o$$

Associated with this, are the transvere wavevectors K_i =

$$k_o(n_i^2 - \bar{\beta}^2)^{\frac{1}{2}}, \quad \gamma_i = k_o(\bar{\beta}^2 - n_i^2)^{\frac{1}{2}} \qquad (3.42)$$

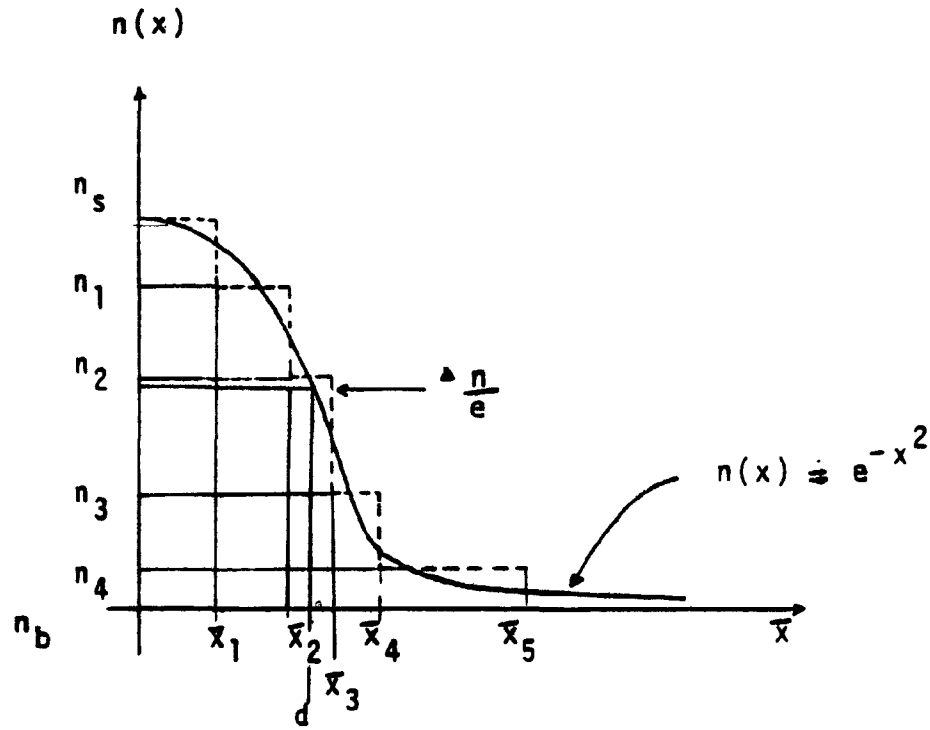

Fig 3.6 Gaussian Profile Subdivided for Analysis.

x: transverse depth, d: guide depth at n_e, $\Delta n = n_s - n_b$
$\bar{x} = x/d$, n_s: surface index, n_b: bulk index,

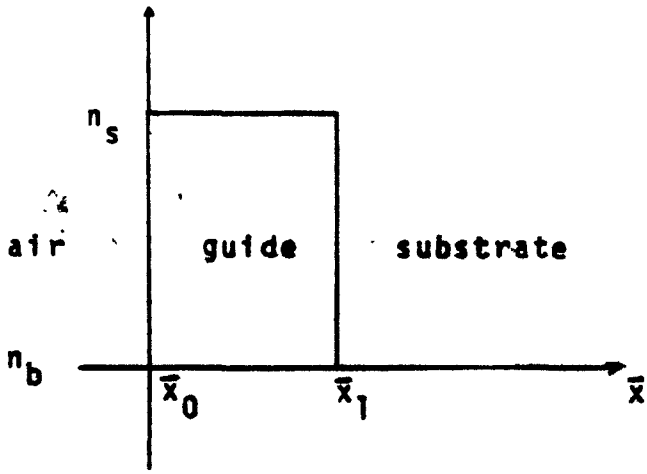

Fig. 3.7 Single Step Approximation.

The subscript i designates which layer the quantity in question represents. Choose K_i if the fields are oscillatory in the region or select γ_i if the normalized propagation constant $\bar{\beta}$ predicts decaying fields for that region

For simplicity, consider the case of a single layer, the staircase approximation proceeds as follows.

(I) define the normalized transverse depth boundaries (quantization procedure) see Fig 3.7, the single step approximation,

(II) define all possible field solutions for the various regions

$$\underline{x < \bar{x}_o} \quad E_y = A_o e^{\gamma_o x}, \quad H_z = \frac{j\gamma_o}{\omega\mu_o} A_o e^{\gamma_o x} \tag{3.43}$$

$$\underline{\bar{x}_o < x < \bar{x}_1} \quad E_y = A_1 \cos(k_1 x) + B_1 \sin(k_1 x), \tag{3.44}$$

$$H_z = -(k_1/\omega\mu_o) A_1 \sin(k_1 x) + \frac{jk_1}{\omega\mu_o} B_1 \cos(k_1 x)$$

$$\underline{x > \bar{x}_1} \quad E_y = A_2 e^{-\gamma_2 x}, \quad H_z = \frac{-j\gamma_2}{\omega\mu_o} A_2 e^{-\gamma_2 x} \tag{3.45}$$

(III) Match field quantities at the boundaries

$$x = \bar{x}_o: \quad A_o = A_1; \quad \gamma_o A_o - k_1 B_1 = 0 \tag{3.46}$$

$$x = \bar{x}_1: \quad A_1 \cos(k_1 x) + B_1 \sin(k_1 x_1) - A_2 e^{-\gamma_2 x_1} = 0$$

$$-A_1 k_1 \sin(k_1 x) + B_1 k_1 \cos(k_1 x_1) +$$

$$\gamma_2 A_2 e^{-\gamma_2 x_1} = 0 \tag{3.47}$$

This yields 3 equations in 3 unknowns.

(IV) Formulate matrix equations - introduce the normalized transverse depth quantities ($\bar{x} = x/d$)

$$\begin{bmatrix} d\gamma_o & -dk_1 & 0 \\ \cos(k_1 \bar{x}_1 d) & \sin(k_1 \bar{x}_1 d) & -e^{-\gamma_2 x_1 d} \\ -dk_1 \sin(k_1 \bar{x}_1 d) & dk_1 \cos(k_1 \bar{x}_1 d) & d\gamma_2 e^{-\gamma_2 \bar{x}_1 d} \end{bmatrix} \begin{bmatrix} A_1 \\ B_1 \\ A_1 \end{bmatrix} = \emptyset \tag{3.48}$$

or $\quad \Gamma x = 0 \qquad (3.49)$

the matrix dispersion equation is thus:

$$\det \Gamma = 0 \tag{3.50}$$

The number of homogeneous steps employed to model the inhomogeneous structure will dictate the matrix size and hence complexity:

Matrix order = $(2N + 1)$, N = # of steps

Refer to Appendix D for detailed flow charts.

As the number of steps increases, the accuracy of the results improves. The results for single step, double step and five step approximations are graphed together in Fig. 3.8 to demonstrate the aforementioned effect. To maximize accuracy, yet maintain a reasonable matrix size for numerical considerations, a five-step profile was chosen.

The detailed quantization of a Gaussian profile is shown in Fig. 3.9, and a comparison between the WKB and step methods is presented in Fig. 3.10. A comparison in accuracy and execution times for the WKB and step methods is presented below in Table 3.1

Method	Value of V for TE_0	TE_1	TE_2	TE_3	Computing Time
Step	1.75	5.28	8.50	11.8	1.31 sec.
WKB	2.20	5.55	8.75	11.82	0.01 sec.

The V values for both the Step and WKB methods were obtained by setting b = 0.1 . Refer to Fig. 3.10.

Comparison of Various Multi-step Approximations.

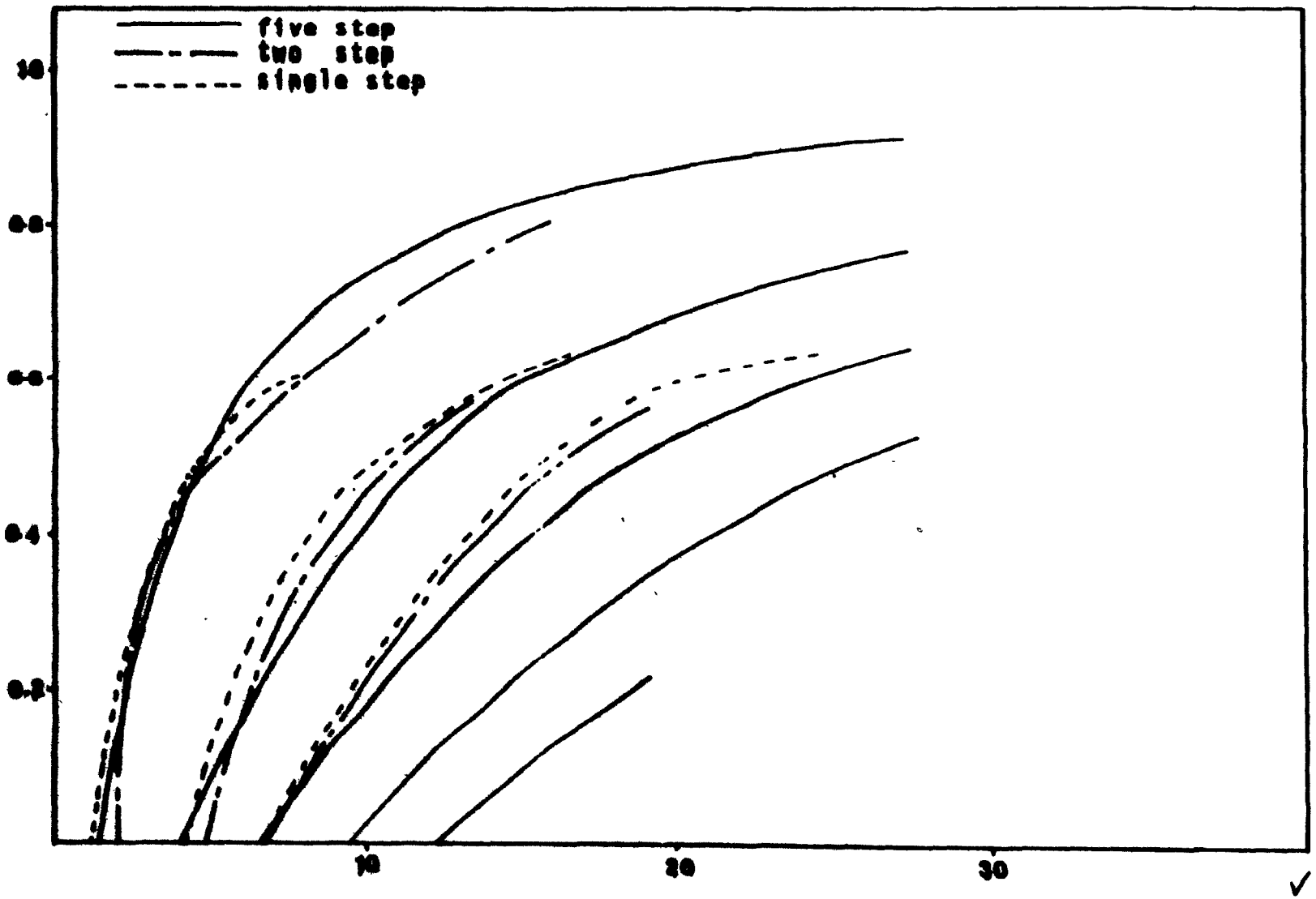

Figure 3.8

Gaussian Profile Quantization. (5 step approximation)

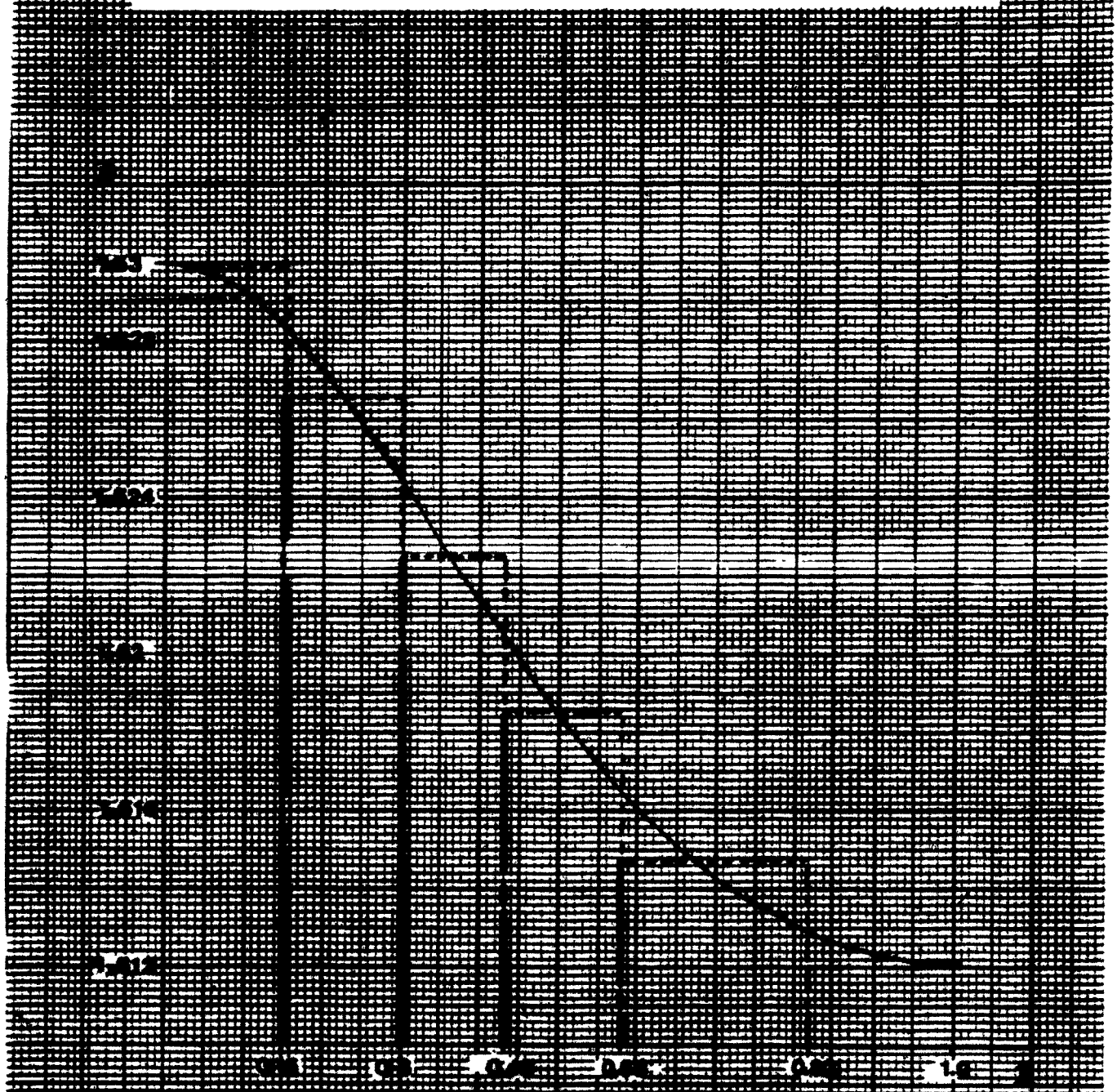

$$n(x) = n_b + \Delta n_s e^{-(x/d)^2}$$

Figure 3.9

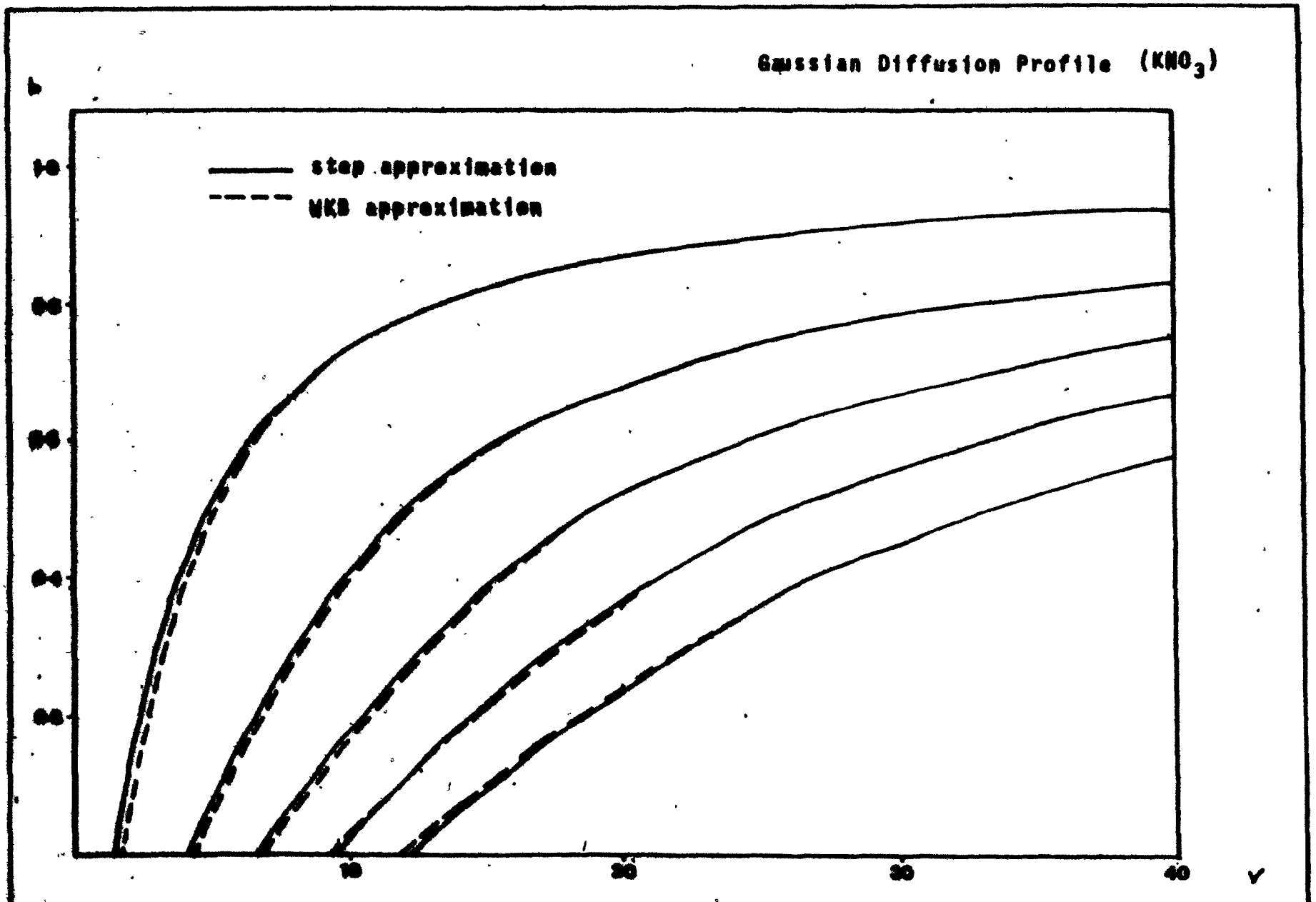
Gaussian Diffusion Profile (KNO_3)
b
step approximation
WKB approximation
1.0
0.8
0.6
0.4
0.2
10
20
30
40
V

Figure 3.10

CHAPTER IV

FABRICATION OF ION EXCHANGED SLAB GUIDES

4.1 Apparatus

The basic equipment necessary for the fabrication of waveguides by the process of ion-exchange includes a furnace, some type of control unit and a dipping system. In order to achieve good repeatability, the control unit must be sufficiently stable to provide a certain measure of thermal stability.

For slab waveguide exchanges in $AgNO_3$, a Lindberg "hevi-duty" furnace and controller were employed. This system is primarily used for semi-conductor fabrication and hence did not perform up to expectation for the ion-exchange process. This is due to the fact that the controller is preset for operating temperatures in excess of 1000°C while the exchange process was subject to a temperature of 245°C. This problem resulted in a poor temperature stability of approximately ± 3°C, not sufficient for good repeatability. The KNO_3 slab guides were exchanged in a vertical furnace with much better thermal stability. The vertical and horizontal furnaces are displayed schematically in Fig. 4.1 and 4.2 respectively. The stability

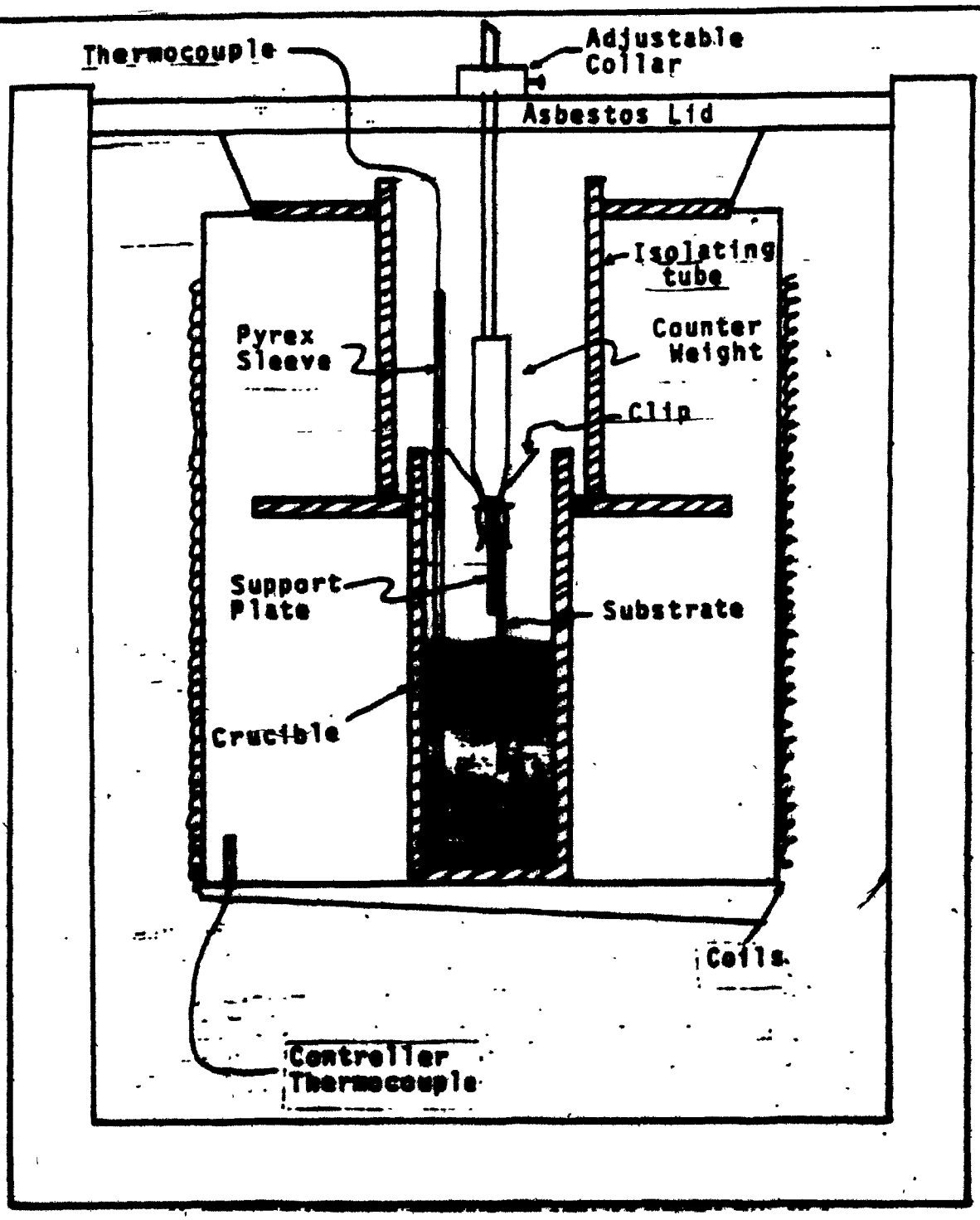

Cross-section of The Ion Exchange Furnace

Insulation

Stainless Steel

Melt

Figure 4.1

ION EXCHANGE FURNACE

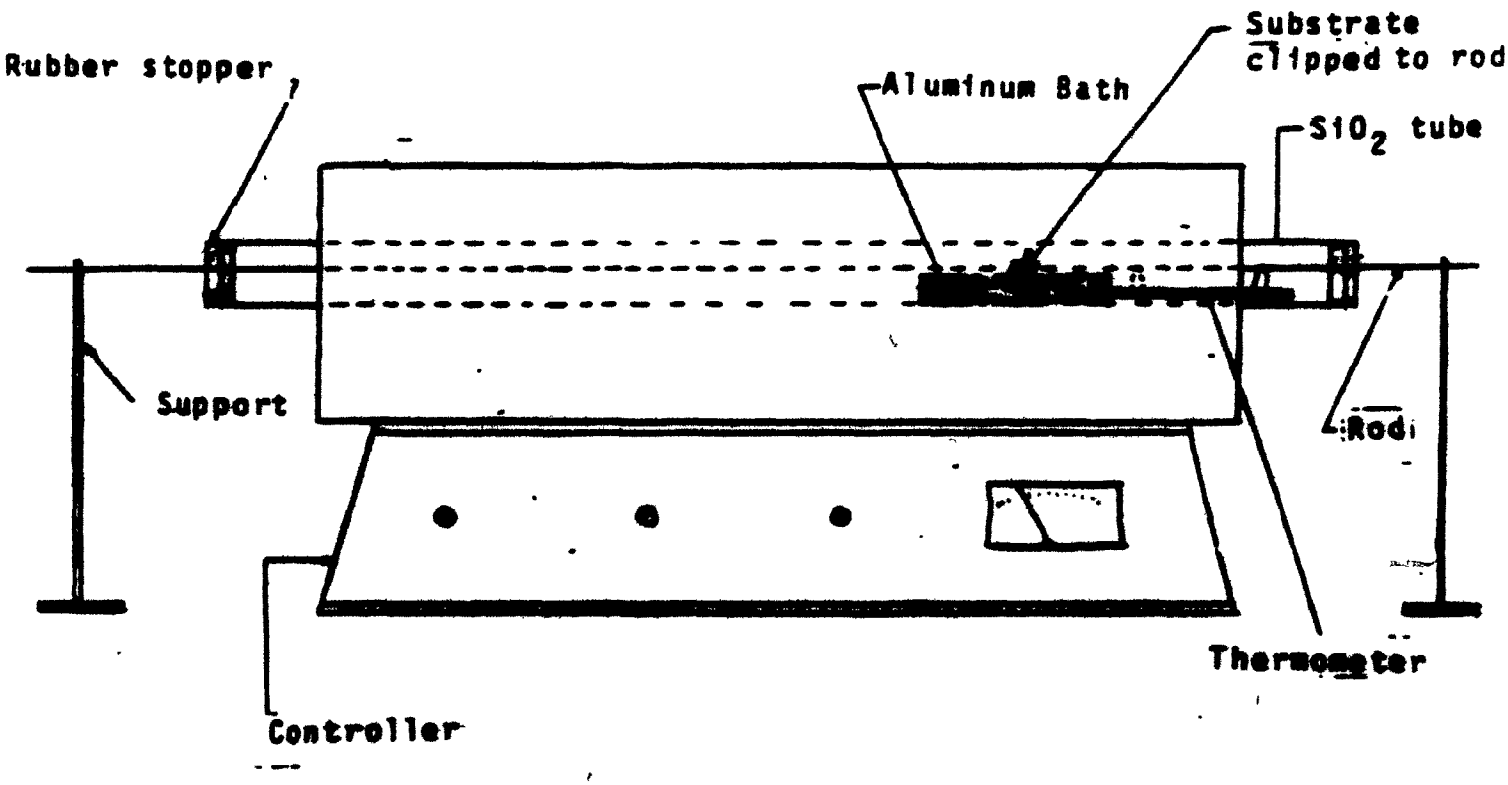

Figure 4.2

of the vertical furnace was maintained with a "J" type thermocouple.

4.2 Substrate preparation

To achieve good quality waveguides with the lowest possible loss figures, the glass substrates must be immaculately cleaned. Soda-line glass substrates manufactured by the Fisher Scientific Corp. were employed. The cleaning process began with washing the substrate with soap and city water with cotton swabs. Following this, the substrate was immersed in nitric acid for 20 minutes. After rinsing with acetone, the substrate was immersed in trichloroethylene, which was brought to its boiling point for 20 minutes. Then the substrate was rinsed with distilled, deionized water and finally it was sonically cleaned in DI water for five minutes. This completed the cleaning process.

4.3 Slab guide fabrication

Slab guide fabrication was relatively simple; as in Fig. 4.2, the cleaned substrate was clipped to the long horizontal rod and then the rod was positioned in the preheated furnace. Both steppers were then positioned, and before the substrate was dipped in the bath by rotation of

the rod, the temperature had to be sufficiently stable. Once a reasonable level of stability was achieved, the rod was rotated and the substrate was immersed in the bath, commencing the exchange process. It should be noted that the substrate was preheated while waiting for temperature stability to be achieved. The $AgNO_3$ slab waveguides were produced in an unstirred, undiluted bath of molten silver nitrate at a temperature of $245^{\circ}C \pm 4^{\circ}$ (on average) for exchange times ranging from 10 minutes up to 160 minutes. A few of the trials were repeated to try to verify repeatability, but this was unfortunately not the case. The waveguides supposedly formed under identical experimental conditions did not exhibit the same number of modes, nor the same M-line separation.

Once the exchange was complete, the substrate was removed from the furnace and was allowed to cool in the air for a few minutes. Following the cooling down, the substrate was cleaned in distilled water to remove residual $AgNO_3$ adhering to the surface of the slide.

4.4 Measurement procedures

To characterize the parameters of the waveguide, light was coupled, via prisms into the structure and the

angular displacement of the resulting M-lines was measured. The angles at which these M-lines appeared were then manipulated into the synchronous coupling angle of the laser itself.

Consider now, the analysis of coupling light into waveguides via prisms.

4.4.1 The prism coupler (38)

In both the prism and grating coupler a light beam is fed into a film, via the broad surface of the substrate. We limit this discussion to the prism coupler.

The prism and guide are coupled over many wavelengths of the incident light, and energy transfer takes place continuously. If the coupling strength of the laser beam and its intensity is uniformly distributed over the coupling length, along with the correct pin pressure on the prism, an efficiency of about 80% can be achieved (38). To excite all possible modes in the waveguide, η_3 prism > η_1 film. Total reflection of the incident beam occurs at the prism base. As a result, the field in the prism is a standing wave that becomes a decaying, evanescent mode below the base of the prism in the air gap.

Decomposing A_3 into its components (Fig.4.4) we see the boundary conditions require that the horizontal components at the prism-gap interface be equal. The evanescent field therefore varies as $e^{-jkn_3 x \sin\theta_3}$ in the direction of propagation. For good optical coupling, the air gap should be approximately 1/8 to 1/4 of the vacuum optical wavelength. The evanescent field in turn excites a light wave in the guide upon penetration of it, an effect known as optical tunneling.

If the horizontal component of either A_1 or B_1 is equal to $kn_3 x \sin\theta$ the corresponding horizontal component of the wave vector in the prism light wave, the incident signal is said to be exclusively coupled to this waveguide mode. Under this situation, the laser light is in a synchronous direction.

Any waveguide mode can be coupled via a proper selection of the incident light; i.e. the waves in the prism and film have the same horizontal wave motion with the same phase: $\rightarrow kn_3 \sin\theta_3 = kn_1 \sin\theta$.

As shown in Fig.4.5, the two evanescent tails of the fields in the prism and guide overlap in the air gap constituting the coupling effect. Energy is continuously trans-

Fig. 4.3 Ray Optics

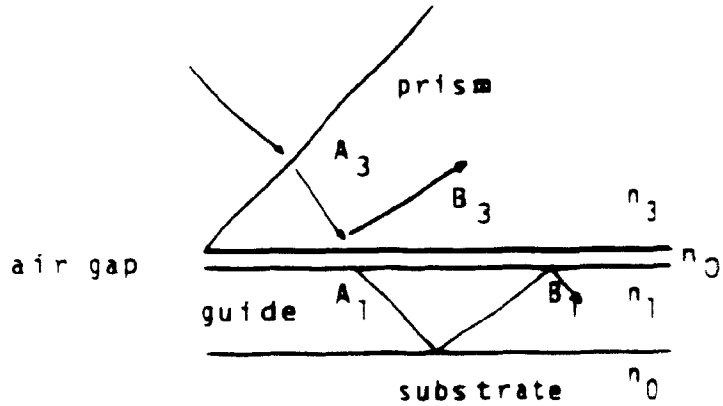

Fig. 4.4 Reference Angles

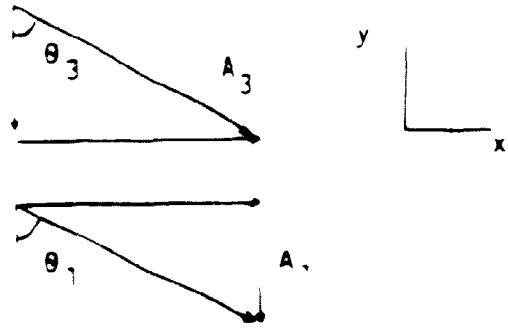

Fig. 4.5 Coupling Mechanism

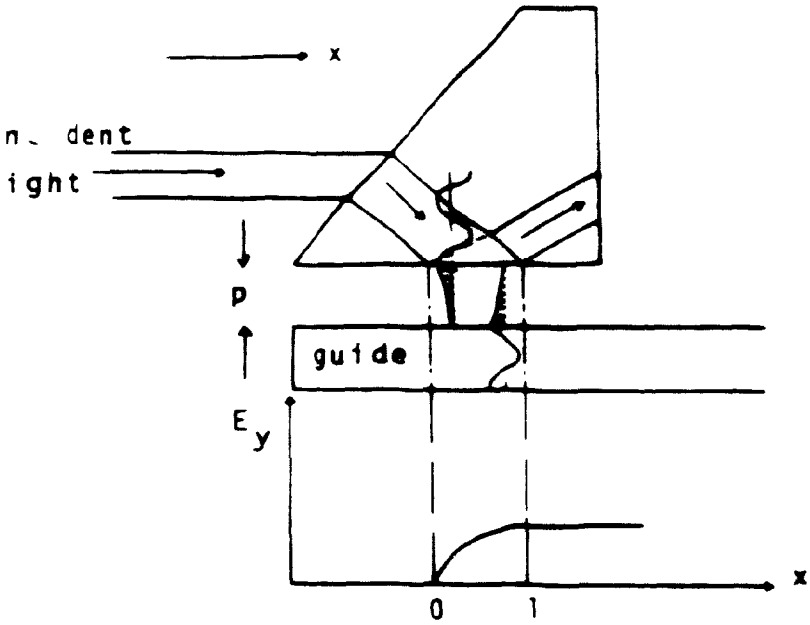

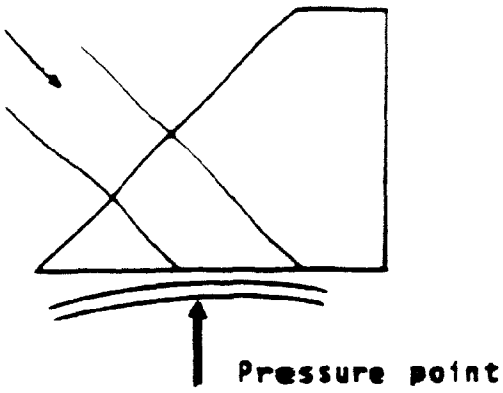

Fig. 4.6

fered from the prism to the guide along the coupling length (38)

If the film is bent such that the gap is narrow at x = 0 and wider at the rectangular end of the prism, enhanced coupling occurs (Fig 4 6)

4 4 2 Measurement Apparatus

The measuring set-up required for launching the waveguide modes consists of a rotational stage with 4 degrees of freedom, a prism and substrate holder, a screen, lens and a He-Ne laser light source The complete set-up is shown in the schematic of Fig 4 7

As can be seen from Fig 4.7 when the laser beam is incident in a synchronous direction, (i e. the phase matching condition is met) guided modes are successfully excited and the following relation exists (24)

$$\theta = \sin^{-1}(n_p \sin(\sin^{-1}(N_{eff}/n_p)-\alpha)) \qquad (4.1)$$

$$N_{eff} = (n_p \sin(\sin^{-1}(\sin\theta/n_p) + \alpha))$$

n_p prism index α. prism angle

θ synchronous angle

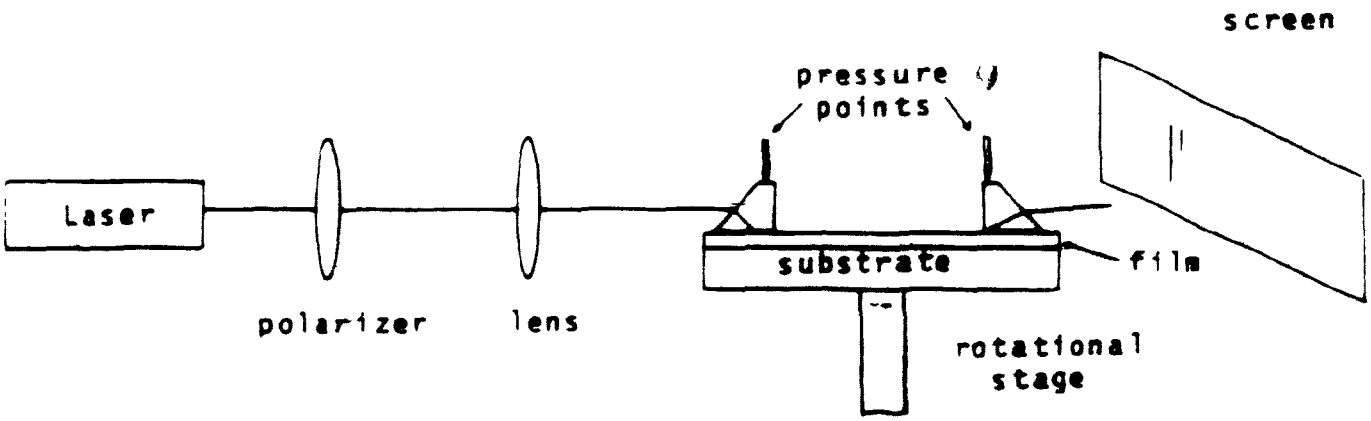

Figure 4.7 Measurement Configuration

Before attempting to measure the synchronous angles, both the prisms and the guide were thoroughly cleaned in ethanol. If the interface between the prism and guide was contaminated, there would have been a marked reduction in the coupling efficiency. After cleaning, the prisms and the guide were secured on the rotational stage.

At this point in the procedure, the securing pins had to be adjusted so that the sharpest possible set of M-lines could be viewed. To get the sharpest M-lines, the input and output securing pins were adjusted so that a light and even pressure on the prism was attained. Once the adjustment was complete, the securing pins could not be touched, else measurement errors would result.

The next step in the procedure was to get a zero reference point. This was necessary because we did not read the synchronous angle of the laser directly from the rotational stage. The synchronous angle was calculated by subtracting the angle read from the rotational stage, from the zero reference angle. To set the zero reference angle, the stage was rotated until the input face of the input prism was perpendicular to the incident laser light. A screen was positioned directly behind the rotational stage, in line with the laser beam (Fig.4.8). To locate a zero reference point,

a pattern of Newton's rings must be found By fine adjustment of the angular rotation of the stage, these rings would appear on the s reen The zer referen e point was precisely at this angular displacement

This measurement was perf rmed several times so that the average of all the tr als would closely correspond to the true zer referen e point (see Appendix I

The angular displacement of the individual M-lines could then be measured The stage was rotated in a clockwise fashion (Fig 4) from the zero reference angle until the pattern was in view again and this adjustment was finely tuned until the line at the far right of the pattern was as bright as possible In this case, light was coupled to the first mode For accuracy, this measurement should be repeated four or five times Performing the adjustment for each M line appearing in the pattern, and averaging the values for each trial completed the set of measurements for that guide

These results could then be manipulated in order to calculate the refractive index profile and guide depth

First, the synchronous angles of the laser cor-

responding to each mode were calculated by subtracting the measured angles from the zero reference angle. Then the effective refractive index for each mode was calculated by the use of (4.1). These calculations are shown on the next page for four different slab waveguides.

4.5 Experimental Results

Table 4.1 $AgNO_3$ Slab Waveguide Data

All measurements were performed with TAFD prism

(n_p = 2.019)

α_p = 45°

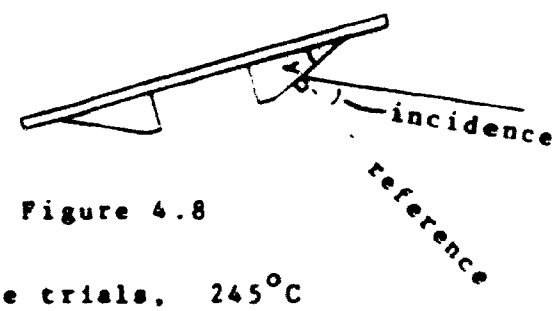

Figure 4.8

(4.1 a) 10 minute trials, 245°C

	MODE	ANGLE OF INCIDENCE (°)	N_{eff}
Sample I	1	13.319	1.581
	2	11.550	1.562
	3	10.033	1.546
	4	8.540	1.529
	5	6.150	1.501
Sample II	1	11.5111	1.5618
	2	9.0951	1.5350
	3	7.4731	1.5167

Discrepancies in the above data can be attested to the fact that stability of temperature was difficult to achieve. In the first trial rubber stoppers were not employed hence temperature variation was more extreme. Another contributing factor is depletion of silver ions in the melt; Sample I was performed with a fresh melt, while Sample II took place some 6 trials later.

(4.1 b) 40 minute trials, 245°C

	MODE	ANGLE OF INCIDENCE (°)	N_{eff}
Sample I	1	14.603	1.595
	2	13.182	1.580
	3	12.058	1.568
	4	10.903	1.555
	5	9.850	1.543
	6	8.749	1.531
Sample II	1	13.8997	1.5874
	2	12.6514	1.5741
	3	11.5504	1.5622
	4	10.6358	1.5522
	5	9.6333	1.5411
	6	8.6792	1.5304
	7	7.7153	1.5194

The above two trials were fabricated under supposedly identical conditions, but just as for the 10 minute trials, temperature instability (due to heat radiation from uninsulated apparatus and poor thermocouple performance in the given temperature range) can take the blame for the discrepancy.

(4.1.c) 90 minute trial, 245°C

MODE	ANGLE OF INCIDENCE (°)	N_{eff}
1	14.715	1.596
2	13.633	1.585
3	12.665	1.574
4	11.663	1.563
5	10.924	1.555
6	9.351	1.538
7	9.153	1.536
8	8.349	1.527

(4.1.d) 160 minute trial, 245°C

MODE	ANGLE OF INCIDENCE (°)	N_{eff}
1	16.277	1.612
2	15.048	1.599
3	14.351	1.592
4	12.471	1.572
5	11.697	1.564
6	11.043	1.557
7	10.204	1.547
8	9.506	1.540
9	8.785	1.532
10	8.113	1.524

Photographs of the m-line outputs from the $AgNO_3$ slab samples are included in Fig. 4.9 (a)-(c). The M-lines are ordered m = 0,1,2... from left to right. The picture of Fig. 4.10 shows an ion-exchanged $AgNO_3$ slab guide. Note the yellowing of the exchanged area: this is an undesirable effect, causing surface imperfections due to an excessive exchange temperature.

4.6 Refractive Index Profiles of $AgNO_3$ Slabs

All refractive index profiles presented in this chapter are based on an algorithm outlined by Heidrich & White (22). The theory behind profiling by the WKB method has been presented in Chapter 3, section 3, while the software and flowchart is presented in Appendix C.

As explained in Chapter 3, a good approximation to the surface index is required to start the procedural calculation. The surface index can be estimated by plotting the right hand side of the WKB integral

$$k_o \int_0^{z_t} (n^2(z) - N_{eff}^2)^{\frac{1}{2}} \, dz = \phi_1 + \phi_2 + m\pi$$

$$(\phi_1 = \pi/2, \ \phi_2 = \pi/4 \quad m = 0,1,2...) \qquad (4.2)$$

versus the set of effective mode indices.

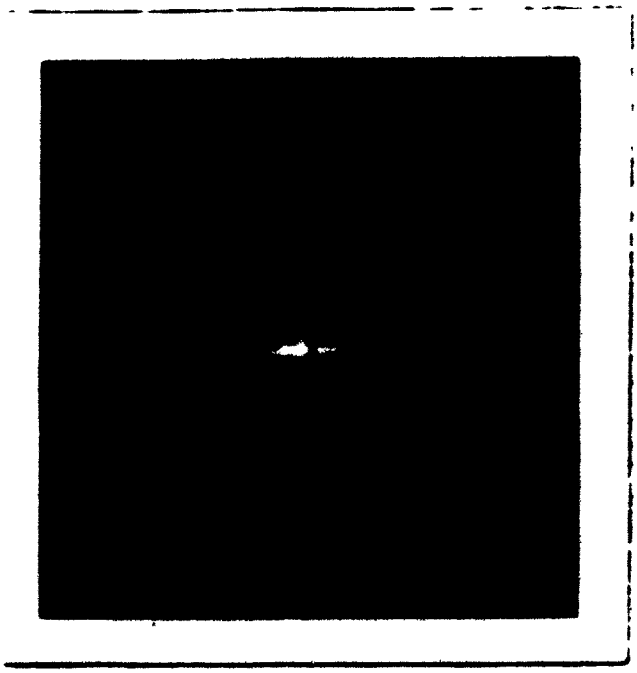

(a) 10 min. 235 °C (I)

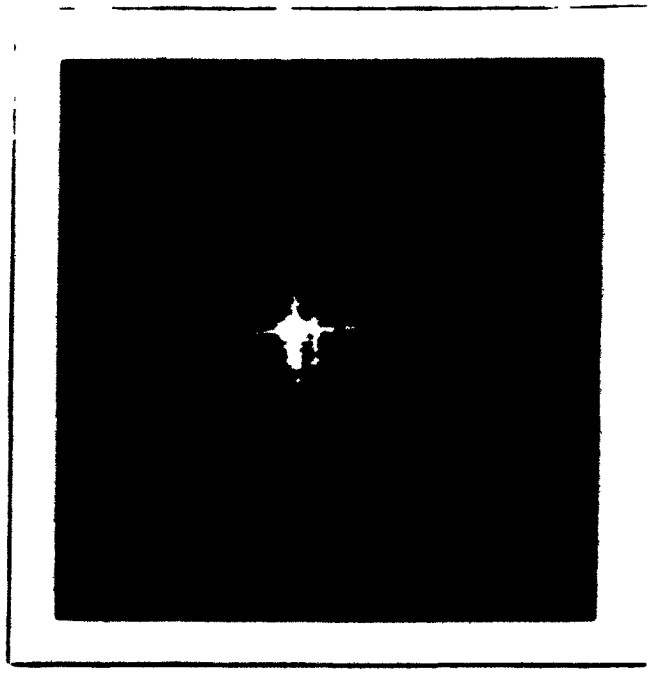

(b) 40 min. 245 °C (II)

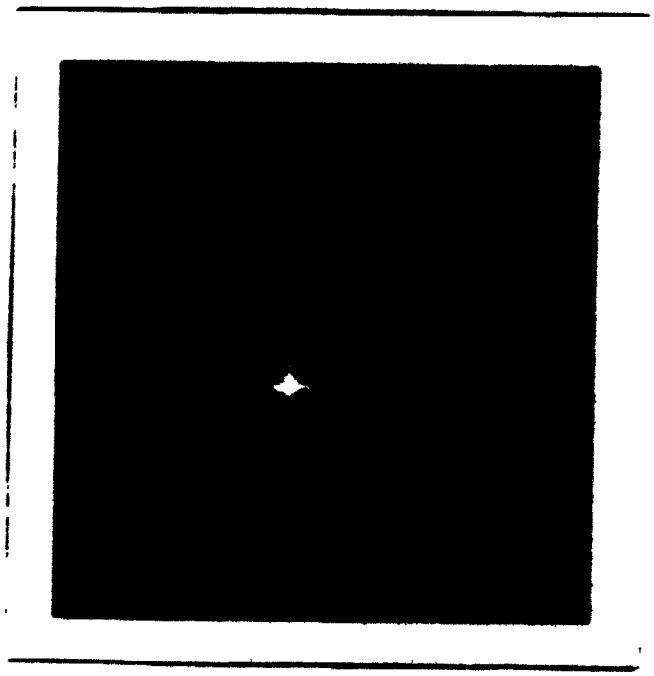

(c) 90 min. 245 °C

Figure 4.9

Selected $AgNO_3$ M-line Photos

Yellowing of Substrate

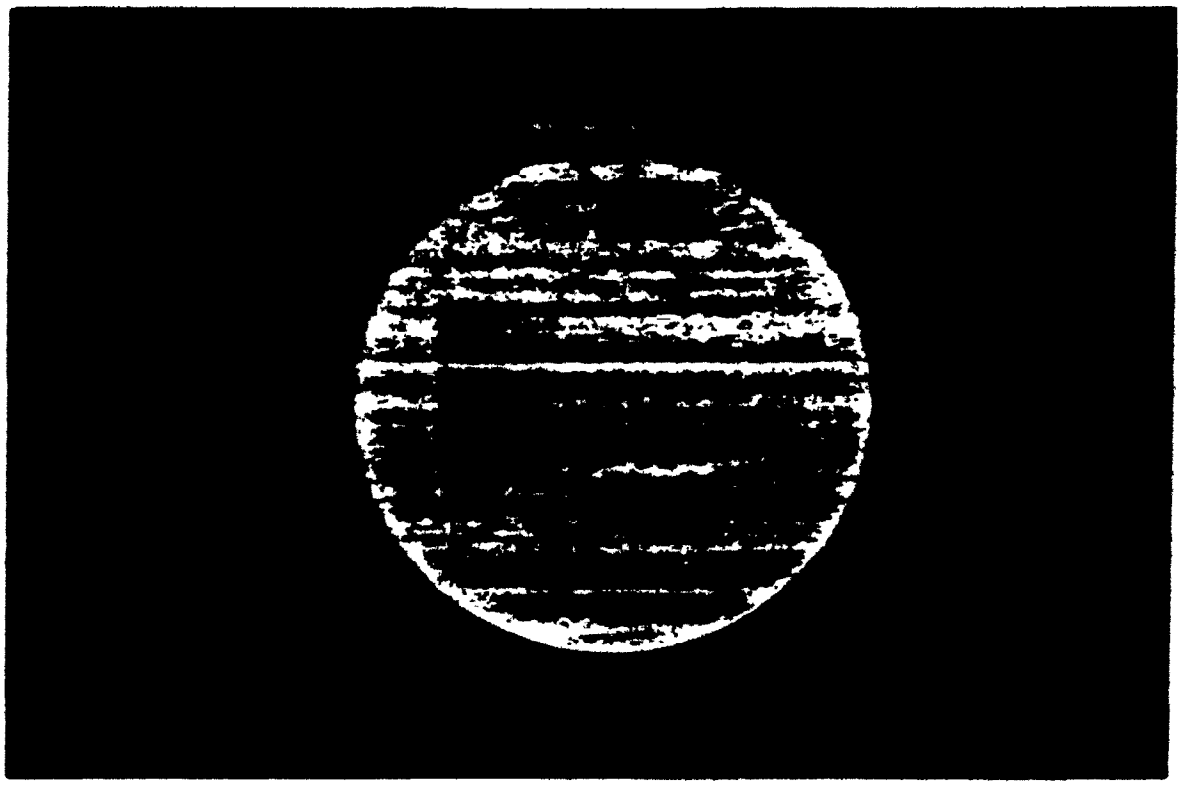

Figure 4.10

The surface index will be estimated as the intersection between the curve and the x-axis. The approximation is outlined for various $AgNO_3$ trials in Fig. 4.11 a-d.

Following these figures are the actual refractive index profiles for the $AgNO_3$ guides. The best free-hand curve is drawn for the given set of data points in each case. Refer to Fig. 4.12 a-b.

It was noted in Chapter 3, section 3, that the initial selection of the surface refractive index is critical in determining the accuracy of the refractive index profile. Since these surface index values are used to normalize the measured effective mode indices, a necessary procedure for correlating theoretical and experimental dispersion curves of inhomogeneous waveguides, a comparison of results yielded by both methods are presented in Table 4.2.

Trial	WKB Integral	Refractive Index Profile
10 min, 245°C (I)	1.596	1.597
40 min. 245°C (I)	1.602	1.600
90 min. 245°C	1.602	1.603
160 min. 245°C	1.620	1.622

Table 4.2 Comparison of surface refractive index values for $AgNO_3$ trials.

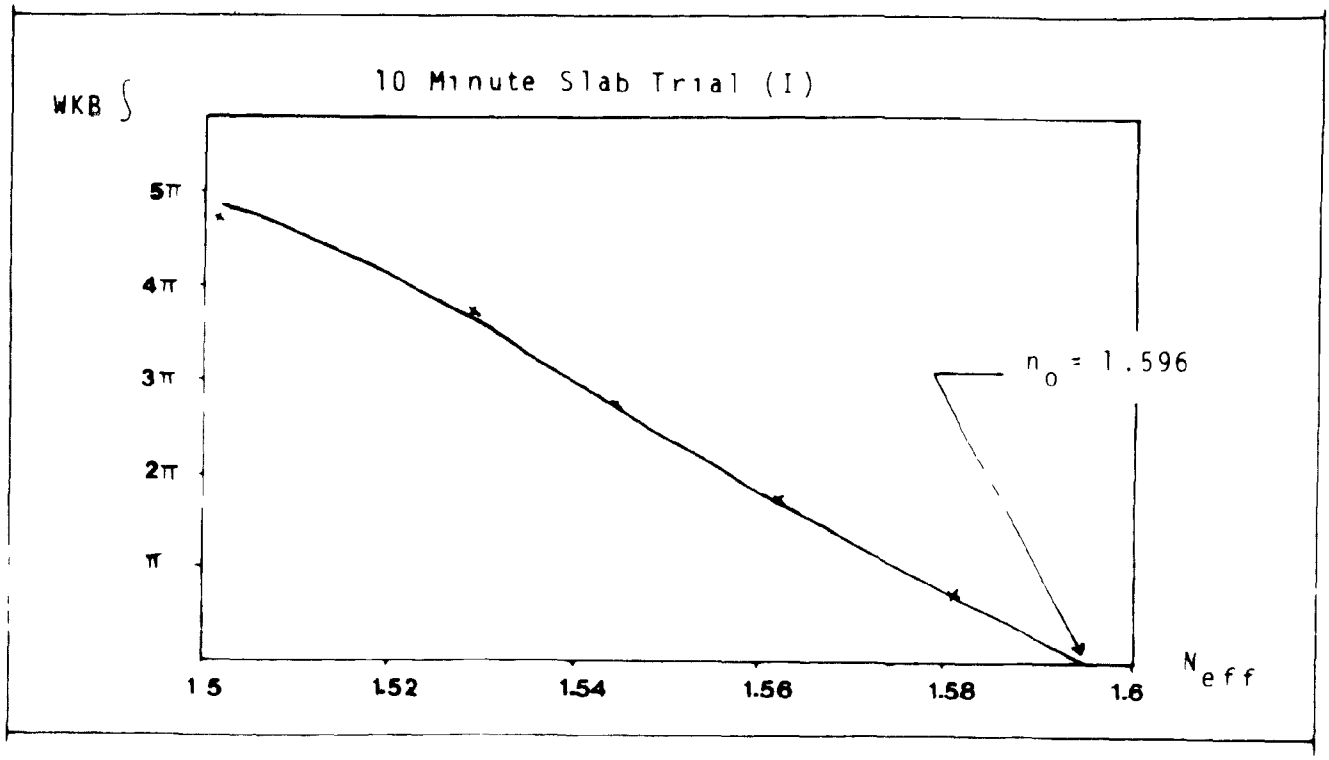

(a)

Measured mode indices plotted on universal curves of $m\pi + \pi/4 + \phi_0$

$\phi_0 \cong \pi/2$ n_0 = surface index

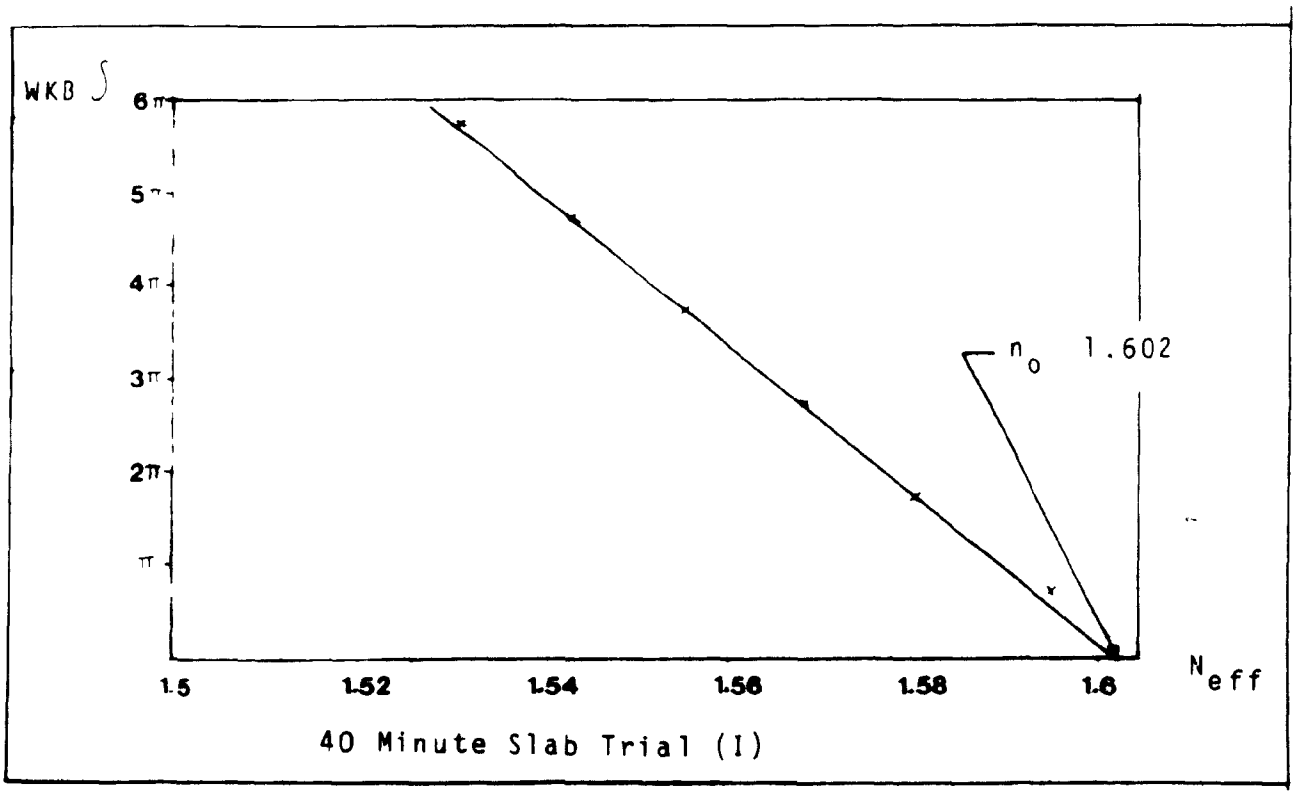

(b)

Figure 4. 11

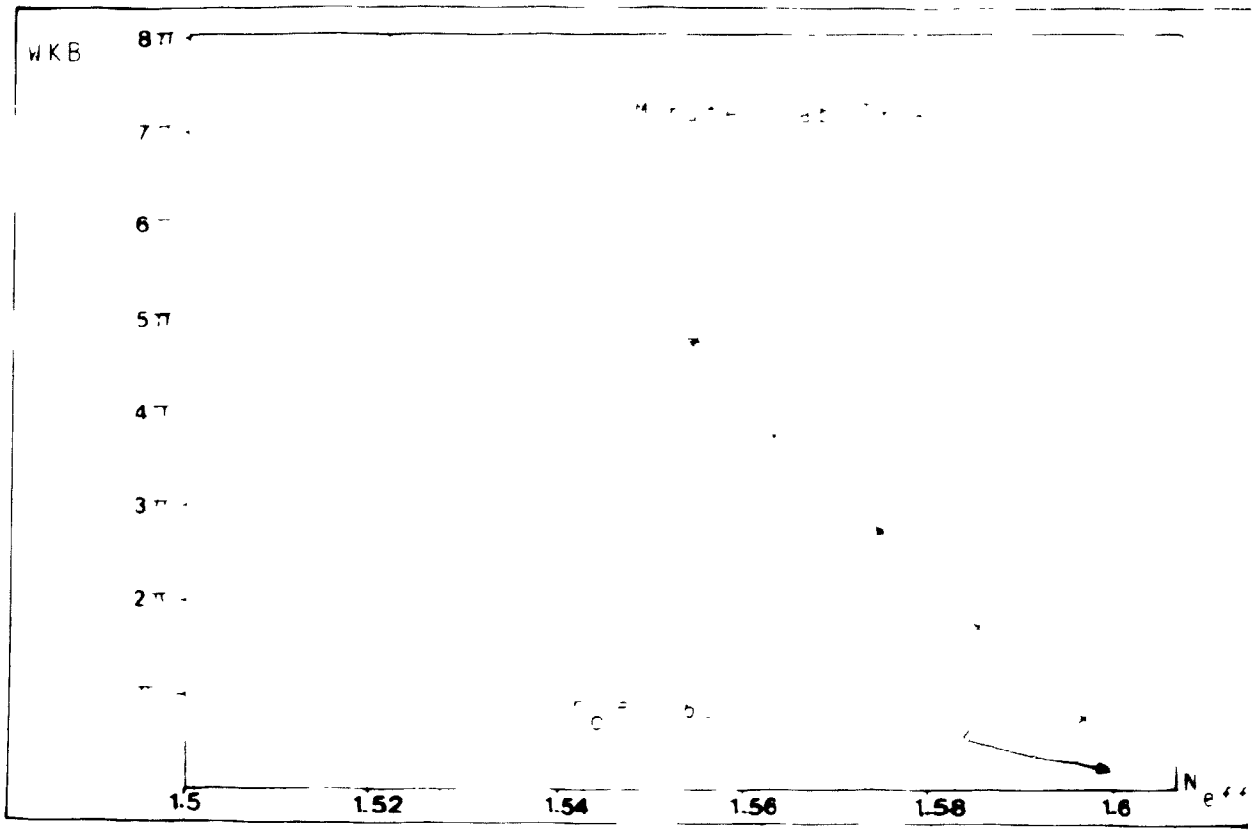
WKB
8π
7π
6π
5π
4π
3π
2π
1.5
1.52
1.54
1.56
1.58
1.6
N

WKB S

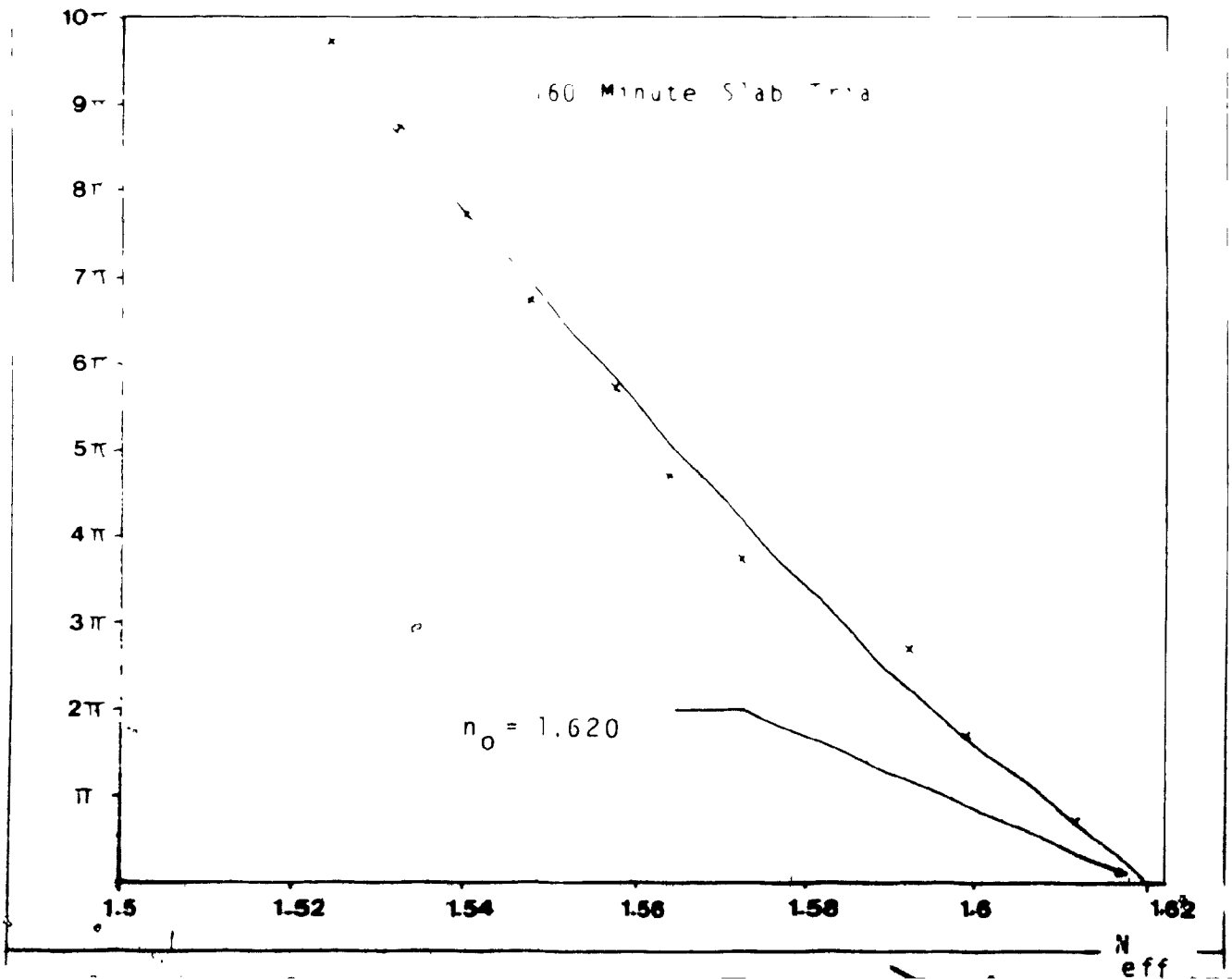
10π
9π
8π
7π
6π
5π
4π
3π
2π
π
60 Minute Slab
n_o = 1.620
1.5
1.52
1.54
1.56
1.58
1.6
1.62
N
eff

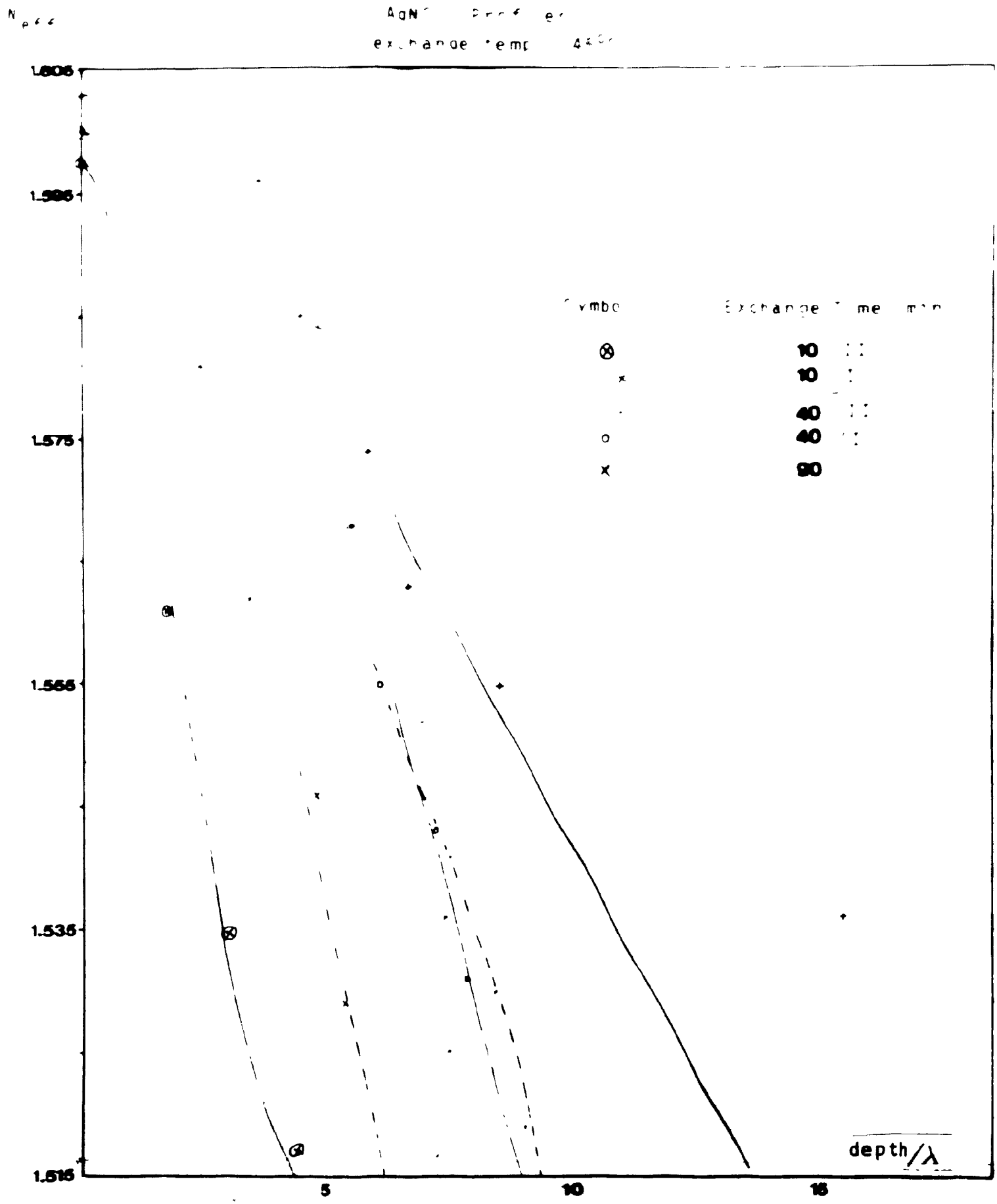

Figure 4.12 (a)

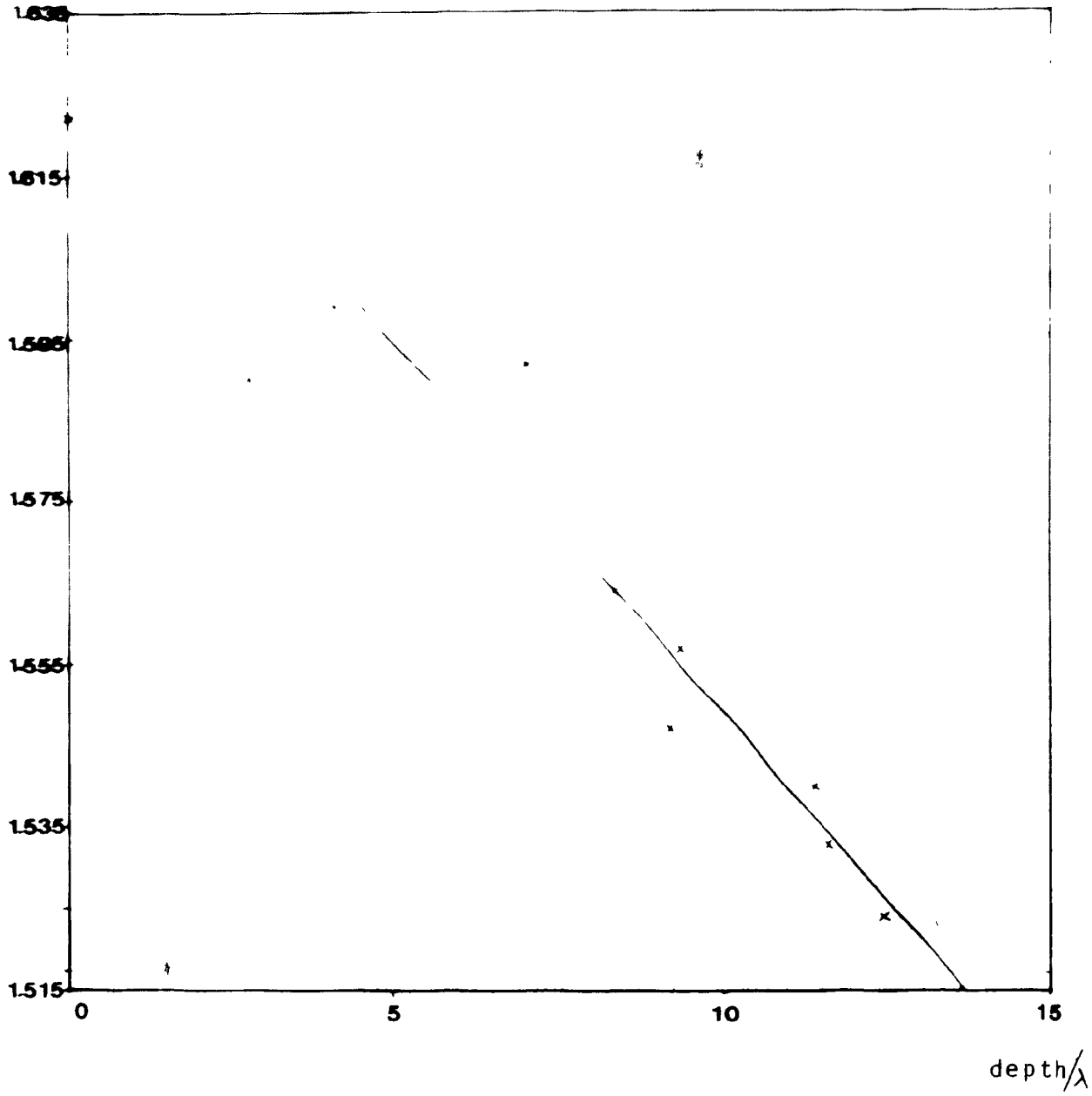

160 minutes, 245 °C

The agreement between both methods appear to be quite good, with a maximum deviation of 0.002 in the 40 and 160 minutes trial.

4.7 Temperature Variation and Diluted $AgNO_3$ Melts

4.7.1 Temperature variation

All previous $AgNO_3$ slab trials were fabricated at 245°C. In this section, the effects of variation of temperature are investigated.

According to diffusion theory (31), we expect that as the temperature of the melt increases, the same guide depth achieved at a lower temperature is attainable in less time. This is evident by examining the equations for diffusion depth;

$$d = 2\sqrt{Dt}, \qquad t = \text{diffusion time} \tag{4.3}$$

$$D = Do \exp(-Ea/KT) \qquad Ea = \text{activation energy} \tag{4.4}$$

It is obvious from equation (4.4) that as the temperature increases, so does the coefficient of diffusivity and hence the diffusion depth d.

One might think that to speed up the fabrication process, one needs only to increase the melt temperature. This functions up until a certain point. If the temperature is at an upper extreme, a brownish yellow discoloration of the substrate becomes evident. The discoloration worsens with increasing temperatures and is due to the presence of free silver at the substrate surface, contributing to waveguide losses (Fig. 4.10).

Table 4.3 shows the effects of temperature on the effective mode indices for various thermal conditions, time being held constant at 10 minutes.

Table 4.3 Temperature Variation

(I) 235°C trial

MODE	ANGLE OF INCIDENCE (°)	N_{eff}
1	14.9056	1.5979
2	13.5670	1.5030
3	12.0417	1.5675
4	10.6014	1.5518

Table 4.3 (cont'd)

(II) 260°C trial

MODE	ANGLE OF INCIDENCE (°)	n_{eff}
1	15.2713	1.6017
2	14.1796	1.5903
3	13.2222	1.5802
4	12.4181	1.5716
5	11.7009	1.5638
6	10.9371	1.5555
7	10.2565	1.5480
8	9.5325	1.5399
9	8.9384	1.5333
10	8.3176	1.5263
11	7.4454	1.5163

(III) 315°C trial

Mode	Angle of Incidence (°)	N_{eff}
1	15.8351	1.6075
2	15.0379	1.5993
3	14.3171	1.5918
4	13.7504	1.5858
5	13.3365	1.5814
6	12.8138	1.5758
7	12.3092	1.5704
8	11.6810	1.5636
9	11.4204	1.5608
10	11.0453	1.5567
11	10.6041	1.5518
12	10.0523	1.5457
13	9.7776	1.5427
14	9.2060	1.5363
15	8.7828	1.5315
16	8.5157	1.5285
17	8.1495	1.5244
18	7.8037	1.5204
19	7.5259	1.5173

The effects of temperature on the refractive index profiles of $AgNO_3$ exchanged waveguides are presented in Fig. 4.13. It is evident that as the melt temperature increases, the surface index increases and there is a corresponding increase in the guide depth. These results were

$AgNO_3$ Profiles
(exchange time: 10 min.)

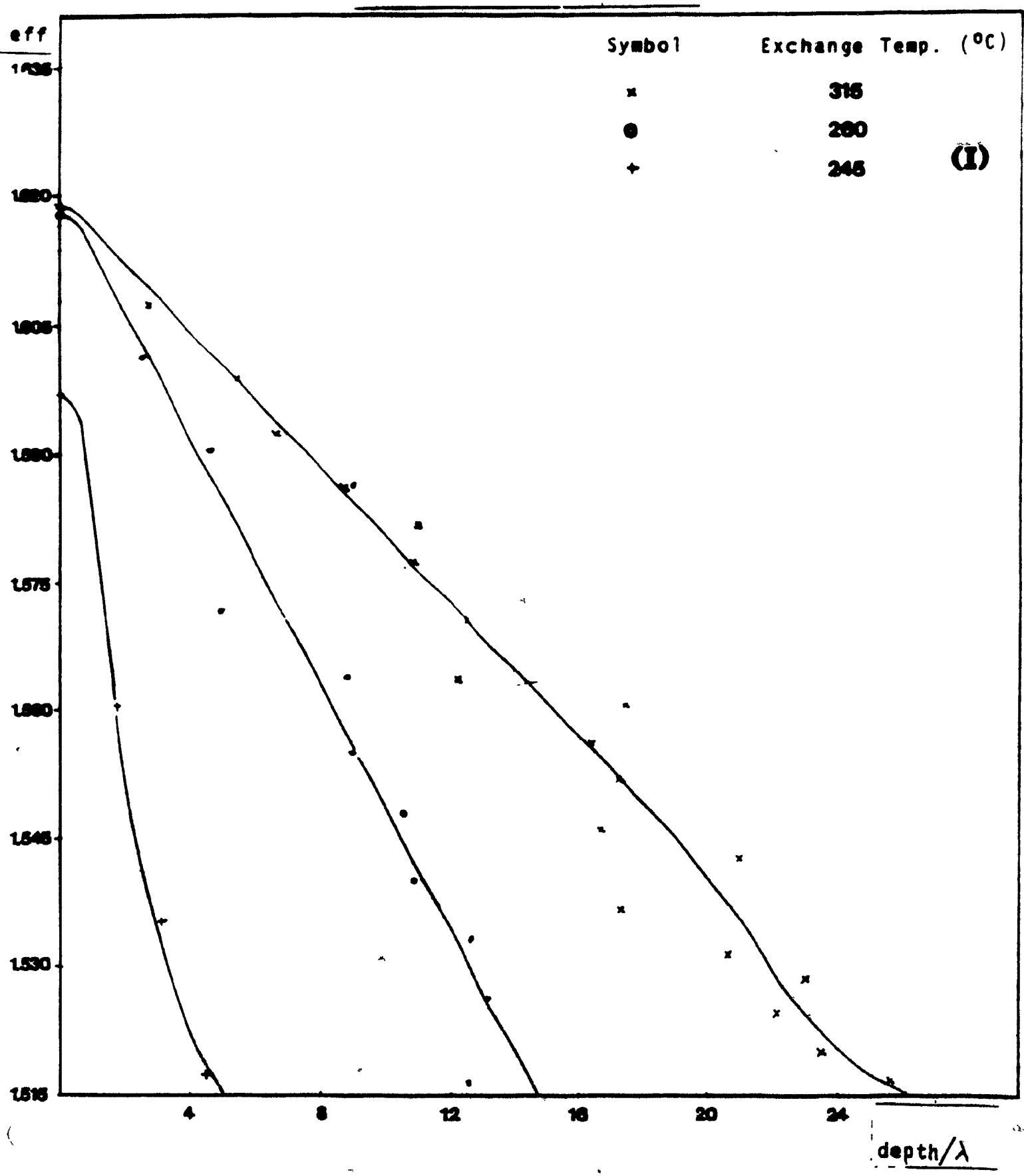

Figure 4.13.

expected as per equations 4.3, 4.4.

Table 4.3 clearly shows an increase in the number of modes as the temperature is increased (time being constant).

4.7.2 Diluted melts ($AgNO_3$)

To investigate the effects of dilution on an $AgNO_3$ melt, four different Ag-Na melt preparations were considered with a 22 gram base of $NaNO_3$ in crystal form. Values of the melt mole ratio M_B/M_A were kept below 0.1 since significant reductions of the surface index are observed in this region.

The various melts were prepared following simple chemical relations along with the atomic weights of the elements involved.

$AgNO_3$: 169.87 A.W. (See Appendix F)

$NaNO_3$: 85 A.W.

Table 4.4. Melt Preparation (22 gram base) $NaNO_3$

Trial	Melt-mole ratio (m_B/m_A)	grams $AgNO_3$
1	0.001	0.0439
2	0.01	0.439
3	0.05	2.12
4	0.1	4.39

Since the melting point of pure $NaNO_3$ is about 307°C, all trials were performed at T = 315°C for 30 minutes to insure liquefaction of the crystals even in the most dilute case.

Upon exciting the modes via the He-Ne laser, it was immediately evident that these guides formed by diluted melts were much less leasy. The familiar bright streak seen in connection with the pure $AgNO_3$ guides was much reduced in intensity and more well-defined, indicating low loss or good guidance. The resulting M-line patterns of these guides were also better defined with strong central maxima but little light intensity in between the individual M-lines. (Fig.4.14)

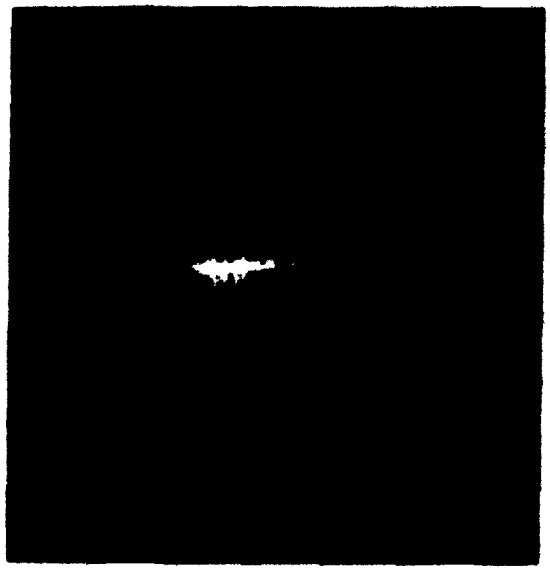

M line structure for a slab guide

exchanged in a dilute silver melt; $m_b/m_a = 0.1$

exchange time: 30 min.
exchange temp.: 315 C

Figure 4.14

It is evident that lowering the silver concentration reduces the surface index. Previous analysis of the resulting refractive index profile by computer program yields that the profile can be modelled by a 2nd order polynomial and that it approachs the erfc distribution as dilution increases (13). See Fig. 4.15

Data for $AgNO_3$ - N_aNO_3 Dilute Melt System

Table 4.5

Trial (1) m_B/m_A = 0.001 T = 315°C, t = 30 min. for all trials

MODE	ANGLE OF INCIDENCE (°)	N_{eff}
1	8.8796	1.5326
2	8.4292	1.5275
3	8.0894	1.5237
4	7.8366	1.5208

Trial (2) m_B/m_A = 0 01

MODE	ANGLE OF INCIDENCE (°)	N_{eff}
1	13.6958	1.5852
2	13.3729	1.5818
3	13.1173	1.5791
4	12.1173	1.5769
5	12.5891	1.5734
6	12.4382	1.5718
7	12.2396	1.5697
8	12.0437	1.5675
9	11.8687	1.5657
10	11.6625	1.5634
11	11.4930	1.5616
12	11.2139	1.5585
13	11.0472	1.5567
14	10.8465	1.5545
15	10.6616	1.5525
16	10.4930	1.5506
17	10.3000	1.5485
18	10.1194	1.5465
19	9.9673	1.5448
20	9.7625	1.5425
21	9.6041	1.5407
22	9.4458	1.5390
23	9.2555	1.5368
24	9.0875	1.5350
25	8.9125	1.5330
26	8.7541	1.5312
27	8.6137	1.5296
28	8.5423	1.5288

DATA (cont'd)

Trial (3) m_B/m_A = 0.05

MODE	ANGLE OF INCIDENCE (°)	N_{eff}
1	15.1333	1.6003
2	14.5556	1.5943
3	14.0681	1.5891
4	13.7347	1.3836
5	13.3549	1.5816
6	13.0674	1.5785
7	12.6833	1.5744
8	12.4236	1.5716
9	12.1056	1.5682
10	11.8250	1.5652
11	11.5285	1.5620
12	11.2833	1.5593
13	11.0257	1.5565
14	10.7097	1.5530
15	10.4215	1.5498
16	10.1757	1.5471
17	9.9285	1.5444
18	9.6563	1.5413
19	9.3840	1.5283
20	9.1445	1.5356
21	8.9083	1.5329
22	8.6806	1.5304
23	8.4722	1.5280
24	8.2806	1.5258

Trial (4) $m_B/m_A = 0.1$

MODE	ANGLE OF INCIDENCE (°)	N_{eff}
1	16.0903	1.6101
2	15.5000	1.6041
3	15.0777	1.5996
4	14.7000	1.5958
5	14.3778	1.5924
6	14.0680	1.5891
7	13.7812	1.5861
8	13.4889	1.5830
9	13.1944	1.5799
10	12.9396	1.5772
11	12.6819	1.5744
12	12.4035	1.5714
13	12.1701	1.5689
14	11.9278	1.5663
15	11.6785	1.5636
16	11.3791	1.5603
17	11.2069	1.5584
18	10.9410	1.5555
19	10.6903	1.5528
20	10.4736	1.5504
21	10.2361	1.5478
22	9.9916	1.5451
23	9.7430	1.5423
24	9.5201	1.5398
25	9.2757	1.5371
26	9.0854	1.5349
27	8.8416	1.5322
28	8.6396	1.5299
29	8.4314	1.15278
30	8.2903	1.5260
31	8.1736	1.5246
32	7.9868	1.5225

Diluted $AgNO_3$ Profiles

(time: 30 min. , temp: 315 °C.)

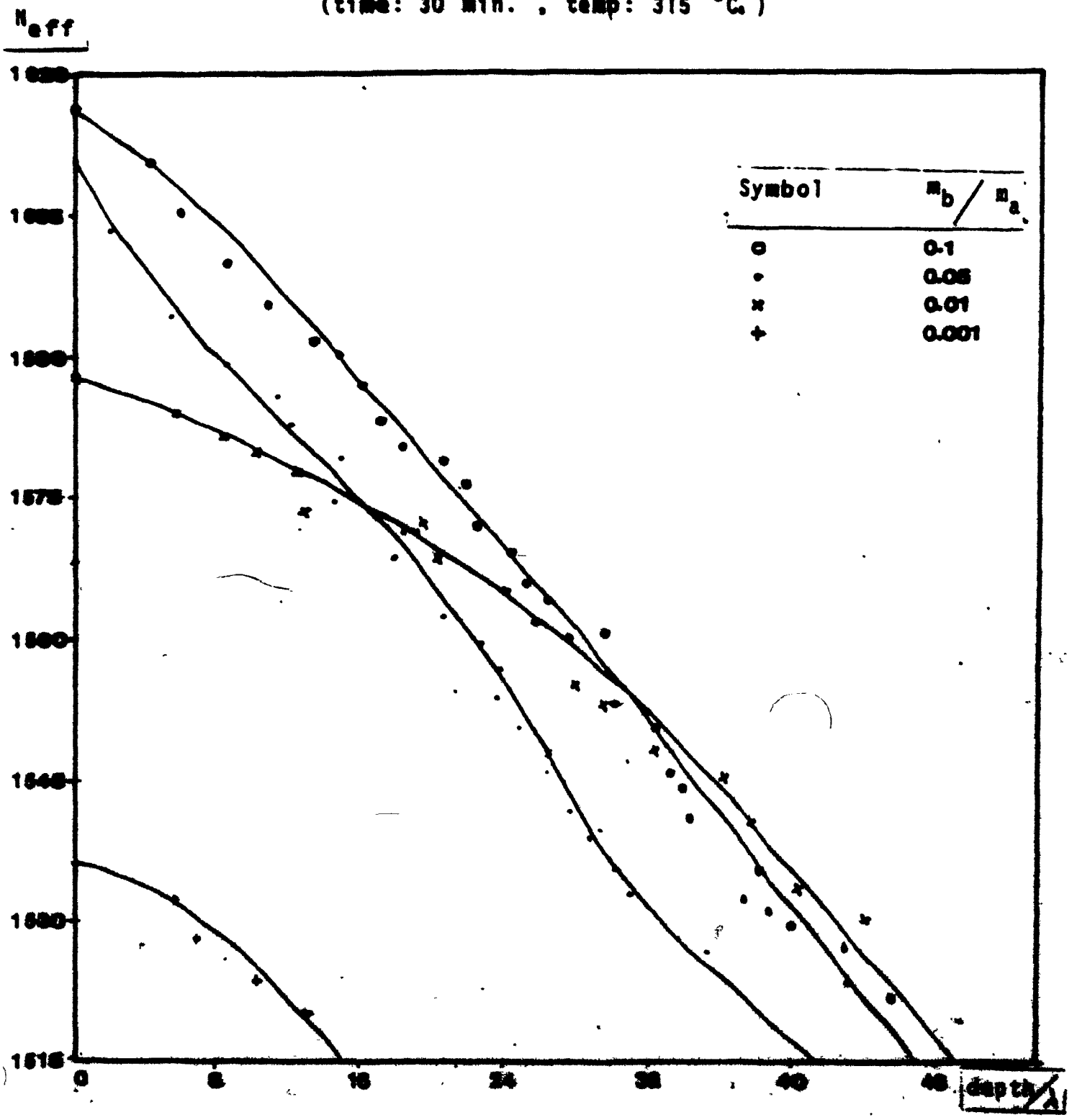

Figure 4.15

Fig. 4.14 includes a photograph of the M-line output of an $AgNO_3$ guide formed in a diluted melt $m_B/m_A = 0.1$. Note the large number of modes and the improved sharpness of each line compared to the previous photos for the pure $AgNO_3$ exchanged samples. The M-lines are ordered $M = 0,1,2...$ from left to right.

4.7.3 Refractive index profiles of various waveguides formed by diluted melts

It is evident that the surface index decreases as melt dilution increases, (see Fig. 4.15) so the surface index value can be controlled. Index profiles obtained with dilute melts can be modelled by second-order polynomials and for very dilute melts, the profile approaches an erfc distribution distribution. (13).

The refractive index profiles of guides fabricated in various diluted $AgNO_3$ melts, were constructed from the data points N_{eff_M}, z_M obtained by the White & Heidrich (22) profiling routine. These curves are presented in Fig. 4.15.

4.8 Slab Waveguides Formed By K^+ Ion Exchange

In this section, we examine the effects of a KNO_3 melt interacting with soda-lime substrates at an index of refraction, $n = 1.517$.

In this situation, the exchange species is the K^+ ion, whose rate of migration is slower than that of the Ag^+ ion. In spite of the fact that the melting point of KNO_3 is considerably higher than $AgNO_3$, it takes a larger diffusion period to achieve the same guide depth as in the case of $AgNO_3$. Even in the case of the most dilute $AgNO_3$-$NaNO_3$ system, single mode guides were fabricated in minutes at temperatures below the melting point of KNO_3. The equivalent guide fabricated in a KNO_3 melt takes the better part of an hour.

The fact that the diffusion time is greatly increased tends to relax the temperature stability requirements. This is a desirable effect for manufacturing processes. Secondly, the refractive index change induced by the K^+ exchange is considerably reduced, compared to an Ag^+ exchange. Typically, we expect a surface index of the order of 1.526 as opposed to 1.60 as measured in the Ag^+ case. Naturally, this will have effects on the propagation of incident light and we should observe more weakly-guided modes, consistent with the reduced change in the refractive index.

This phenomenon of reduced confinement of the modes shall be employed for the mechanism of light coupling by evanescent modes as in a directional coupler. By employing the strong evanescent fields from channel guides, the requirements on the channel separation shall be relaxed, making K^+ guides very attractive for this type of operation.

The next section will display the various data from trials in a pure KNO_3 melt. Substrate preparation, apparatus and fabrication procedures were identical to those described in the previous section pertaining to $AgNO_3$ guides.

4.8.1 KNO_3 slab data, for varying exchange times

(I) Effective Index Measurements

All exchanges were performed at 400°C with little deviation from this setpoint value, as verified by visible thermocouple readings. (Stability: ± 0.5°C). All measurements were made with flint glass prism, α = 49.9, n_p = 1.785.

(TE polarization)

Table 4.6

(1) 2 hour exchange

MODE	ANGLE OF INCIDENCE (°)	N_{eff}
1	7.8099	1.5205
2	7.4319	1.5162

(2) 4 hour exchange

Mode	Angle of Incidence (°)	N_{eff}
1	15.39722	1.521488
2	15.06805	1.518549
3	14.863889	1.516718452

(3) 8 hour exchange

Mode	Angle of Incidence (°)	N_{eff}
1	15.6375	1.523621
2	15.36805	1.5212285
3	15.16588	1.5194073
4	15.02500	1.5181643

(4) 18 hour exchange

Mode	Angle of Incidence (°)	N_{eff}
1	15.7027783	1.5241992
2	15.51250033	1.5225127
3	15.36666633	1.52121613
4	15.2166633	1.519878697
5	15.09722333	1.518811061
6	15.0125033	1.518052319

(5) 24 hour exchange

Mode	Angle of Incidence (°)	N_{eff}
1	15.7402778	1.524531
2	15.5819445	1.5231289
3	15.45	1.52195749
4	15.3291666	1.52088393
5	15.2055563	1.5197813
6	15.1166733	1.51898507
7	15.03333	1.5182389

The M-line patterns for various KNO_3 exchanges are presented in Fig.4.16 (a) - (d). The TE and TM polarizations are much more apparent for these guides compared to their $AgNO_3$ counterparts. The mode spectrum is ordered M = 0,1,2... from left to right.

(6) 66 hour exchange

Mode	Angle of Incidence (°)	N_{eff}
1	15.8250001	1.5252792
2	15.711112	1.5242729
3	15.6027866	1.52331372
4	15.5089446	1.5224634
5	15.4180001	1.52167295
6	15.316666	1.52077075
7	15.226366	1.519965378
8	15.1666	1.51943286

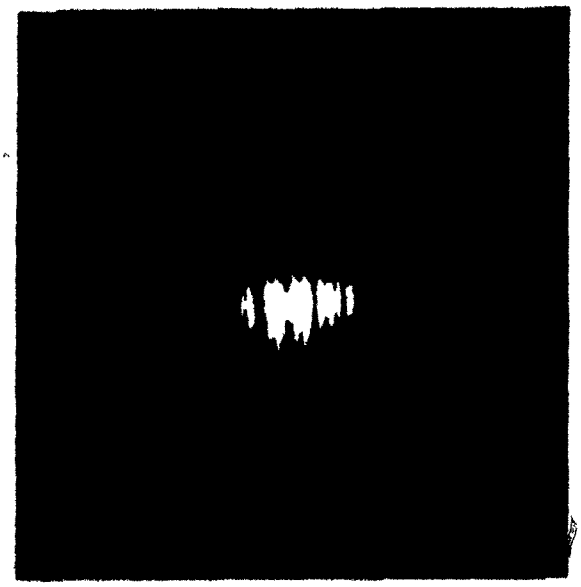

(a) 18 hours, 400 °C

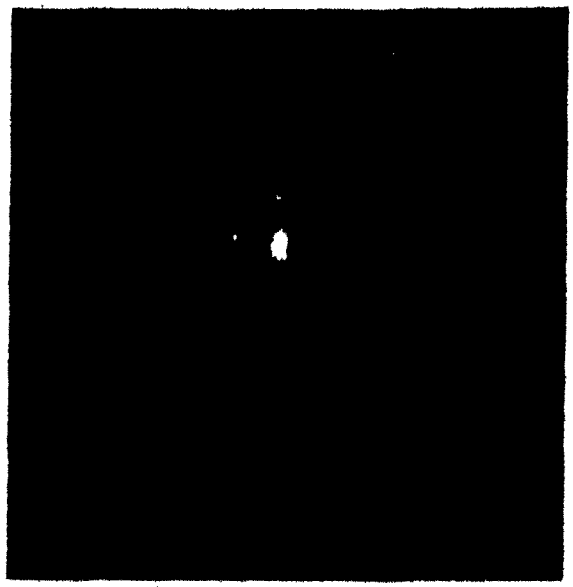

(b) 24 hours , 400 °C

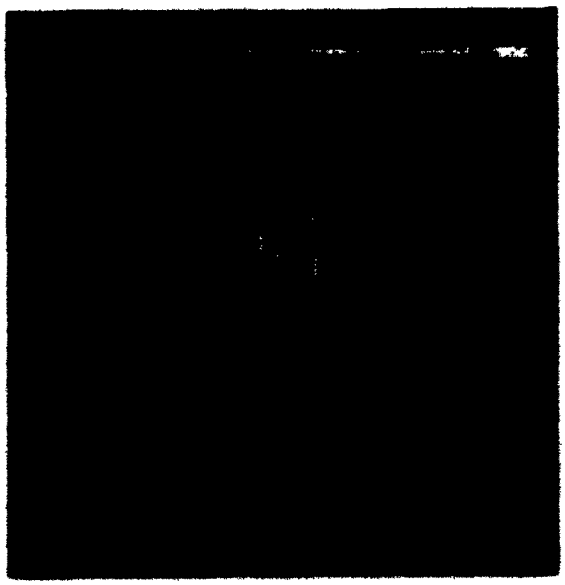

(c) 8 hours , 425 C

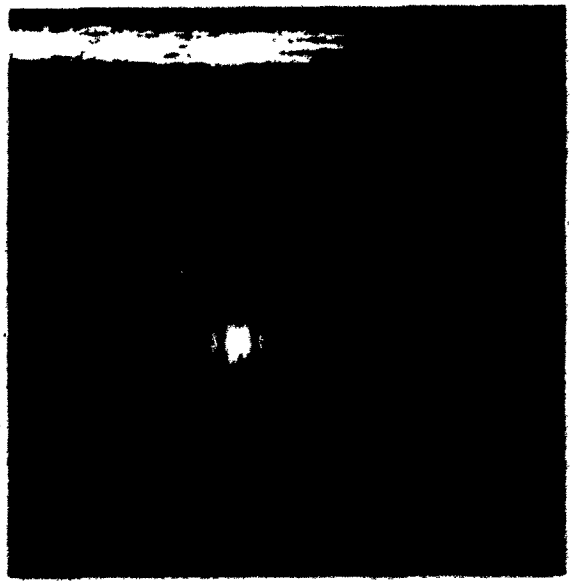

(d) 8 hours , 450 °C

Figure 4.16 Selected KNO_3 m-line Photos

4.8.2 Refractive index profiles

Since the computer program, which generates these refractive index profiles, is sensitive to the N_{eff} values used as the input data, precise measurements are required. The M-lines structures of KNO_3 guides are much denser than those of their $AgNO_3$ counterparts. This results in difficult angular measurement, and hence the accuracy of the KNO_3 profiles presented in Fig.4.18 is slightly reduced when compared to that of the $AgNO_3$ profiles. As the diffusion or exchange time increases, the guide depth increases, but the surface index remains relatively constant.

As in section 4.5, a comparison between the value of the surface refractive index obtained by the WKB integral method and by the refractive index profile is included below:

Trial	WKB Integral	Refractive Index Profile
4 hr, 400°C	1.525	1.5240
8 hr, 400°C	1.5252	1.5260
18 hr, 400°C	1.5251	1.5260
24 hr, 400°C	1.5252	1.5270

Table 4.7 Comparison of surface refractive indicies for a KNO_3 melt.

Surface Index Approximation
(melt temp. for all trials: 400 C)

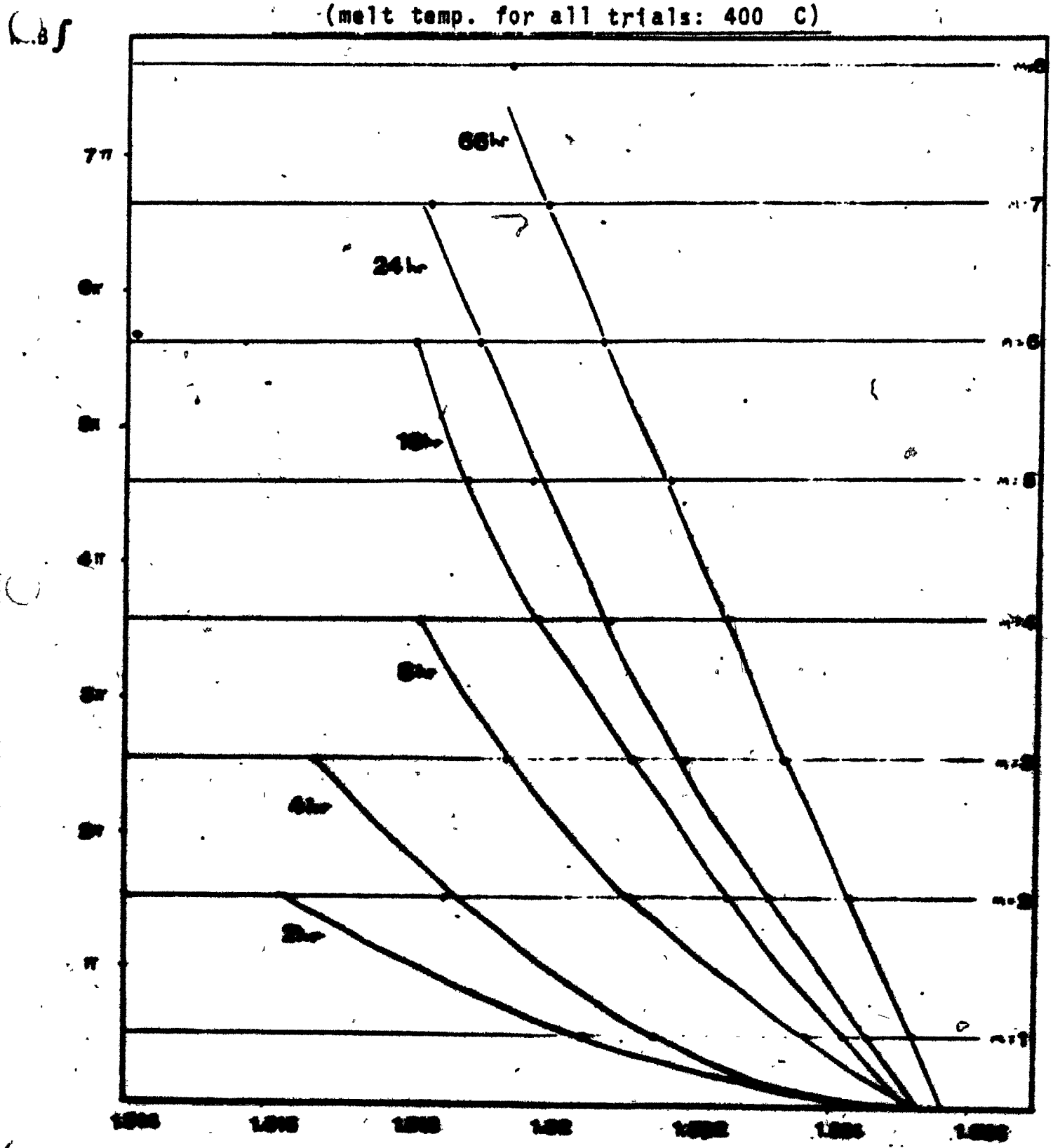

Figure 4.17

KNO_3 Profiles as a Function of Exchange Time
(exchange temp: 400 °C)

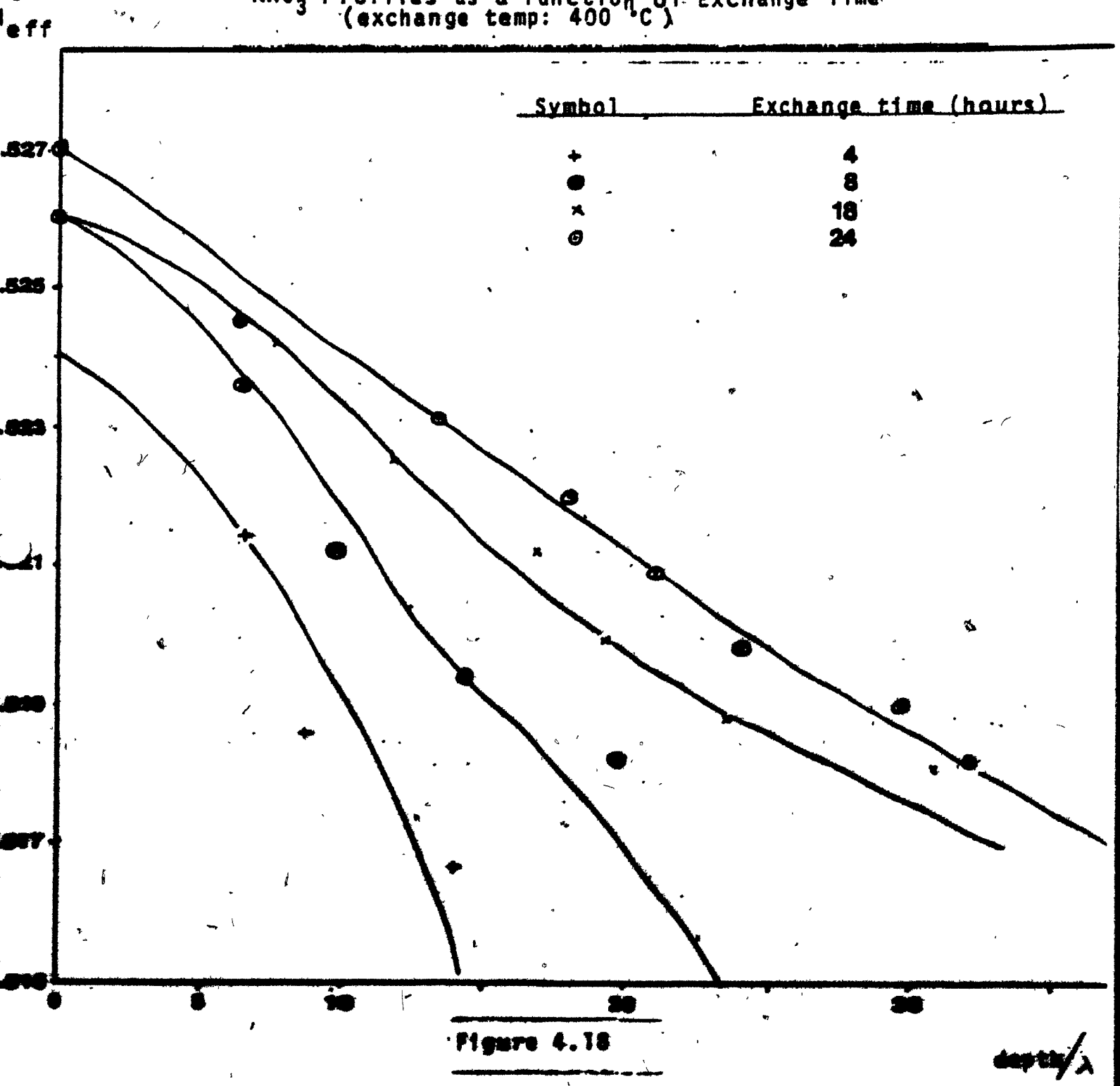

Figure 4.18

Once again we can note that the discrepancy in the measured values is small, averaging about 0.0010. Note also that the surface refractive index value remains relatively constant, and is practically time independent.

4.9 KNO_3 Slab Data for Varying Temperature Conditions

4.9.1. Effective Index Measurement - Table 4.8

All exchanges were performed for a diffusion time of 8 hours at various setpoint values. Measurements were made with a double-edged flint glass prism: $n_p = 1.785$

$\alpha = 49.9$

(I) 375°C

Mode	Angle of Incidence (°)	N_{eff}
1	15.80273	1.5250
2	15.30944	1.5212
3	15.08611	1.5187

(II) 425°C

Mode	Angle of Incidence (°)	N_{eff}
1	15.9375	1.5262711
2	15.70833	1.5242483
3	15.5	1.5224018
4	15.31528	1.5207584
5	15.15695	1.5193452

(III) 450°C

Mode	Angle of Incidence (°)	N_{eff}
1	15.81665	1.5252055
2	15.6972	1.5241498
3	15.563867	1.5229686
4	15.4389	1.5218588
5	15.3472	1.5210428
6	15.2473	1.5201513
7	15.1472	1.5192581

4.9.2 Refractive index profiles (temperature variation)

Since the melt temperature has a direct affect on the speed of the exchange process, we expect an increase in guide depth

Surface Index Approximation
(melt time for all trials: 8 hrs.)

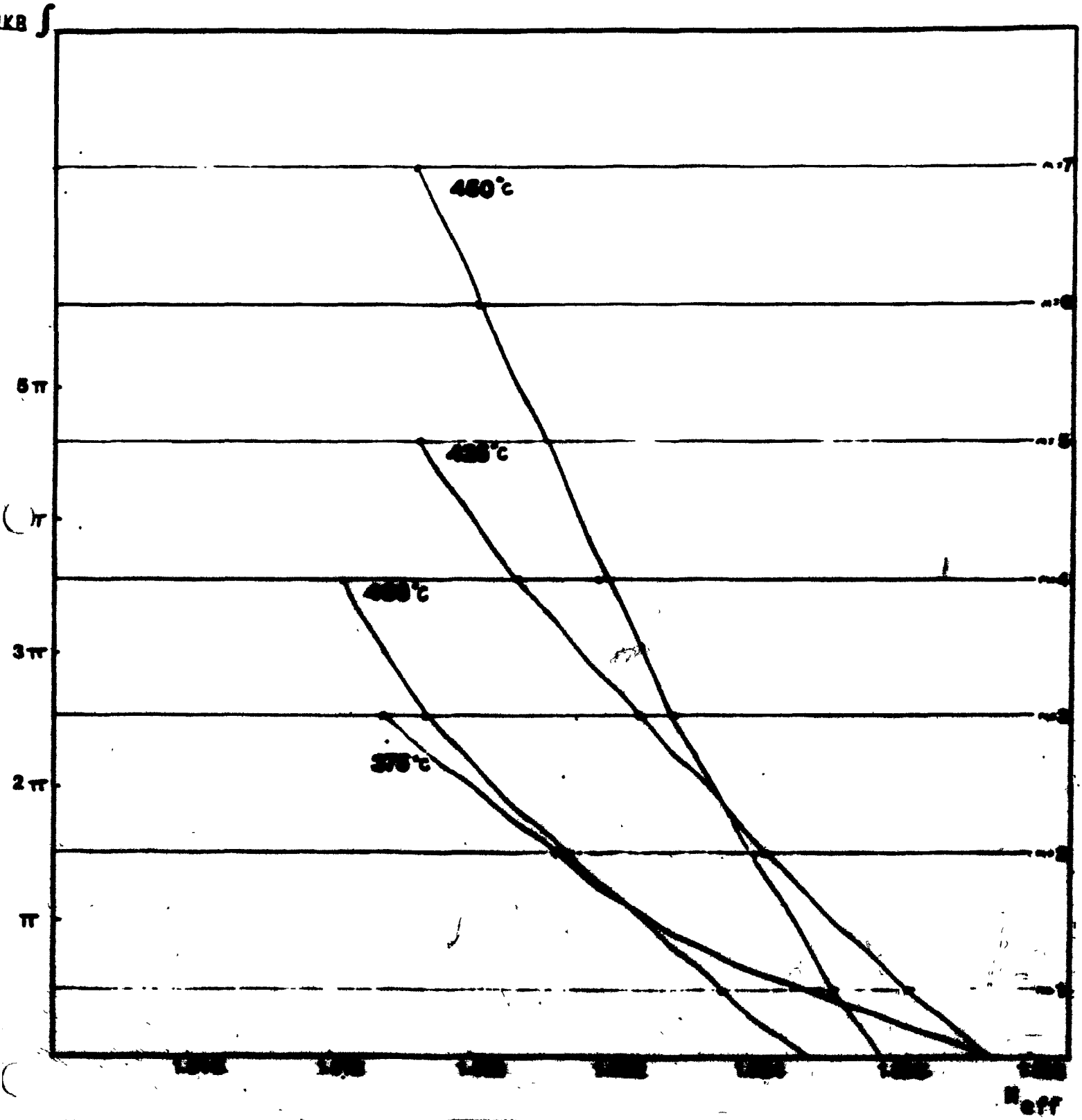

Figure 4.19

KNO_3 Profiles at Various Temperatures.
(exchange time: 8 hours)

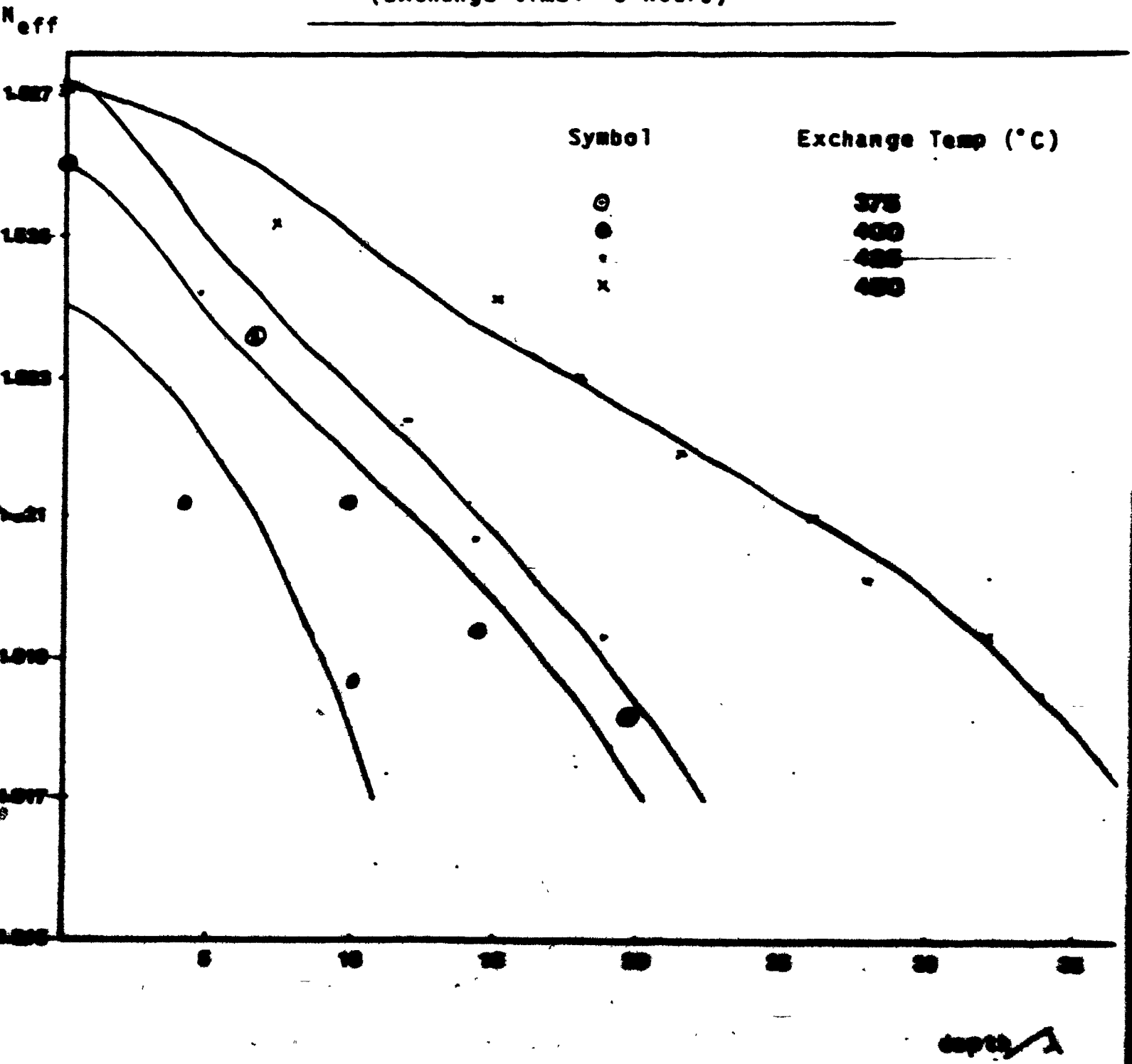

Figure 4.20

for a corresponding increase in temperature (time held constant). These expectations are confirmed by the profiles in Fig. 4.20. A fluctuation in the surface index is also apparent and the profiles are consistent with the trend of increasing surface index for increasing temperature.

Once again, in the following table we compare the estimation of the surface refractive index by the WKB integral method with the results from the refractive index profile using the Heidrich & White procedure.

Table 4.8

Trial	WKB Integral	Refractive Index Profile
8 hr, 375°C	1.5275	1.5240
8 hr, 400°C	1.5248	1.5260
8 hr, 425°C	1.5275	1.5272
8 hr, 450°C	1.5259	1.5271

4.10 Characterization of KNO_3 Ion-Exchanged Slab Waveguides

In an effort to characterize slab waveguides formed by exchange in molten KNO_3, some additional trials were carried out at various settings of time and temperature. This is a worthwhile endea-

ver, since it is desirable to know what depth can be attained in a slab or channel guide following an exchange at any given time or temperature.

Two extra trials were performed at 375°C; one for 18 hours, the other for 24 hours, and two exchanges were also made at 425°C; one for 4 hours, and the other for 24 hours. Including these additional trials, there are 3 guides at 375°C , 4 at 400°C, and 3 at 425°C, yielding sufficient data to investigate a characterization procedure.

In the quest of a unifying equation involving the variables of time and temperature, we follow the steps taken by Stewart et al (9). The first step entails plotting the depth of the slab guide versus the square root of the exchange time. Since ion-exchange is basically a diffusion process, the waveguide depth should vary linearly with the square root of exchange time.

The waveguide depth can be well-estimated by locating the set of measured effective index values on the universal dispersion curve (Fig. 4.25), and noting at what value of V that these indices line up on. By knowing the wavelength of the incident source, the bulk and surface indices, the depth in microns can be found.

Another possibility is to utilize the refractive index profile for that specific guide. By locating where the index falls

off to 1/e of its surface value and finding that corresponding depth, a reasonable estimate of the waveguide depth results.

By employing these two methods, the depth of each waveguide considered in this study was located. A linear plot of d vs $\sqrt{t}$ for temperatures of 375, 400 and 425°C is included in Fig. 4.21. Note that the slope increases for increasing values of temperature.

The next consideration in the characterization involves finding the diffusion coefficient:

$$D = d^2/t \qquad (4.5)$$

This is merely the slope of the lines in Fig. 4.21, and a different coefficient can be found for each temperature. Since D varies exponentially with temperature (9);

$$D = C_3 \exp(-C_2/T) \qquad (4.6)$$

by taking the log of D and plotting each value with respect to inverse temperature, we expect a linear relationship. This plot is included in Fig. 4.22, and is shown to have a negative slope. The value of the slope is C_2 in equation 4.6. The coefficient C_3 can be [illegible] the line crosses the ordinate in Fig. 4.22.

In estimating the waveguide depths for the plots in Fig. 4.2 1 , the values of n_s at various temperatures were required. At 375 °C, neither the WKB plot nor the refractive index curves yielded reliable results (see table 4.8). Consequently, this value was chosen as 1.5250, between the lower bound of 1.5240 (from the refractive index plot) and the upper bound of 1.5275 (WKB result). The average of both the WKB and refractive index results is 1.52575, but 1.5250 was selected because it must be less than the result n_s = 1.5252 at 400 °C (see table 4.7, WKB column).

At 400 °C, 8 hours, the result n_s = 1.5252 is a reliable value: Fig. 4.17 shows many plots converging to this number.

For 425 °C, both the refractive index results are in reasonable agreement: n_s = 1.52735 ave. Given that the n_s figures at 375 & 400 °C do not differ greatly, it was felt that n_s = 1.52735 was too large, so n_s = 1.5255 was selected for T = 425 °C.

Due to the lack of data at 375 & 425 °C, the plots in Fig 4.21 for these temperatures are not as accurate as the curve presented for 400 °C.

Dependance of Guide Depth on Diffusion Time

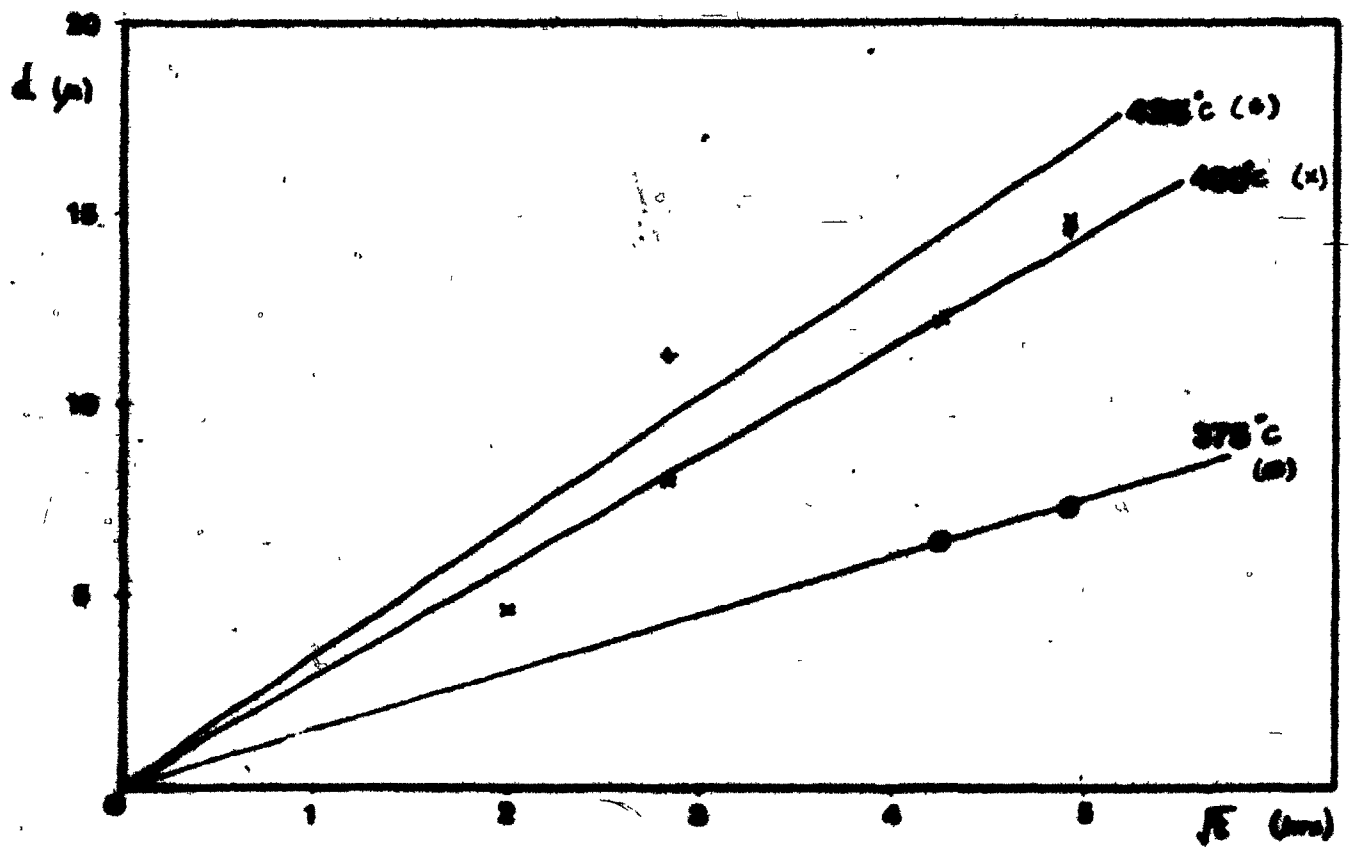

Figure 4.21

Log (diffusion Coefficient) vs Inverse Temperature

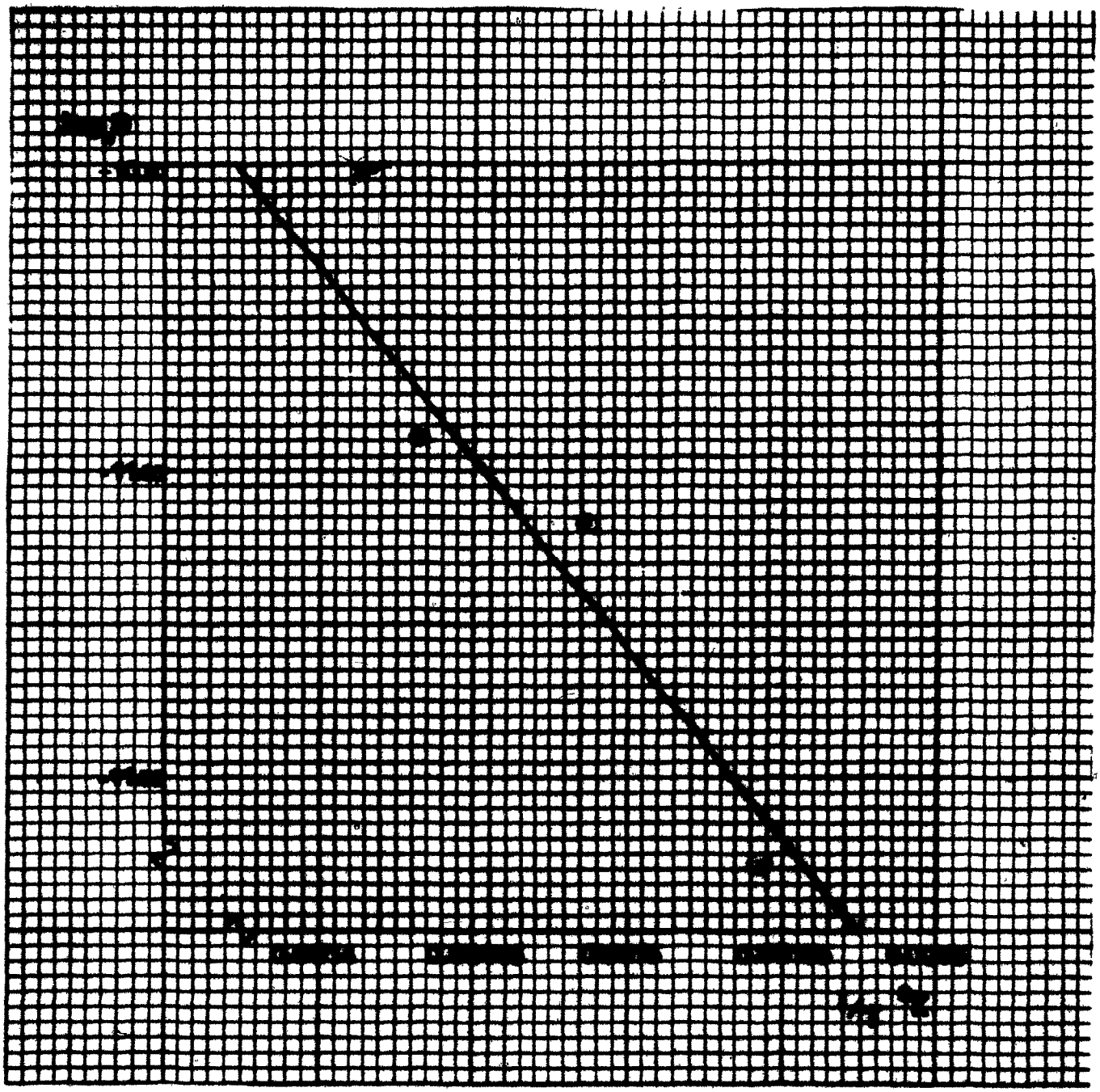

Figure 4.22

Additional KNO_3 Refractive Index Profiles

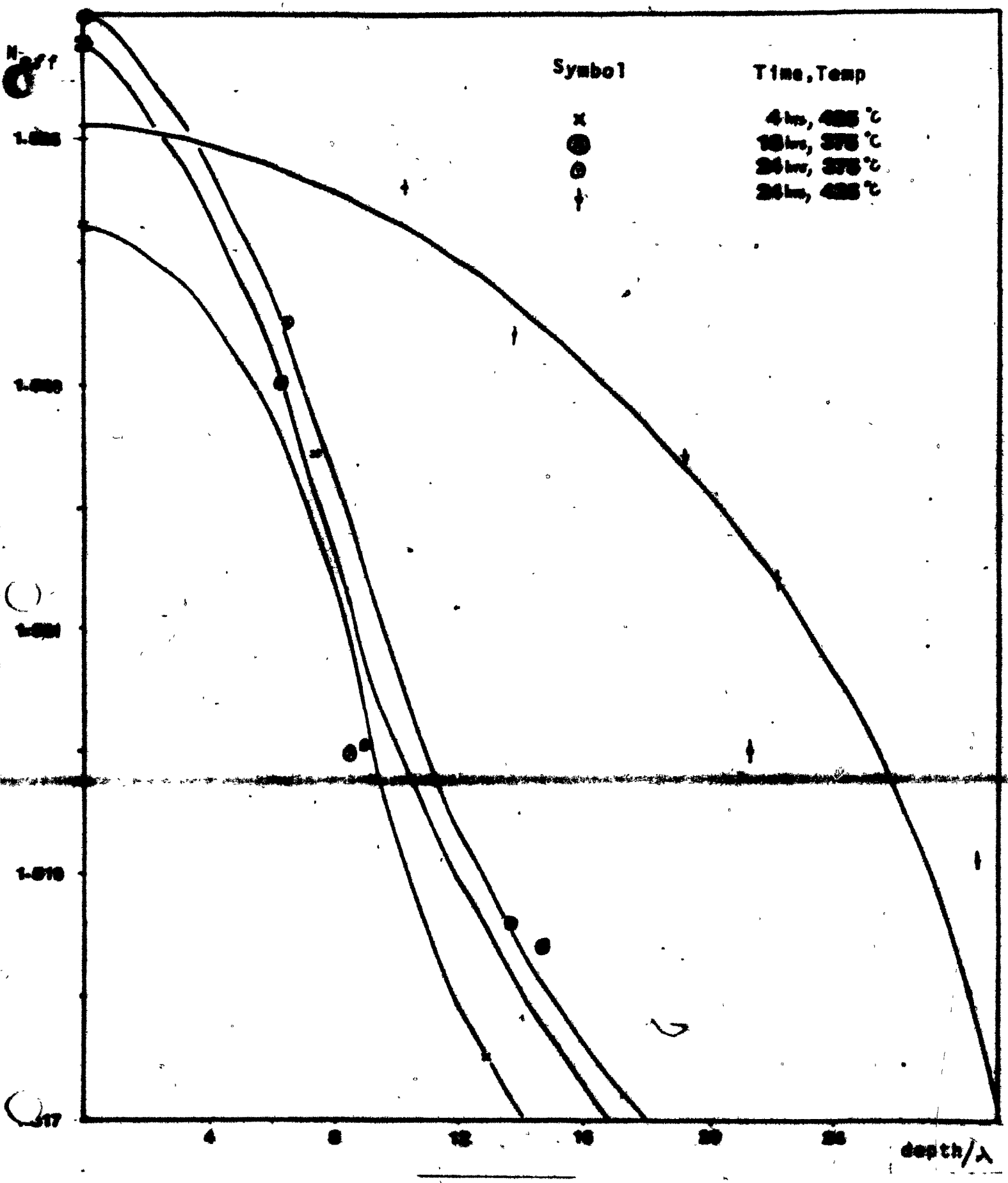

Figure 4.23

As outlined in Stewart et al (9), the unifying equation adopts the following form:

$$d = C_1 \sqrt{t} \exp(-C_2/2T) \qquad (4.7)$$

Since we know C_2 and both the time and temperature values, we can find C_1. By following the steps outlined above, we find that the KNO_3 guides exchanged under our specific laboratory conditions can be characterized by the following two equations:

$$\text{(I)} \quad D_e = 4.467 \times 10^{-11} \exp(-1.4276 \times 10^4/T) \qquad (4.8)$$

$$\text{(II)} \quad d = 1.197 \times 10^{-1} \sqrt{t} \exp(-1.4276 \times 10^4/2T) \qquad (4.9)$$

4.11 A Comparison between Experimental and Theoretical Dispersion Curves

This section is devoted to comparing the previously derived theoretical curves in Chapter 3 with the experimentally measured effective mode indices. As outlined in the previous chapter, normalized quantities must be employed (refer to equations 3.40 - 3.42), with the dispersion curves for inhomogeneous guides normalized to the surface index (n_s).

In order to locate the measured mode indices on the inhomogeneous dispersion curves, they must be normalized according to equations 3.40 - 3.41. After verifying with the refractive index profiles plotted with the H & W method, a typical value for n_s was selected for normalization with respect to both $AgNO_3$ and KNO_3 asymmetry.

The set of curves in Fig. 4.24 and 4.25 exhibit agreement between theory and experiment for $AgNO_3$ and KNO_3 exchanges respectively. A Gaussian refractive index profile was chosen in deriving the dispersion curves for both asymmetries. The number of modes predicted by theory and experiment for a certain normalized depth (frequency) is in reasonable agreement.

The last set of curves in Fig. 4.26 consists of dispersion curves generated by the WKB and step approximation methods outlined in Chapter 3. This figure is essentially the same as the comparison of WKB and step curves shown in the previous chapter except that the former are based on the actual experimental refractive index profile for a guide exchanged in a KNO_3 for 8 hours at 450°C while the latter are for an ideal Gaussian refractive index profile.

4.12 Comparison of Results for $AgNO_3$ Trials with those of Stewart et al (3)

(a) Guide depth:

Comparison of Experimental & Theoretical
Dispersion Curves. ($AgNO_3$)

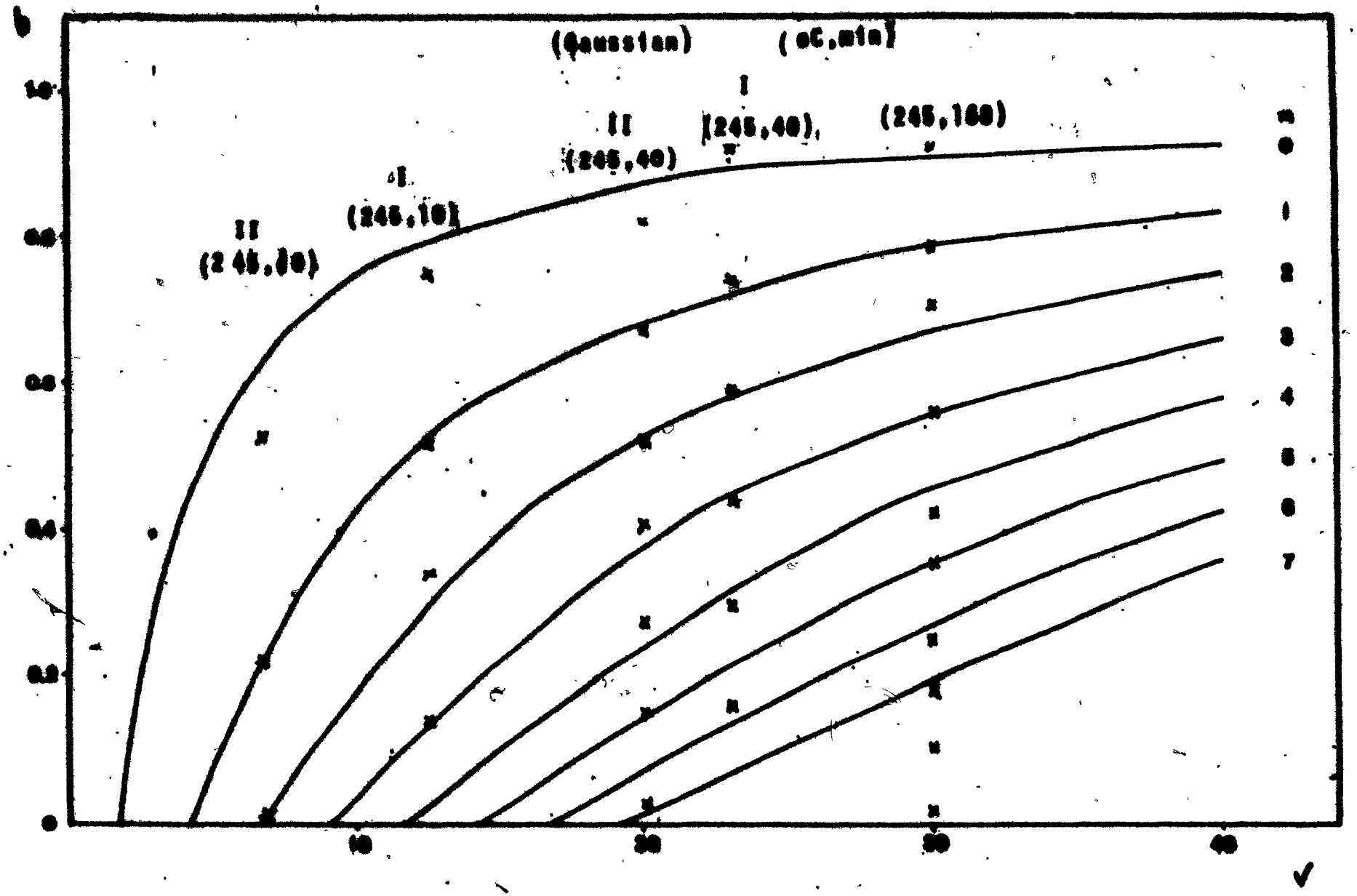

Figure 4.24.

Comparison of Experimental & Theoretical Dispersion Curves
(ZnO_3 , Gaussian profile)

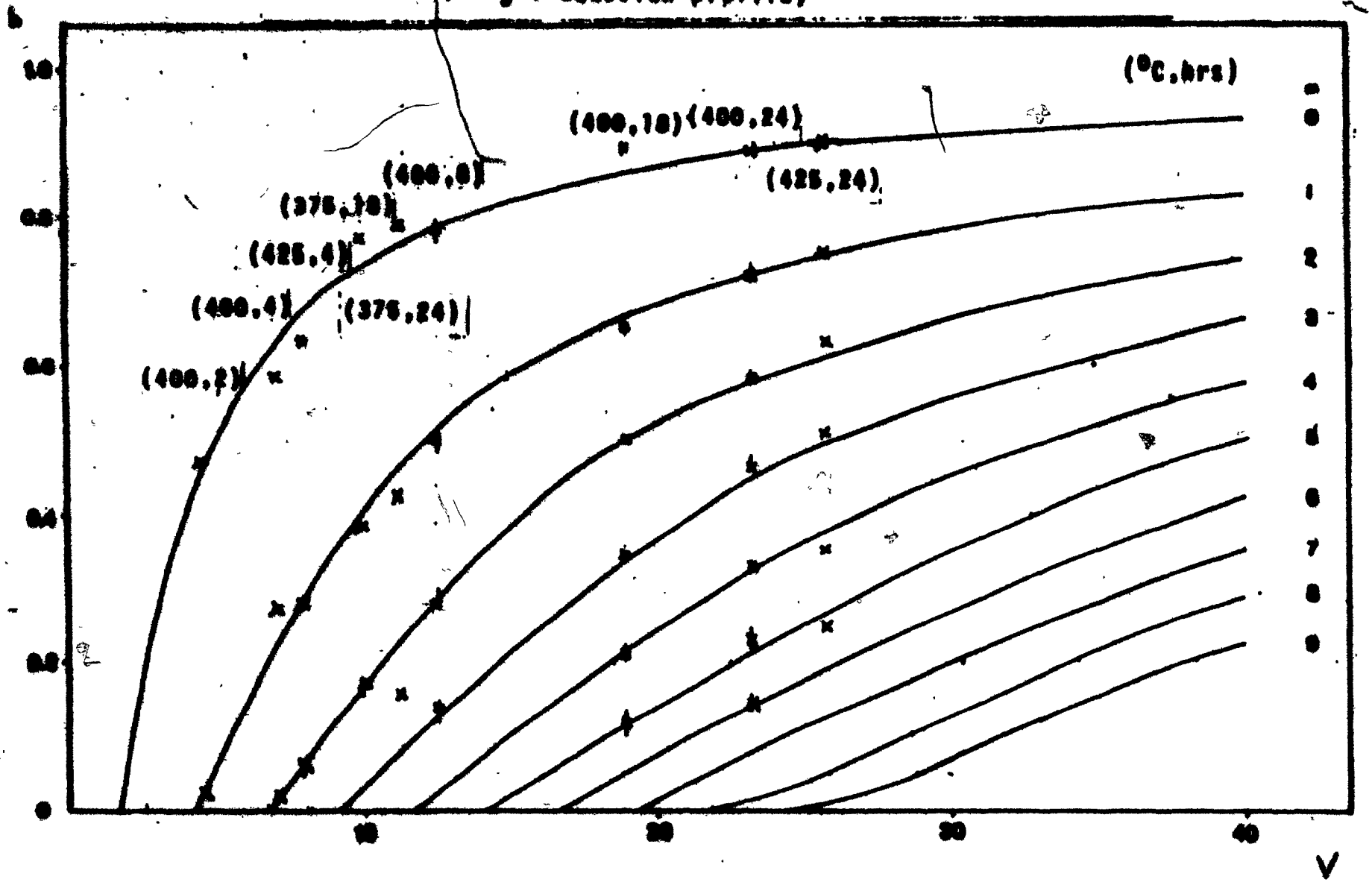

Figure 4.25

Comparison of Dispersion curves - step,WKB

Experimental Profile: 8 hours, 450 °C

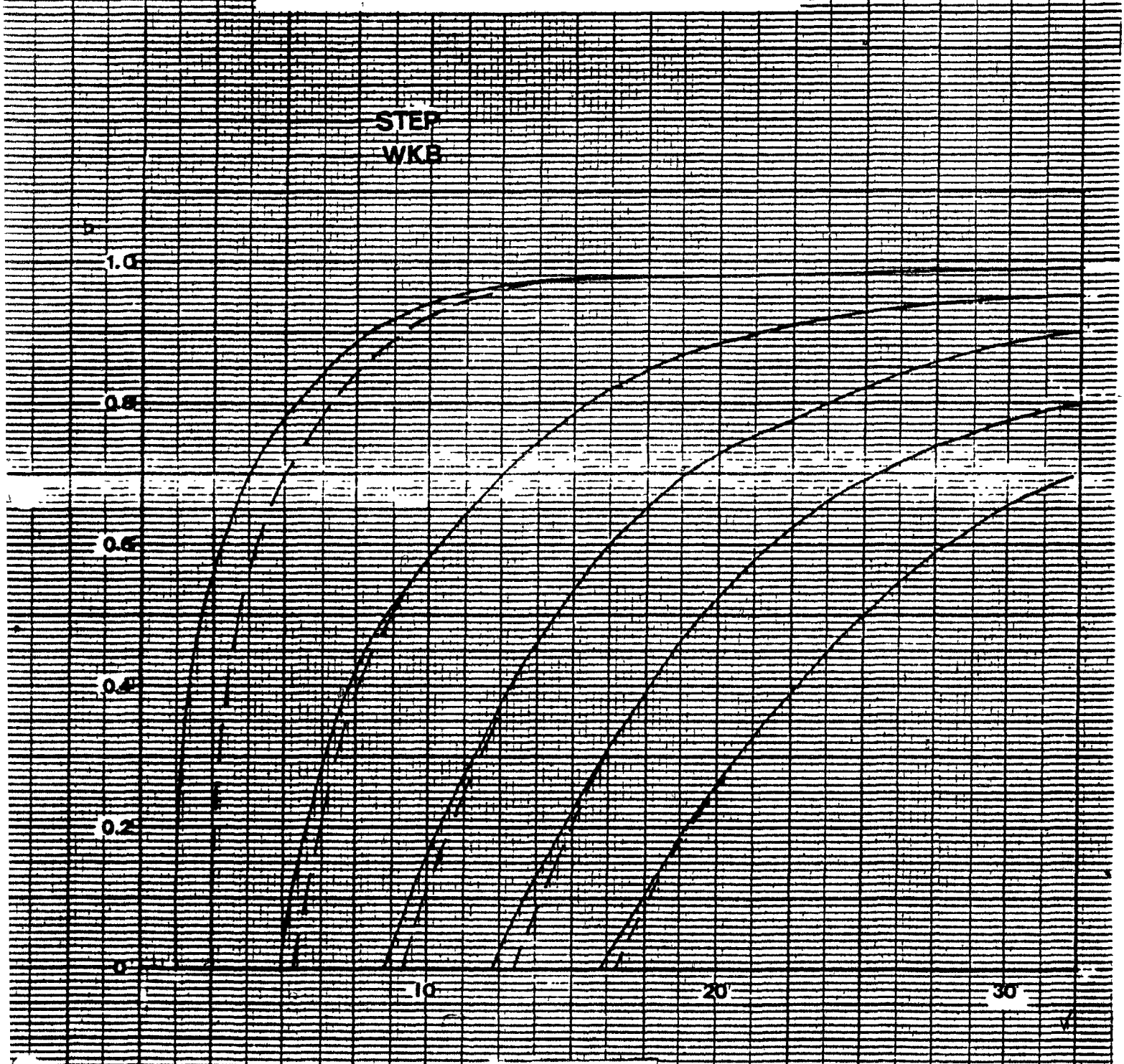

Figure 4.26

Table 4.9 compares the guide depths obtained from the refractive index profiles with the same quantity obtained from Stewart's expression:

$$d = 1.19 \times 10^4 \, t^{\frac{1}{2}} \exp(-1.02 \times 10^4/2T) \quad (\mu m) \qquad (4.5)$$

Trial (T = 245 °C)

		10 min.	40 min.	90 min.	160 min.	
Method	Index Profile	2.59	5.54	8.23	8.31	(μ)
	Stewart	1.99	3.98	5.98	7.97	(μ)

Table 4.9 Guide Depth Comparison
The guide depths were obtained from Figs. 4.12 a & b, where the curves cross the boundary $N_{eff} = 1.517$

(b) Profile:

Figure 4.27 compares two sets of effective mode indices for the following experimental conditions:

Exchange time: 40 minutes

Exchange temp: 245°C

with the curve $F(n(x), n_e)$ generated by setting n(x) to a Gaussian profile and using experimental mode indices n_e for a trial at 300°C for 36 min. (see Stewart et al (9)).

The agreement is excellent in one case and quite good in the other.

Comparison of $AgNO_3$ Data with Stewart's Data

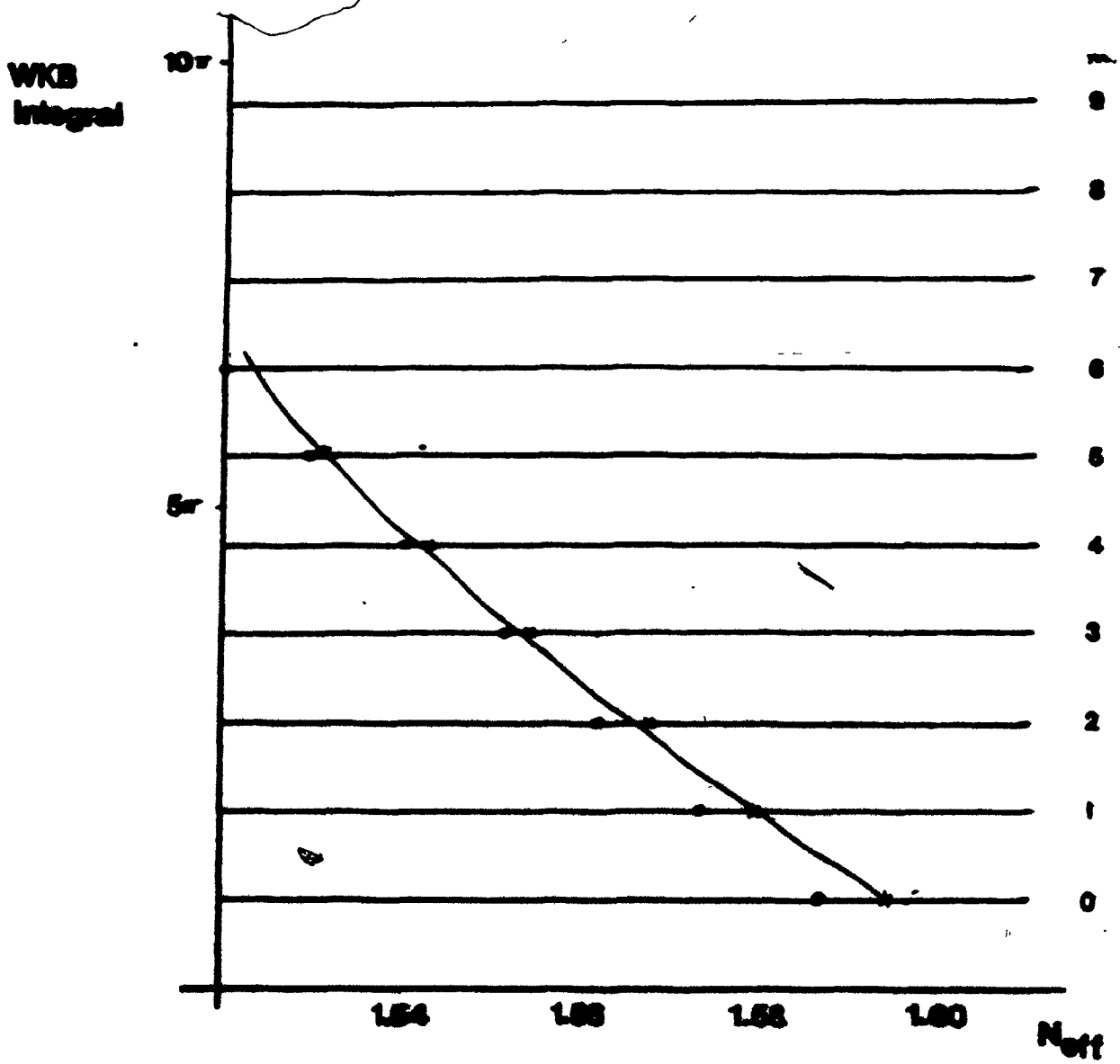

x = trial I 40 min. 245 C $AgNO_3$
• = trial II 40 min. 245 C $AgNO_3$
—— = Gaussian fit as per Stewart et al. (36 min. 300 C)

Figure 4.27

CHAPTER V

CHANNEL WAVEGUIDES BY ION EXCHANGE

Slab waveguides, discussed in the previous chapter, provide no confinement of light in the plane of the guide, (say the y-z plane) except in the x direction alone. Channel guides provide an additional confinement in the y direction as well as the x direction and in this manner, high power signals can be confined and fed to devices for signal processing.

In this chapter, the theory of channel guides and mode dispersion is quoted by two separate methods and the fabrication procedure is outlined, with experimental results.

Many types of crossectional shapes of channel guides are realizable, and although the experimental study is concerned with the simple embedded channel structure, the various configurations are listed in Fig. 5.1.

5.1 Marcatili's method of analysis

In Marcatili's (2) technique of analysing channel guides, the channel is immersed in several dielectrics. (Fig.5.2)

(a) Embedded Channel

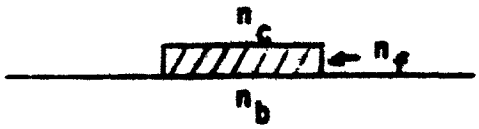

(b) Raised Channel

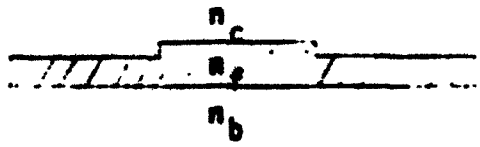

(c) Ridge Guide

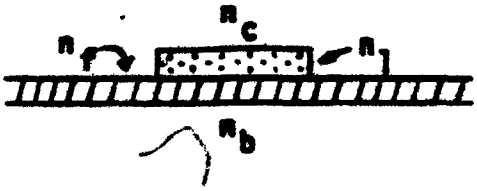

(d) Strip Loaded Guide

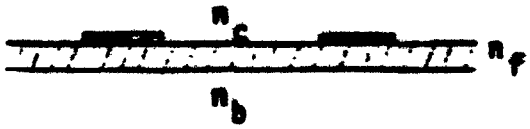

(e) Metal Clad Guide

Figure 5.1 Cross Sections of Various Channel Guides

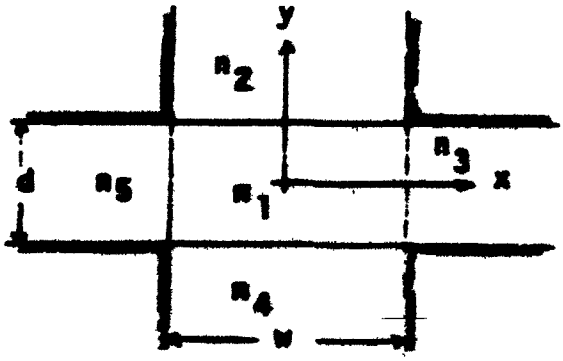

Figure 5.2 Channel Guide Immersed in Several Dielectrics

He assumed five separate refractive indices, for the channel and the four surrounding media. The criterion for guidance is $n_1 > n_{2,3,4,5}$, n_1 being the channel index.

Marcatili considered field distributions not unlike those of a rectangular, hollow metal waveguide. In the core region, the E^y_{pq}, E^x_{pq} modes vary sinusoidally in both the x and y directions. In his nomenclature, p and q indicate the number of modes in the lateral coordinate and depth coordinate respectively.

In Marcatili's method, the fields in the shaded areas of Fig. 5.2 are ignored for simplification. It is also assumed that the field decays exponentially in regions 2,3,4 and 5, with most of the power confined in region 1. Field matching at the four boundaries of the core region can be performed, assuming simple field distributions. Field components in region 1 vary sinusoidally in the x and y directions, while in regions 2 & 4, the fields vary sinusoidally in x and exponentially along y. Lastly, the field components in regions 3 & 5 vary sinusoidally in y and exponentially in x. Employing these assumptions, eigenvalue or transcendental equations can be derived by matching the field solution at the various dielectric interfaces.

We define k_z as the axial propagation constant while $k_{x_{1,2,4}}$ are propagation constants in the x direction, in media 1, 2 and 4 respectively, that are assumed identical and independent of y. We also define propagation constants in the y direction as $k_{y_{1,3,5}}$ in regions 1,3 & 5 respectively, assumed identical and independent of x.

E^x_{pq} Modes

Employing the notation v = 1,2,3,4,5 for identification of the five dielectric media, the transverse propagation constants are denoted k_{x_v} and k_{y_v}. The following relations hold:

$$k_v = k_o n_v \tag{5.1}$$

$$k_z = (k_1^2 - k_x^2 - k_y^2)^{1/2} \tag{5.2}$$

and by field matching at the boundaries between regions 1, 2 and 4;

$$k_x = k_{x_1} = k_{x_2} = k_{x_4} \tag{5.3}$$

and similarly by matching in regions 1, 3 and 5;

$$k_y = k_{y_1} = k_{y_3} = k_{y_5} \tag{5.4}$$

According to Marcatili, these transverse propagation constants are solutions of the following transcendental equations:

$$k_x w = pv - \tan^{-1}\frac{n_3^2}{n_1^2} k_x \xi_3 - \tan^{-1}\frac{n_5^2}{n_1^2} k_x \xi_5 \tag{5.5}$$

$$k_y d = qv - \tan^{-1} k_y \eta_2 - \tan^{-1} k_y \eta_4 \tag{5.6}$$

where w is the channel width, d the channel depth and

$$\xi_{\substack{3\\5}} = \frac{1}{(k_1^2 - k_{\substack{3\\5}}^2 - k_x^2)^{1/2}} \tag{5.7}$$

$$\eta_{\substack{2\\4}} = \frac{1}{(k_1^2 - k_{\substack{2\\4}}^2 - k_y^2)^{1/2}} \tag{5.8}$$

The constants ξ & η are essentially the penetration depths of the field components in the various media.

E^y_{pq} Modes

The main difference between these modes and the

E^x_{pq} modes is the fact that the transverse field components in this case are E_y and E_x as opposed to E_x and E_y for E^x_{pq} modes.

The transverse propagation constants for these modes are obtained by solving:

$$k_x w = p\pi - \tan^{-1}(k_x \xi_3) - \tan^{-1}(k_x \xi_5) \tag{5.9}$$

$$k_y d = q\pi - \tan^{-1}\left(\frac{n_2^2}{n_1^2} k_y \eta_2\right) - \tan^{-1}\left(\frac{n_4^2}{n_1^2} k_y \eta_4\right) \tag{5.10}$$

By making the approximation that for well-guided modes (far from cutoff), most of the power travels in the core region or medium 1, the transcendental equations 5.5, 5.6, 5.7 and 5.8 can be reduced to closed form. Thus, solution for k_x, ξ and η are possible and upon comparison of these solutions for E^x_{pq} and E^y_{pq} modes, they coincide exactly. This makes us aware that both modes are degenerate.

5.2 Effective Index Method

This method is a simple tool for providing relatively good predictions for the behavior of channel guides. In 1970, Knox & Toulios (39) introduced an effective dielectric

constant serving to couple two slab guides so that they approximate a rectangular waveguide.

In Fig. 5.3 a,b, & c, we see the cross-section of a channel guide and then the two slab guides, which together, approximate the original channel.

The method consists of letting the long dimension of the channel guide approach infinity to obtain a slab guide as in 5.3 (b) and then calculating the propagation constant of this guide. This propagation constant serves as the effective index in slab configuration 5.3(c) provided it is properly normalized. The second slab configuration is obtained by allowing the short dimension of 5.3(a) to approach infinity. Finally, the propagation constant of this second slab is taken to be that of the original channel guide.

Hocker and Burns (25) have used the above method to analyze mode dispersion in embedded channel guides assuming (n_1-n_2) large and (n_1-n_3, n_1-n_4) small as in the case of diffused channel guides. Using normalized, universal dispersion charts, they applied the effective index method and their results had closer agreement to Goell's (3) circular harmonic calculations than those of Marcatili near the cutoff region. The effective index method for channel guides

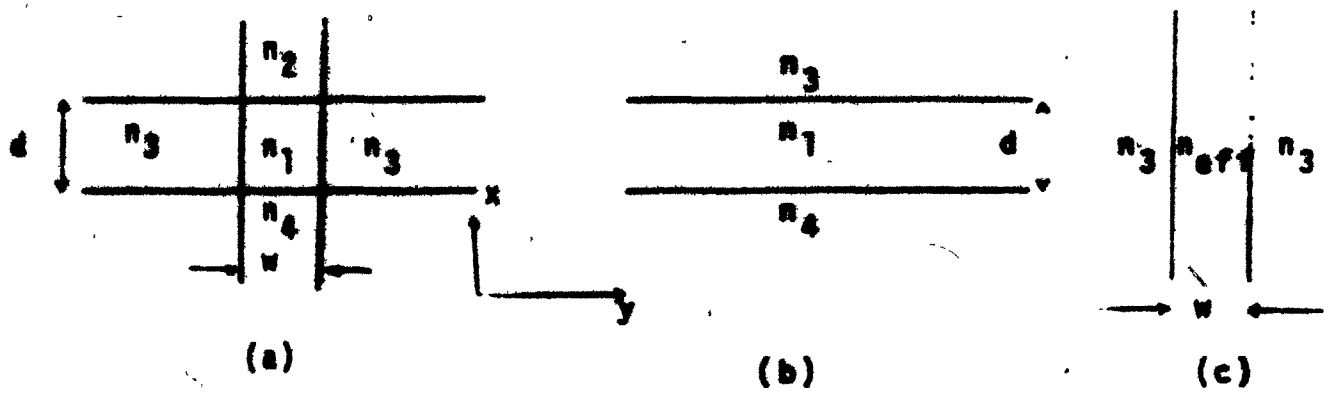

Figure 5.3 Effective Index Methodology
(Homogeneous Case)

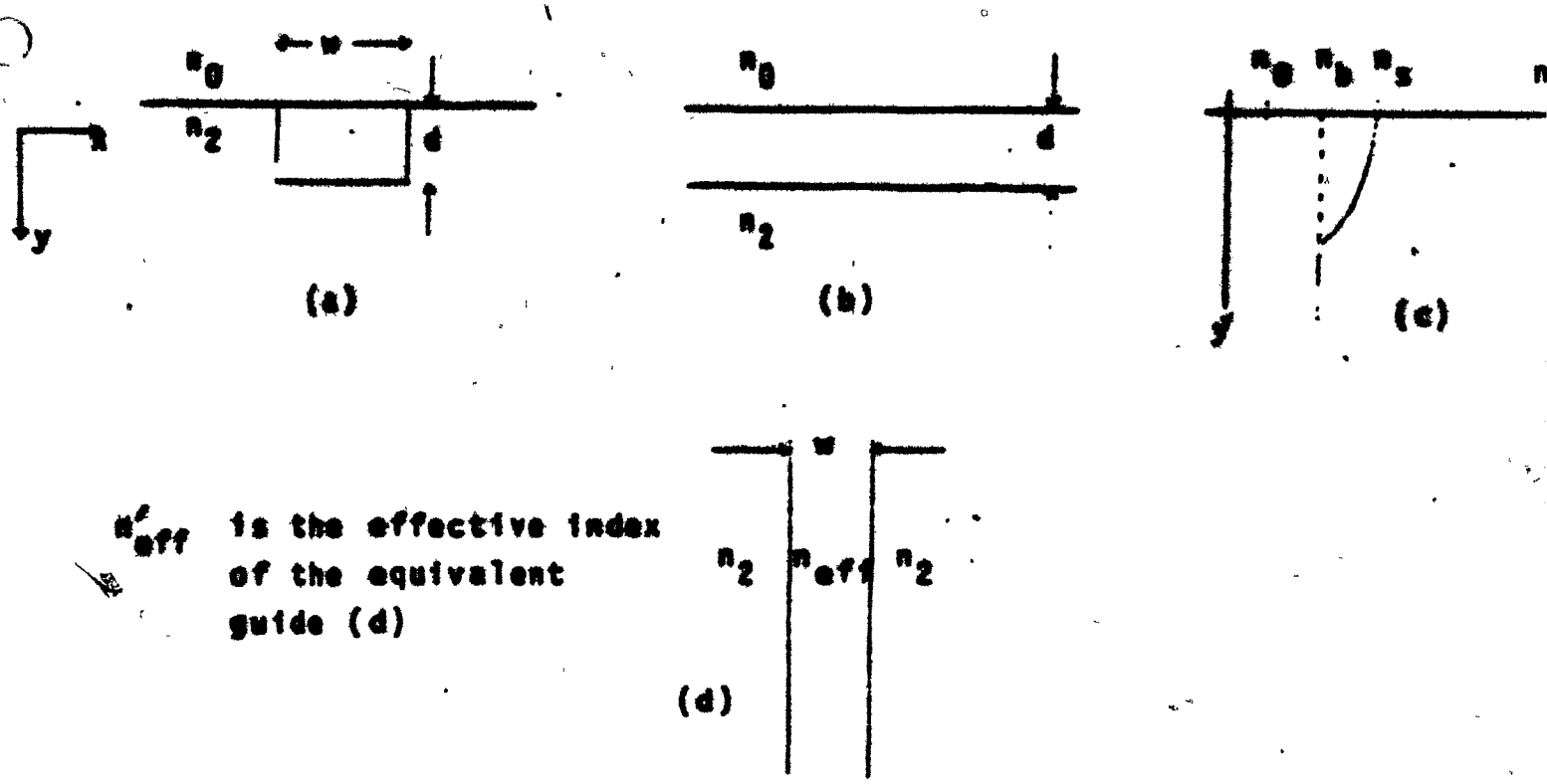

n'_{eff} is the effective index of the equivalent guide (d)

Figure 5.4 Effective Index Methodology
(Inhomogeneous in Y)

with 1-D diffusion (no sideways diffusion) is developed as follows with the aid of Fig. 5.4.

Note that although the index profile is inhomogeneous in y, it is taken to be constant for all x values within the core region. As in the previous case, extend the x direction to infinity to get an equivalent inhomogeneous slab guide and solve

$$\nu \int_{0}^{\alpha t} (n(\alpha) - b)^{1/2}\, d\alpha = (\nu + 1/4)\pi + \tan^{-1}\sqrt{\frac{b+a}{1-b}} \qquad (5.11)$$

(variables described in Appendix B)

$$\nu = k_0 d(n_g^2 - n_2^2)^{1/2} \qquad \nu \text{ integer TE modes}$$

for the required propagation constants. Equation (5.11) may also be used for TM modes (26) provided $(n_g - n_b) \ll 1$, (a good assumption for diffused guides) and the asymmetry measure a, is defined as:

$$a' = n_g^4/n_e^4 \left[(n_b^2 - n_e^2) \,/\, (n_g^2 - n_b^2)\right] . \qquad (5.12)$$

The resulting propagation constants are in turn used as the effective index values for the equivalent slab obtained by letting the y dimension extend to infinity. The propagation

constants of this configuration are easily obtained from the eigenvalue equation for a homogeneous symmetric slab guide

$$v\sqrt{1-b} = \nu\pi + 2\left(\tan^{-1}\sqrt{\frac{b}{1-b}}\right) \qquad \text{(TE modes)}$$

$$v = k_o w\sqrt{n_{eff}^2 - n_2^2} \qquad \nu \text{ integer} \qquad (5.13)$$

and these values are considered to be the propagation constants of the original channel guide.

The theory has been extended by Hocker and Burns (25) for the situation of 2-D diffused channel guides including the effects of lateral diffusion but is not presented herein.

Note that the eigenvalue equation (5.13) can be used for TM modes provided $(n_{eff}-n_2)$ is small. If this is not the case, then we must redefine the effective guide index; (40)

$$b = \left[(N^2 - n_2^2) / (n_{eff}^2 - n_2^2)\right] / (n_{eff}^2/n_2^2 q_o) \qquad (5.14)$$

$$\text{where } N^2 = \left[n_{eff}^2(1-b) + n_2^2 b\right] q_o \qquad (5.15)$$

$$q_o = \frac{N^2}{n_{eff}^2} + \frac{N^2}{n_2^2} - 1 \qquad (5.16)$$

being a reduction factor to keep $0 \leq b \leq 1$.

In keeping with Kogelnik and Ramaswamy (40), the normalized dispersion relation for TM modes in a symmetric slab guide is as follows:

$$v\left[(q_s)^{1/2}\, n_{eff}/n_2\right](1-b)^{1/2} = \nu\pi + 2\tan^{-1}\sqrt{b/(1-b)} \quad (5.17)$$

ν integer

The normalized dispersion curves outlined in Chapter 3 can be employed to characterize propagation in channel guides. According to Hocker and Burns (25), diffused channel waveguides conform to the situation where the index difference between the channel and the cladding is small. Thus, the normalized dispersion curves for TE modes can be used for both the E^x_{pq} and E^y_{pq} modes; with an appropriate change in the assymetry measure a.

It should also be noted that the dispersion curves can be plotted with respect to normalized guide width $v = 2\pi w/\lambda\sqrt{n_1^2 - n_4^2}$ as in (27) or with respect to the normalized guide depth $v = \frac{2\pi d}{\lambda}\sqrt{(n_1^2 - n_4^2)}$ as in reference (25).

In order to gain further insight into propagation in channel waveguides, the dispersion curves for both polarisations of the electric field are plotted in Fig. 5.5 for various modes. The curves are based on Marcatilli's dispersion equations in approximate, closed form composed of a

TE & TM Dispersion Curves for Channel Guides

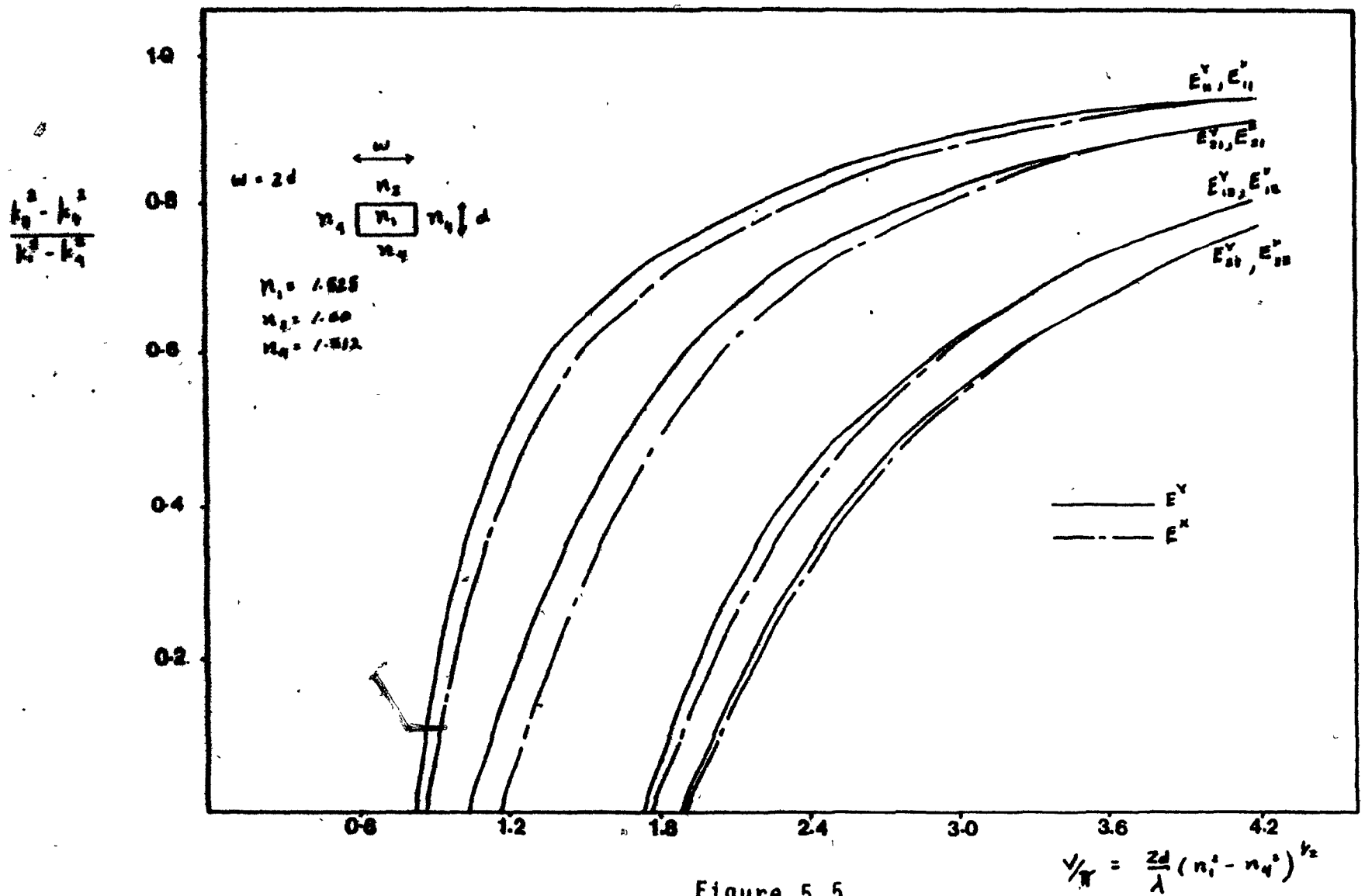

Figure 5.5

homonegenous core (n_1 = 1.525 (KNO_3)) immersed in a homogeneous surround, as shown in Fig. 5.2.

A comparison of dispersion curves, generated by both Marcatili's analysis and the effective index method is included in Fig. 5.6(a) and 5.6(b). Since Marcatili assumes a homogeneous guide for his analysis, the curves plotted from the effective index method employ the homogeneous dispersion equations for depth, as well as width. This is a necessary condition for comparison purposes.

In Fig. 5.6(a), E^y_{pq} modes are compared, using equations 5.9, 5.10 for Marcatili's analysis, and equation 5.13 as well as the asymmetric form of 5.13:

$$v\sqrt{1-b} = v\pi + \tan^{-1}\sqrt{\frac{b}{1-b}} + \tan^{-1}\sqrt{\frac{b+a}{1-b}} \qquad (5.13(b))$$

$$v \text{ integer}$$

for the effective index method. A comparison of E^x_{pq} modes is illustrated in Fig. 5.6(b) employing equations 5.5 and 5.6 for Marcatili's analysis, and equations 5.13(a) and 5.13(b) with the proper asymmetry measure for the effective index method.

Comparison of Dispersion Curves by
the Effective Index Method & Marcatili's Method.

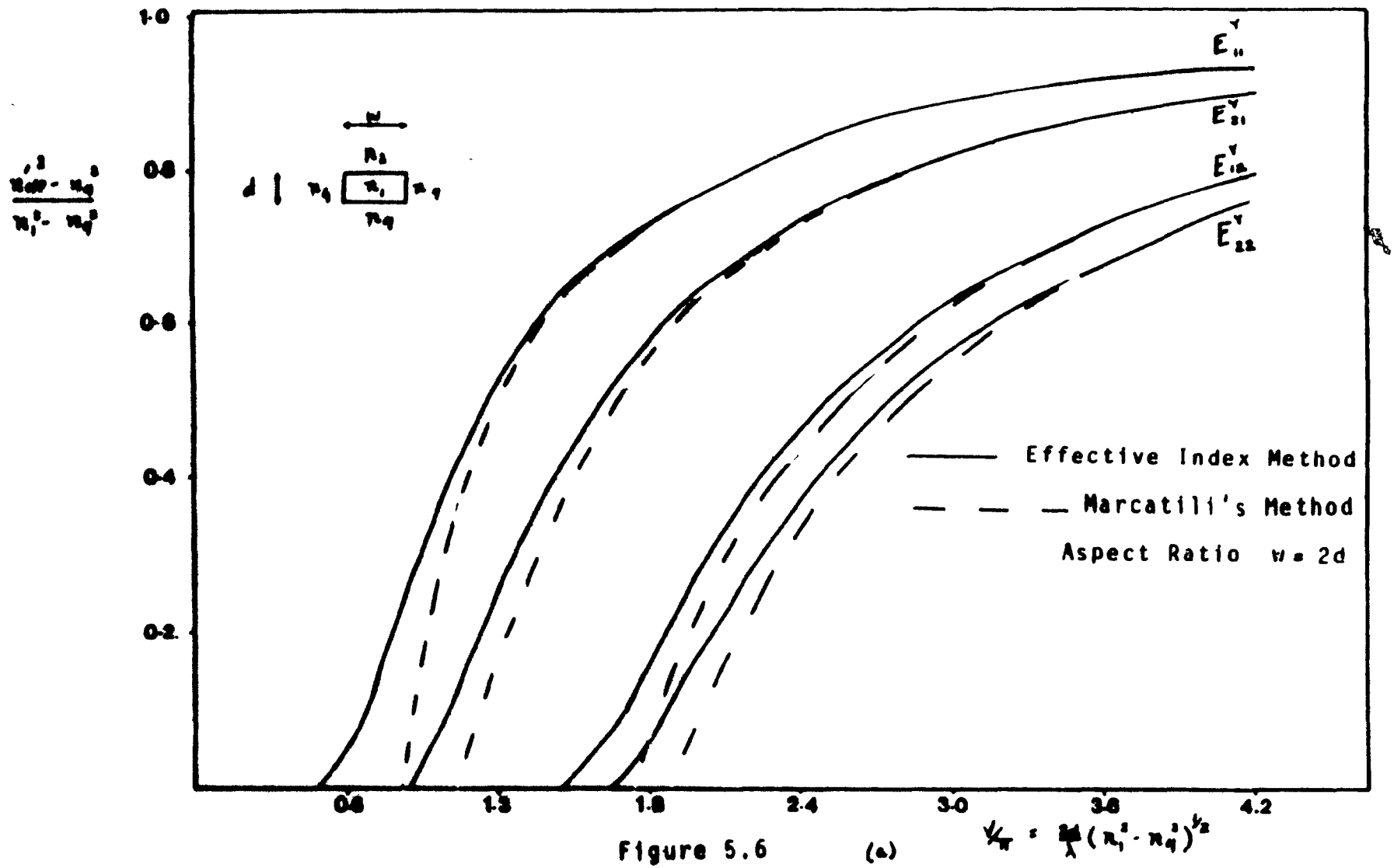

Figure 5.6 (a)

Comparison of Dispersion Curves
by the Effective Index Method
and Marcatili s Method.

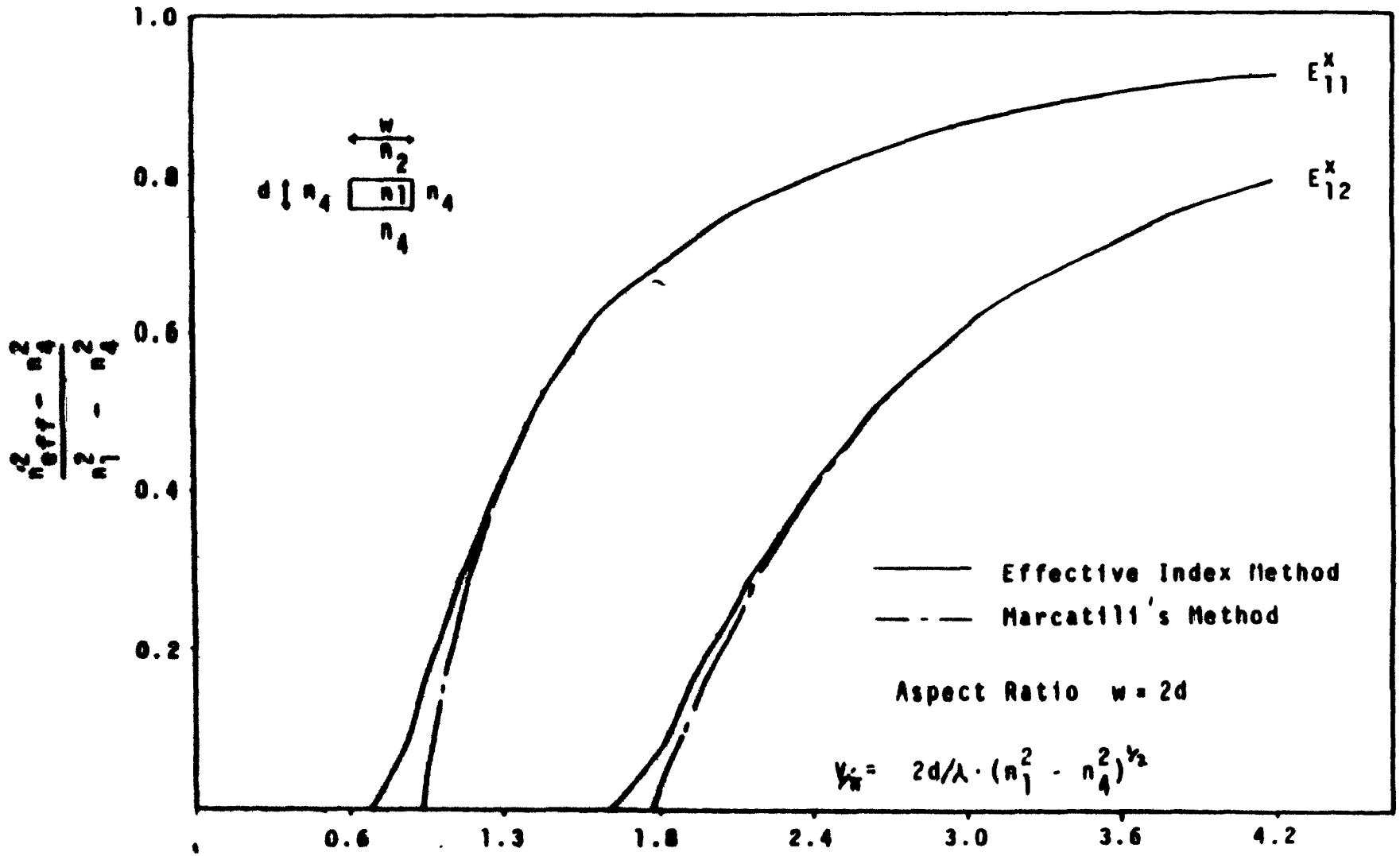

Figure 5.6

(b)

5.3 Transverse Field Distributions

The field expressions for channel guides, developed by Marcatili(2), will be employed to plot various transverse field distributions. The field expression for the electric field polarized in the y-direction, in the channel is as follows:

$$E^y = \frac{k_o^2 n_f^2 - k_y^2}{\omega \varepsilon n_f^2 k_z} M_1 \cos(k_x x + \alpha) \cos(k_y y + \beta)\, e^{j(\omega t - k_z z)} \tag{5.18}$$

n_f = uniform film index, $\omega = 2\pi c/\lambda$

Using the following initial conditions,

(1) $M_1 = 1$, $y = 0$ (center of channel guide), $\alpha = \beta = 0$

(11) suppress time & z dependence

we rewrite this field expression as:

$$E^y = \frac{k_o^2 n_f^2 - k_y^2}{\omega \varepsilon n_f^2 k_z} \cos(k_x x) \qquad \text{(field in channel)} \tag{5.19}$$

Using the same initial conditions, we write the field expression for fields outside the channel, in the substrate:

$$E^y = M_3 \frac{k_o^2 n_b^2 - k_y^2}{\omega \varepsilon n_b^2 k_z} e^{-jk_x x} \tag{5.20}$$

The constant M_3 assures a field match at the core-substrate boundary $x = w/2$, in keeping with the continuity of the electric field.

Using equations (5.9) and (5.10), and reducing them to approximate form, we can solve for k_x and k_y.

According to Marcatili (2);

$$k_z = (k_1^2 - k_x^2 - k_y^2)^{1/2}, \tag{5.21}$$

Employing the results from (5.21) and the following approximate expressions for (5.9) and (5.10):

$$k_x = \frac{p\pi}{w} \left(1 + \frac{A_3 + A_5}{\pi w}\right)^{-1} \tag{5.22}$$

(E^y_{pq} modes)

$$k_y = \frac{q\pi}{d} \left[1 + \frac{n_2^2 A_2 + n_4^2 A_4}{\pi n_1^2 d}\right]^{-1} \tag{5.23}$$

where $A_{2,3,4,5} = \lambda/2(n_1^2 - n_{2,3,4,5}^2)^{1/2}$, w = channel width, d = channel depth.

We can use expressions (5.19) and (5.20) and plot the E^y fields for various guide geometries and lateral mode numbers.

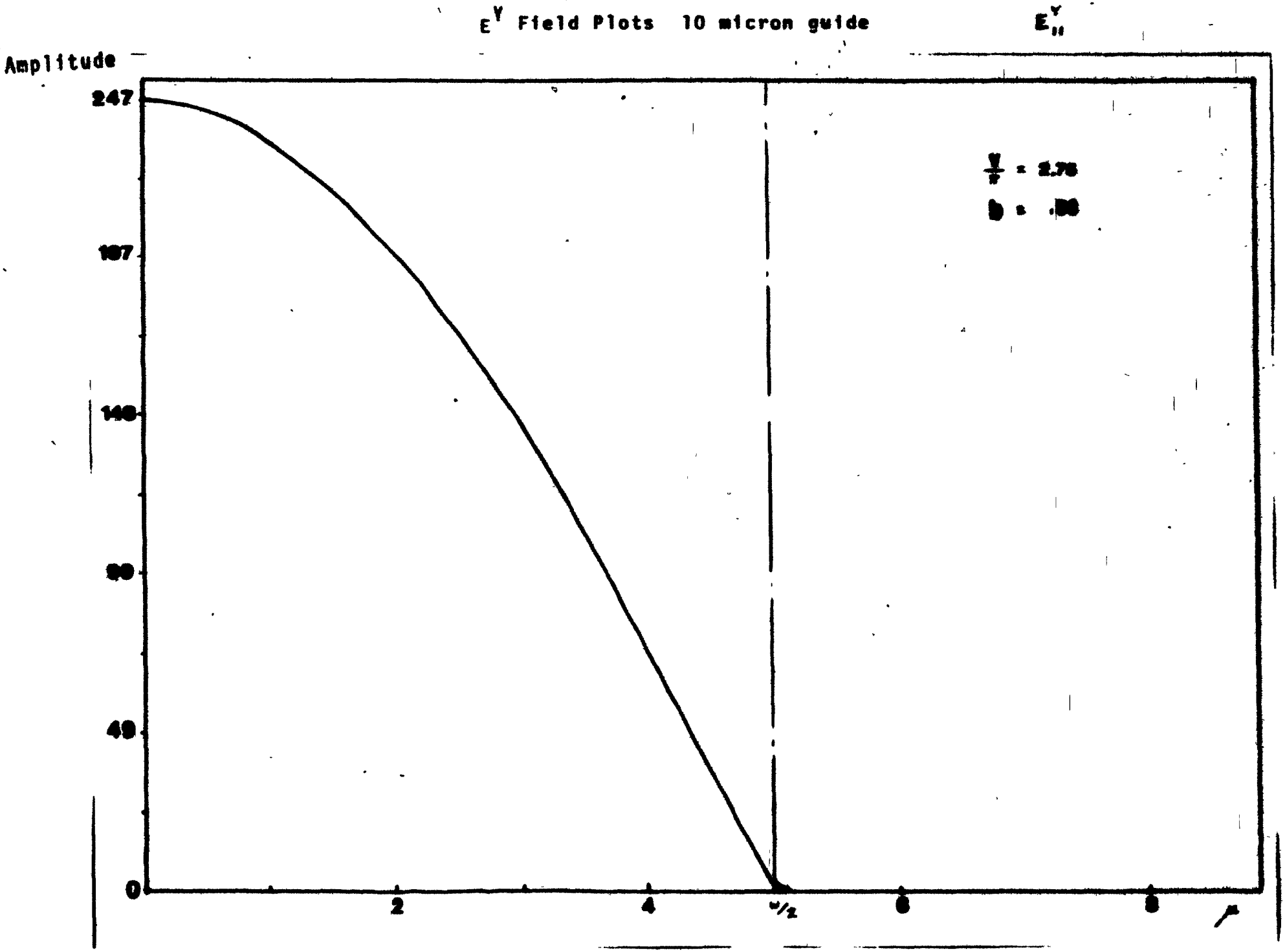
E^Y Field Plots 10 micron guide
E^Y_{11}
Amplitude
247
197
148
99
49
0
2
4
w/2
6
8
μ
width
$\frac{V}{V}$ = 2.76
b = .56

Figure 5.7

(a)

(b)

E_{11}^{Y}

E^Y Field Plots 20 micron guide E^Y_N

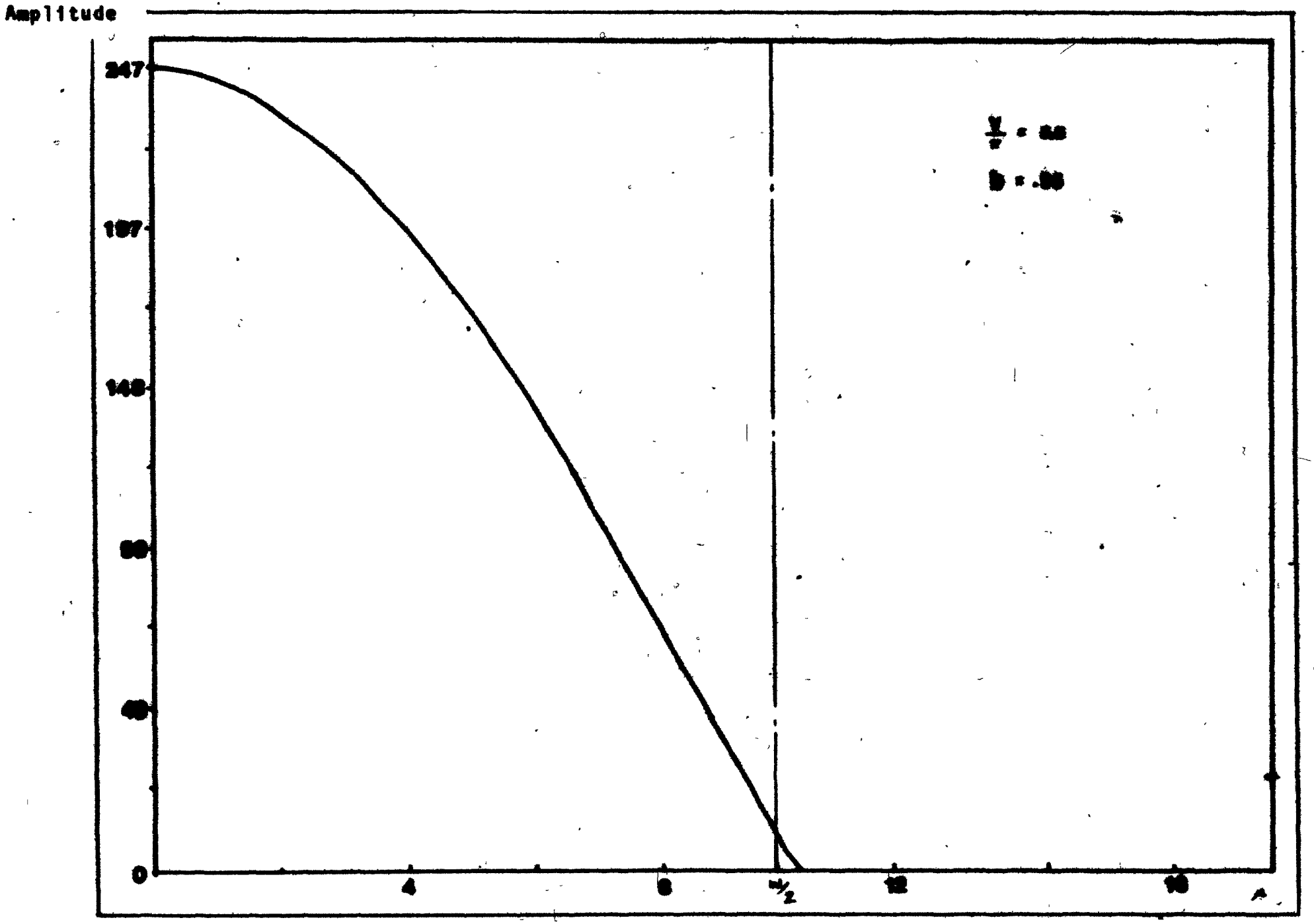

Figure 5.8 (a) width

/131

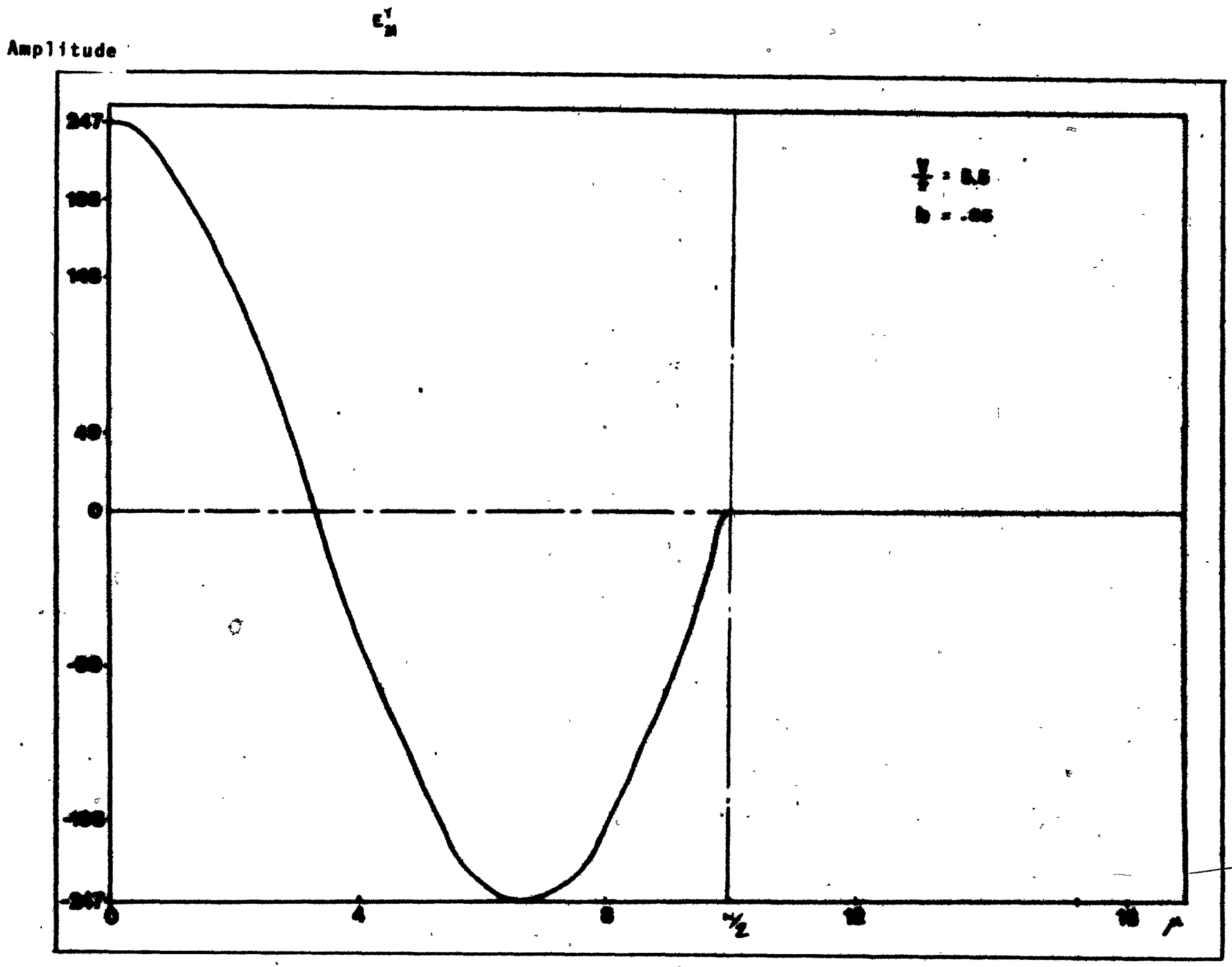
ε_{21}^{Y}
Amplitude
247
100
140
40
0
-100
-247
0
4
8
π/2
12
16
μ

(b)

wid

/132

$E_{41}^{\sim}$

Amplitude

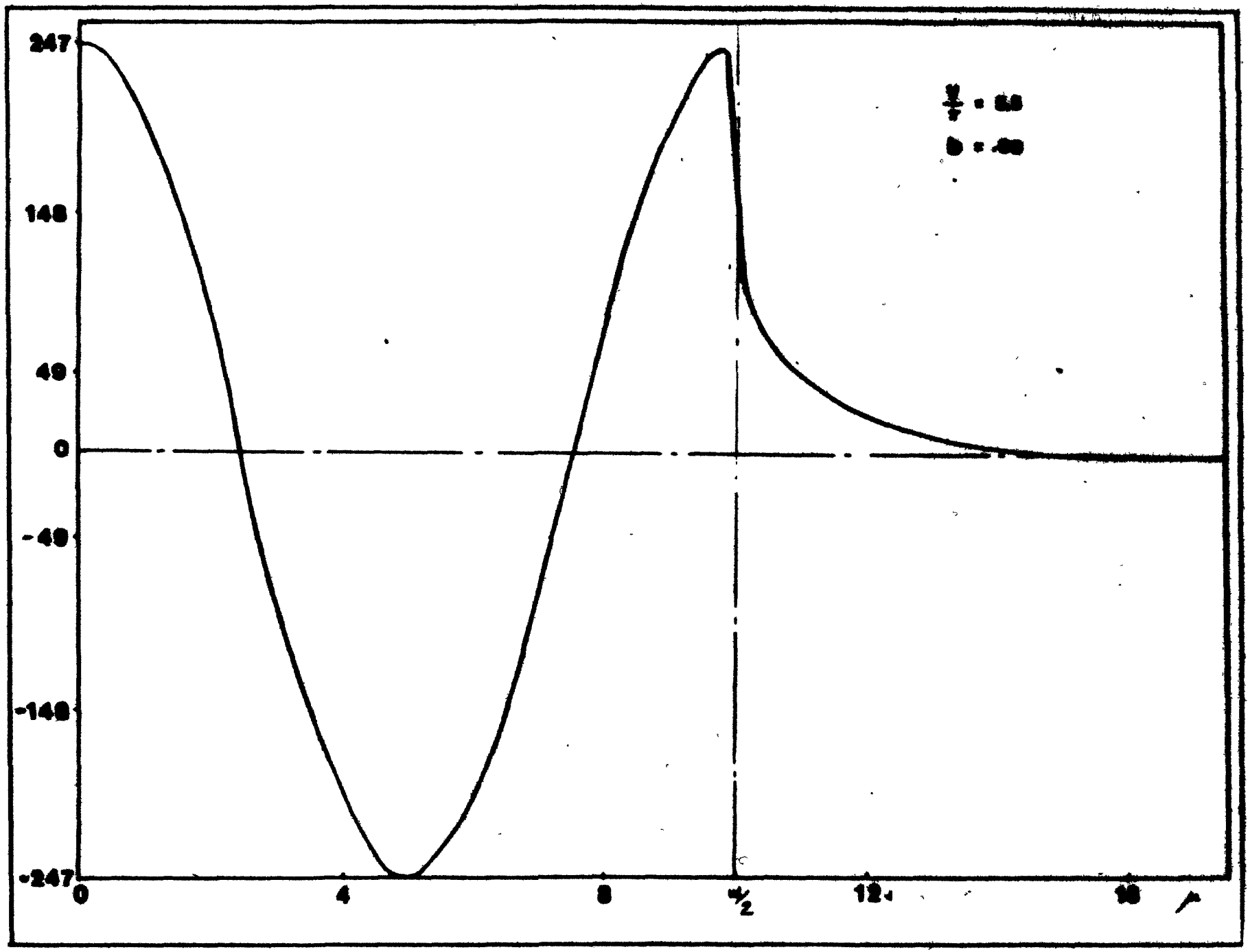

These plots are included in Fig. 5.7.a,b and 5.8.a,b,c. Figures 5.7(a) and (b) depict the E^y field for a guide width of 10 microns for the 1st and 2nd lateral modes respectively. The y axis coincides with the center of the channel.

Fig. 5.8(a),(b) and (c) show the E^y fields for a guide width of 20 microns for the 1st, 3rd and 4th lateral modes respectively.

The following field parameters were employed for all plots:
aspect ratio: width/depth = 2, $n_1 = 1.522$, $n_{3,4,5} = 1.512$, $n_2 = 1.0$, $\lambda = 0.6328\ \mu$.

Experimental Channel Guides

Channel guides have been fabricated in $AgNO_3$ salt melts, employing aluminum masks patterned by either the lift-off or etching technique. A mask consisting of 5, 10, 20 and 30 micron channels was used in the photolithographic process to study the effects of channel width on light propagation.

5.4 Substrate Preparation

The soda-lime glass substrates must be perfectly cleaned,

since the channel guides cannot tolerate any foreign particles which would be detrimental to wave guidance. The procedures outlined in Chapter 4 were applied to channel guide fabrication. It is recommended that the entire fabrication process be completed in the same day to sustain cleanliness and ease of mask preparation.

5.5 Aluminum Masking Procedures

Once the substrate was thoroughly cleaned, aluminum channels were patterned on the surface of the substrate either by etching the metal surface or using a method described as the lift-off technique. Since the ion exchange process is primarily a diffusion mechanism, the aluminum mask will prevent exchange in the desired area, creating embedded channel waveguides. Both methods of masking require patterning of a photoresist layer, with Shipley Az-1350J positive photoresist. Positive resist implies that the area exposed to an ultraviolet lamp is removed by development.

5.5.1 Spinning Photoresist

This was the method used to deposit a layer of photoresist, required for both Al masking operations. The dust particles on the substrate were removed with a spray of N_2 gas,

then the substrate was placed on the vacuum chuck of the spinner. The spin velocity was adjusted to 3000 RPM with quick ramp acceleration. Vacuum was applied to the chuck and the required amount of finely-filtered resist was applied, dependent on substrate size and shape.

The spin motor was switched on with the timing mechanism set to 30 seconds. After the spin process, the photoresist was prebaked in an oven set at 80°C for approximately 20 minutes. Once baked, the substrate was allowed to cool for a few minutes.

5.5.2 Exposure

In order to expose the photoresist film on the substrate surface, a precision mask aligner, with a well-collimated UV source was used. Using a mask made from chrome or a photo emulsion layer, the UV light was restricted to specific areas of the substrate surface. If an etching process is to be employed, a dark mask is required ie; clear channels surrounded by chrome, and for lift-off, the inverse mask is necessary. To form channels in the resist layer, the mask was aligned on the substrate and pressed to the substrate surface, employing light pressure provided by the vacuum stage on the mask aligner. The substrate was exposed to the UV

source (which had been preheated for at least 10 minutes) for the desired exposure time depending on the masking method.

5.5.3 Development

Two developer solutions were employed: a 1:1 ratio of developer and deionized (DI) water and a pure solution of developer. The exposed substrate was immediately immersed in the former solution for approximately 30 seconds. Any remaining photoresist in areas expected to be free of resist was carefully examined. It was then redeveloped in pure developer for a few seconds, cleaned with DI water and re-checked for fineness of pattern using a microscope. The photoresist layer was redeveloped for short periods in pure developer, until desired pattern accuracy was achieved.

5.5.4 Aluminum Film Deposition

The aluminum film can be applied to the substrate either by ion-gun deposition or evaporation. The latter technique was employed for the ion-exchanged channel guides. A vacuum pumping station with facilities for tungsten coil heating was used for the evaporation process. A tungsten coil was placed between the two heater terminals and two small hooks of Al wire, (half-inch) precleaned in methanol, were hung on

the coil. The bell jar was positioned over the apparatus containing the cleaned glass substrates and a rough vacuum was generated within, with the aid of the mechanical pump. Once a pressure of about 10^{-2} torr was attained, the vacuum source was switched over to the foreline circuit, to start fine pumping with the diffusion pump until a pressure of the order of 10^{-6} torr was achieved. With the shutter in place (protecting the substrate), the tungsten coil was slowly heated, keeping the heater current low, since the melting point of aluminum is only 660°C. The heater current was slowly increased until the Al hooks began to melt, then the shutter was opened and the current was maintained until the desired thickness was achieved. The shutter was then closed and the heater current switched off, while the film was allowed to oxidize for a few moments, before atmospheric pressure was restored to the bell jar.

5.5.5 The Etching Process

The etching process requires that an Al film, free of pin holes and other defects, be applied to the substrate first. A layer of photoresist must be spin coated on the aluminum then developed for 6-7 seconds. After development, the aluminum film is protected from the etchant, except in the channel area, which is free from resist.

An etchant was prepared using the following ratio

36 (H_2PO_4) ; 8 (DI water) ; 2 (nitric acid)

The substrate was immersed in the etchant and the etching process was observed. The etching time depended on the thickness of the Al film and its age. In view of this, continual monitoring of the substrate with the aid of a microscope was imperative to avoid undercutting. The cross-sectional geometry of a substrate prepared via etching is as illustrated in Fig. 5.9.

5.5.6 The Lift-off Process

In the case of lift-off, the photolithography preceeds the Al film deposition. As before, a layer of photoresist was spincoated on the substrate, and was exposed for 10-12 seconds, a longer exposure in this case, since there was no reflective layer of aluminum. Once developed, the aluminum film could then be evaporated onto the substrate. After evaporation, the substrate was immersed in a bath of cold acetone for 10-15 minutes. The acetone would attack the photoresist underneath the film and cause the aluminum on top of it to "lift-off".

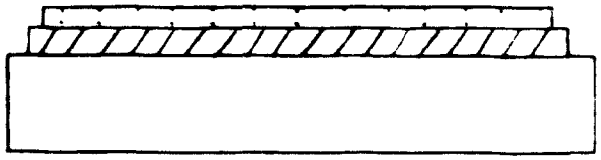

(a) Three Layer Structure

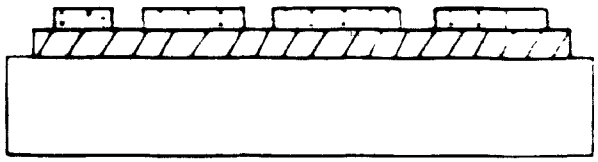

(b) After Exposure & Development

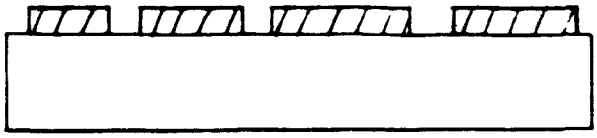

(c) After Etching

aluminum

photoresist

substrate

Figure 5.9 Stages of Aluminum Masking (Etching)

Figure 5.10 Stages of Aluminum Masking (Liftoff)

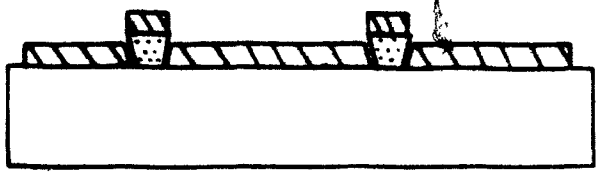

(a) After Aluminum Deposition

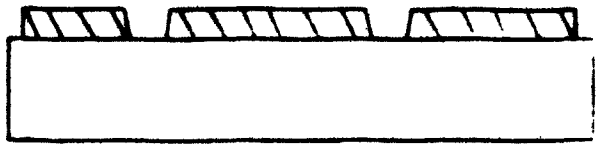

(b) After Liftoff

Aluminum Channel Mask

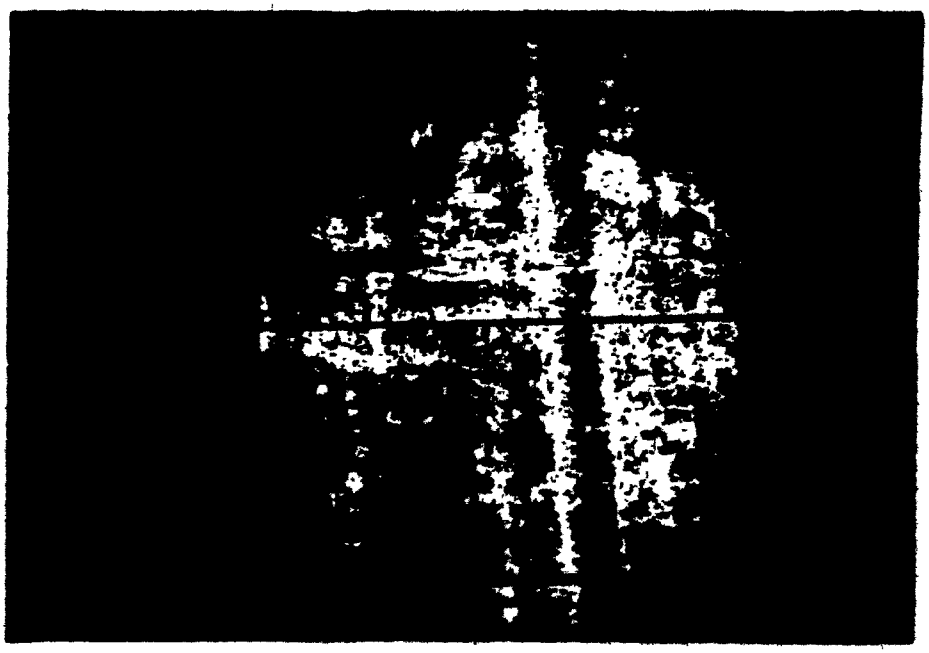

Figure 5.11

5.6 Ion-Exchange

Once the desired waveguide pattern was scribed in the aluminum film, (also termed window-opening in semiconductor terminology) the substrate was ready to be exchanged. Several substrates were prepared for exchange in $AgNO_3$ and KNO_3 salt baths under conditions for single-mode (in depth) guidance.

Experimental Conditions

- KNO_3 Exchange

  Temperature: 400°C Time: 55 minutes

  Synchronous angle for depth mode excitation: 7.6903°

- Dilute $AgNO_3$ - $NaNO_3$ Exchange (m_B/m_A = 0.001)

  Temperature: 315°C Time: 2 minutes

  Synchronous angle for depth mode excitation: 7.5125°

After the exchange process, the substrates were removed from the furnace and were allowed to cool down to room temperature.

Before attempting to measure the propagation cha-

racteristics of the ion-exchanged channel guides, the aluminum mask on the surface of the substrate must be removed. This is imperative, since a thin metal layer on top of a dielectric waveguide is essentially a cladding layer, which perturbs the field.

A drop of photoresist at the input and output locations of each channel was used to preserve small markings of the channel locations after the rest of the mask was etched away. This greatly facilitated the coupling procedure since the channel became invisible to the naked eye after the mask was etched completely from the substrate surface.

5.7 Experimental Setup and Measurements

The scheme for measuring the modal propagation constants for the Ag^+ and K^+ ion exchanged channel waveguides was essentially the same as what was described for slab waveguide measurement in Chapter 2. The only additional equipment used was a goniometer for the exitation of the lateral modes.

As can be verified in the photographs on the following pages, the M-line structure for channel guides is significantly more complex than for slab guides. Corresponding to each M-line in depth, there is a broken M-line representing

the lateral modes, with a number of dark and bright spots dependent on the channel width.

Following Marcatili's (2) nomenclature, the p parameter represents the number of depth modes. In reference to Fig.5.12 the angle φ determines which q mode is excited while the angle ψ determines which p mode is excited.

The dimensions of the channel guide (dependent on the melt time and temperature) dictate the angular spacing of the transverse M-lines. It was relatively simple to excite depth modes in the channels once the prisms were properly positioned, but excitation of separate transverse M-lines was nearly impossible. Having no intensity detector for the output spots made it difficult to resolve which lateral mode in the group was the most intense for a given angle of ψ. It was as if several lateral modes were being excited simultaneously for one specific angle of ψ. See Figs. 5.13, 5.14.

In order to estimate the number of lateral modes excited for given experimental parameter, equation 5.24 can be employed:

$$p = \frac{2\pi a}{\lambda}\sqrt{n_{eff}^{2} - n_{b}^{2}} \qquad (5.24)$$

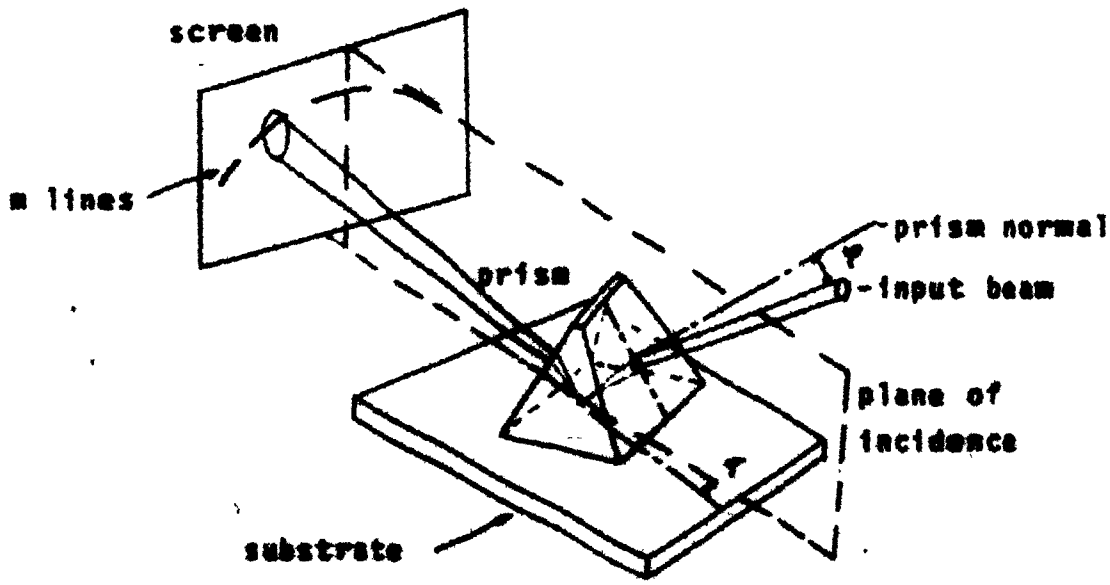

Figure 5.12 Prism Angles

M line Photos for $AgNO_3$ Channel Guides

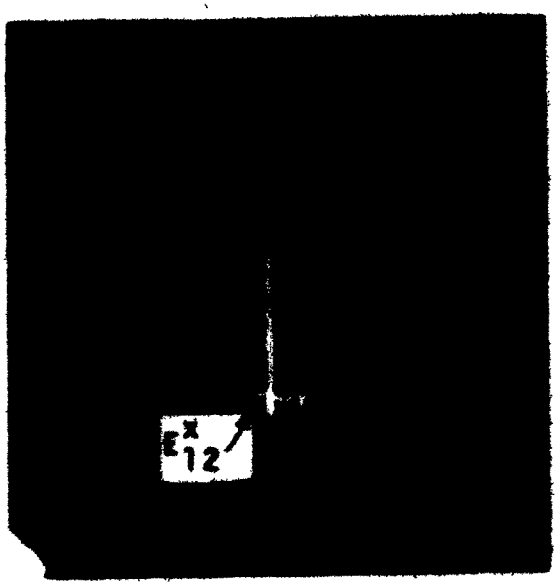

10μ channel E^x_{11} mode

20μ channel E^x_{11} mode

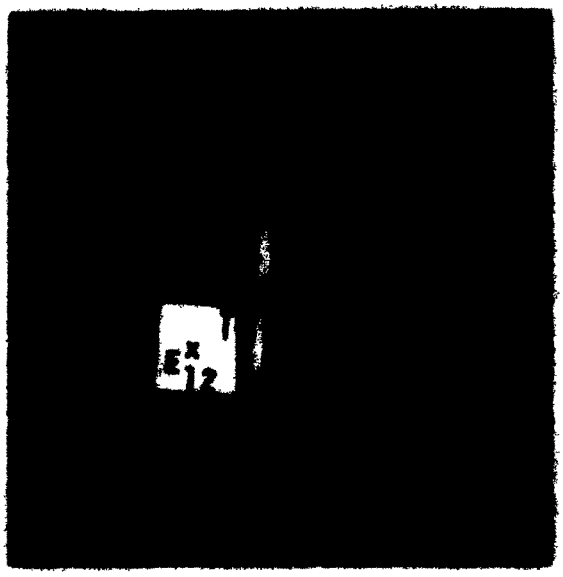

30μ channel E^x_{11} mode

Figure 5.13

M line Photos for KNO_3 Channel Guides

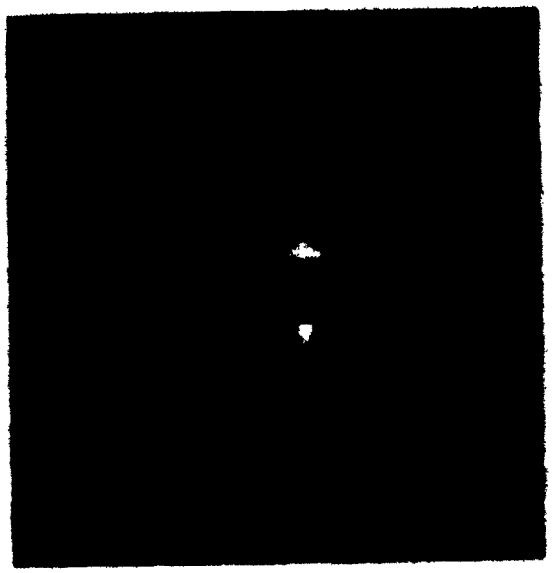

30μ channel $E^x_{\bar{p}1}$ mode
(central maximum blocked)

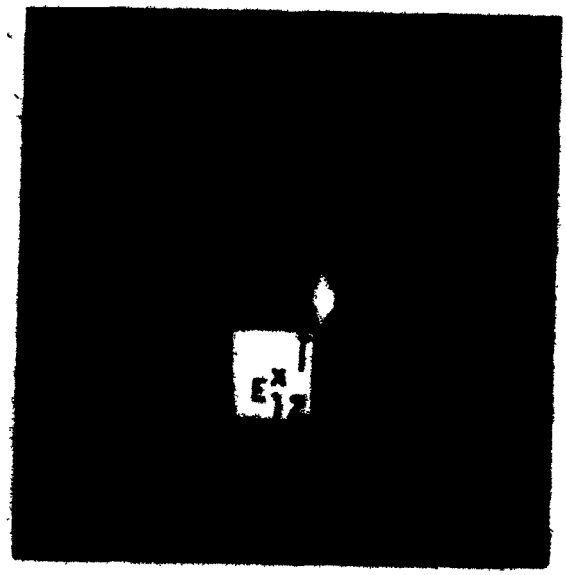

30μ channel E^x_{11} mode

Figure 5.14

CHAPTER VI

CONCLUSION AND DISCUSSION

This thesis has generated a complete characterization of slab waveguides formed by ion exchange in $AgNO_3$ and KNO_3 molten salts. Although $AgNO_3$ slab guides have been previously characterized by other researchers, it is the author's understanding that KNO_3 slab guides have not yet been fully characterized to this extent. The theoretical analysis involved the generation of dispersion curves based on a Gaussian index profile, (found to be the closest approximation to KNO_3 refractive index profiles within the author's efforts), employing both the WKB and staircase approximation. Numerous refractive index profiles for various KNO_3 slab guides were also constructed from the experimentally measured modal index values.

The fabrication procedures for $AgNO_3$ and KNO_3 slab guides have been outlined, and the use of a vertical furnace, with an additional thermocouple to monitor the melt temperature results in a repeatable manufacturing process. However, due to limitations in the measurement procedure, it is difficult to determine exactly how repeatable the experimental trials are. More precise measurements of the mode indices could be obtained by employing a simple photo-detector and slit assem-

bly to determine the position of maximum intensity of a particular M-line, rather than relying on the naked eye.

It was observed that by diluting the $AgNO_3$ melt with $NaNO_3$, the surface index of the resulting waveguide could be reduced, as well as the waveguide depth. It has also been reported (13) that slab guides formed from diluted $AgNO_3$ tend to be more stable than their pure counterparts.

KNO_3 ion exchanged guides, which have been characterized in Section 4.10 of this thesis, are less costly to produce, and hence would appear to be better candidates for an optical device manufacturing process. Because the melt temperature required for KNO_3 exchange is much higher than that of $AgNO_3$ exchange, and the exchange time for a single mode guide in KNO_3 is longer than that for the same guide in $AgNO_3$, the manufacturing tolerances for KNO_3 exchange are considerably relaxed, when compared to $AgNO_3$ exchange requirements. This factor can be employed to the designer's advantage; the effective refractive index of the substrate can be selectively adjusted, with ease, to meet the requirements of a specific device, as could be the case in adjusting the refractive index of the coupling region in a directional coupler.

Device fabrication in integrated optics requires

light guiding structures in the form of dielectric channel waveguides. Theoretical calculations were performed to determine the propagation characteristics of this channel structure based on Marcatili's analysis (2) and the effective index method (24). Since both of these methods assume a homogeneous guiding region, some improvements could be realized by taking into account the inhomogeneous nature of ion exchanged guides. (More exact calculations are theoretically speaking, possible by including the effects of lateral or transverse diffusion, as well as inhomogeniety in depth). However, it is difficult to estimate how much more accuracy can be obtained. For experimental pruposes, the effective index method yields reasonably good results for verification of measured data.

In regard to the experimental trials in general, the calibration trials could have led to more precise results if glass substrates of well known composition and refractive index were employed, rather than using common microscope slides (soda-lime glass). Nevertheless, the calibration results produced from the slab trials were of sufficient benefit in the manufacture of single mode channel guides in $AgNO_3$, dilute $AgNO_3$ and KNO_3.

The photolithographic laboratory was vastly improved as a result of the installation of a new photoresist

spinner, mask aligner and a dust-free, temperature controlled environment. These factors enabled a resolution in the micron range; an order of magnitude smaller than was possible with the previous equipment. New techniques, such as immersing the photoresist coated substrate in chlorobenzene before development enabled well defined edges in the photoresist windows, resulting in a more sharply patterned aluminum mask following the etching process.

Concerning the measurements of the maxima of the M-line patterns for channel guides, a major problem prevented us from recording data; experimental measurements of the lateral M-lines were inhibited due to the absence of the photodetector set-up, so theoretical results could not be checked with measured modal indices.

As a further project, the properties of the thermooptic effect in glass could be studied,(41) to gain insight into its relationship with KNO_3 ion exchanged guides. By supplying an external voltage to small heaters positioned over the channels and separation region of the device, the resulting localized increase in temperature changes the refractive index and thereby alters the coupling characteristics. The use of a dc signal enables the device to operate as a switch while an ac signal results in a low-frequency modulator.

It is hoped that the previous suggestions for possible improvements in the fabrication and measurement techniques, as well as the considerations for future work will generate continuing studies in the use of the ion-exchange technique for device research and applications in integrated optical circuits

APPENDIX A

1. Derivations for basic diffusion theory

First define the flux of a diffusing species as [31]

$$F(x) = -D\frac{\partial C}{\partial x} + \mu EC \qquad (A.1)$$

where F. the number of species passing through a unit area in a given time

D: diffusion $= \frac{kT}{q}\mu = D_o e^{-E_a/kT}$ [4]

q: charge

μ: mobility

C: concentration of diffusant

E: applied electric field

E_a: activation energy

D_o: diffusivity constant

Next, consider the transport equation which is the increase in density of material per unit area per unit time, equivalent to $F_{in} - F_{out}$. [31]

$$\Delta x\frac{\partial \bar{C}}{\partial t} = F(x) - F(x + \Delta x) \qquad (A.2)$$

$\bar{C}$: average concentration in element.

As $\Delta x \to o$, then (1) $\bar{C} \to C(x)$

(2) $\frac{F(x) - F(x + \Delta x)}{\Delta x} \to \frac{\partial F}{\partial x}$

Therefore $\frac{\partial C}{\partial t} = -\frac{\partial F}{\partial x}$ (A.3)

(1-d transport equation)

Using equations (A.1) and (A.2) we derive:

$$\frac{\partial C}{\partial t} = D\frac{\partial^2 C}{\partial x^2} - uE\frac{\partial C}{\partial x} \quad (A.4)$$

Neglect the effects of the electric field, and write the one dimensional diffusion equation as:

$$\frac{\partial C}{\partial t} = D\frac{\partial^2 C}{\partial x^2} \quad (A.5)$$

when D is concentration dependent, we rewrite (A-5) as follows:

$$\frac{\partial C}{\partial t} = \frac{\partial}{\partial x}\left(D\frac{\partial C}{\partial x}\right) \quad (A.6)$$

2. <u>Derivation of the interdiffusion coefficient</u> [33]

Define the electrical flux as:

$$(F_i)_{el} = -u_i z_i \nabla\phi C_i$$

where ϕ: electric potential

C: concentration

z: electrochemical valence

u: electrochemical mobility

u_i: $\frac{D_i F}{RT}$ (with R: gas constant, D_i diffusion coefficient)

Define the thermal flux as: $(F_i)_{th} = -D_i \nabla C_i$

and the net flux as: $F_i = (F_i)_{th} + (F_i)_{el}$ (A.8)

$$= - D_i (\nabla C_i + z_i C_i \cdot \frac{\bar{F}}{RT} \nabla \Phi)$$

where $\bar{F}$: Faraday's constant

Particle diffusion assumes the following:

$z_A \bar{C}_A + z_B \bar{C}_B = \text{Const}$ (electroneutrality) (A.9)

$z_A F_A + z_B F_B = 0$ (no electric current)

We can eliminate the electric potential in (A.8) by using (A.9)

$$F_A = -\left[\frac{\bar{D}_A D_B (z_A^2 \bar{C}_A + z_B^2 \bar{C}_B)}{z_A^2 \bar{C}_A \bar{D}_A + z_B^2 \bar{C}_B \bar{D}_B} \right] \nabla \bar{C}_A \qquad \text{(A.10)}$$

Combine (A.10) with Fick's 2nd law $(\frac{\partial \bar{C}_A}{\partial t} = -\nabla \cdot F_A)$ [31] and rederive A.6

$$\frac{\partial C_A}{\partial t} = \frac{\partial}{\partial x} (\bar{D}_{AB} \frac{\partial \bar{C}_A}{\partial x}) \qquad \text{(A.11)}$$

APPENDIX B

COMPUTER SOFTWARE GENERATED FOR THE VARIOUS DISPERSION CURVE CALCULATIONS

1. Step Index Calculations

For the homogeneous or step index, the following equation was programmed:

$$V = \left[m\pi + \tan^{-1}\sqrt{b/1-b} + \tan^{-1}\sqrt{b + a/1-b} \right] / \sqrt{1-b} \qquad (B.1)$$

and solution for V was obtained by varying the mode number m, in an outer loop and incrementing b in an inner loop.

As input to the program, the necessary data includes, the number of modes to be solved, the step size for incrementing b, and the assymmetry measure for a homogeneous waveguide as well as the radius of convergence for the root search portion of the algorithm.

Because the experimental data for the ion exchanged waveguides did not correlate with the theoretical, homogeneous data, the homogeneous modelling scheme was abandoned. The following analysis is presented for tutorial pur-

poses, as well as an example of how to obtain a single film index, n_f, from an inhomogeneous waveguide.

Essentially, equation B.1 is rearranged in the following manner, in the quest of a root within the required radius of convergence:

$$\tan^{-1}\sqrt{(N_{eff}^2 - 1)/(n_f^2 - N_{eff}^2)} + \tan^{-1}\sqrt{(N_{eff}^2 - n_b^2)/(n_f^2 - N_{eff}^2)}$$

$$+ m\pi - (\sqrt{n_f^2 - N_{eff}^2})\, dk = 0 \qquad (B.2)$$

d: guide thickness

k: Free space propagation constant

Once a zero has been located, the corresponding b value is stored (since it contains information on n_f) and the mode number is incremented. The desired value for the uniform film index approximation is the average value of the m film indices. A flow chart outlining the software is contained in Figure B.2 (tol = 10^{-5})

2. Graded Index Calculations

To plot inhomogeneous or graded index dispersion curves, the method outlined by Hocker [21], employing the

WKB approximation was applied. The equation to be programmed in this case is:

$$v \int_{0}^{\alpha_t} \left[n(\alpha) - b\right]^{1/2} d\alpha = (m + 1/4)\pi + \tan^{-1}\sqrt{(b + a)/1-b} \tag{B.3}$$

$n(\alpha)$:	diffusion profile	a:	asymmetry
b:	normalized guide index	m:	mode index
v:	normalized frequency	α_t:	turning point

The logic of the program proceeds as follows: solve for α_t by using the fact that $n(\alpha_t) = b$, for each increment of b. Next solve the WKB integral expression and finally solve for v in equation (B.3). All that is required on input is a function describing the diffusion profile, the number of modes to be solved for and the increment value for b. A flow chart describing this procedure is included in Figure B.3.

To correlate theory and experimental data, the measured experimental mode indices were normalized via equations (3.40, 3.41) and then located on the universal dispersion chart. As mentioned in chapter 3, a more refined value of n_s (Heidrich & White method) was calculated to yield a comparison between the theoretical and experimental dispersion curves.

The IMSL routine DCADRE relies on Rhomberg integration techniques to solve the WKB integral. Rhomberg integration is based on the use of the trapezoidal rule combined with Richardson extrapolation. The trapezoidal rule estimates of the integral are denoted as: [37]

$$T_{\ell,k} = \frac{\Delta x}{2}\left[f(a) + f(b) + 2\sum_{j=1}^{\ell} f(a + j\Delta x)\right] \qquad (B.4)$$

a,b: interval of integration, $\Delta x = (b-a)/\,2^{k-1}$

$\ell = 2^{k-1} - 1$

Note that the extrapolation is carried out according to:

$$T_{\ell k} = 1/(4^{\ell-1} - 1)\left[4^{\ell-1}\, T_{\ell-1,\, k+1} - T_{\ell-1,k}\right] \qquad (B.5)$$

Equation B.4 and B.5 can be combined and the results placed in tabular form as in Table B.1.

Increasingly accurate trapezoidal rule values

Increasingly accurate extrapolated values

T_{11}					
T_{12}	T_{21}				
T_{13}	T_{22}	T_{31}			
T_{14}	T_{23}	T_{32}	$T_{4,1}$		
"	"	"	"		
"	"	"	"	$T_{\ell-1,}$	
$T_{1,\ell}$	$T_{2,\ell-1}$	$T_{3,\ell-2}$	.....	$T_{\ell-1,2}$	$\longrightarrow$ $T_{\ell,1}$ accurate Rhomberg result.

<u>Table B-1</u>

Convergence criterion:

$$\left| \frac{T_{\ell,1} - T_{\ell-1,1}}{T_{\ell,1}} \right| < \epsilon \qquad (B.6)$$

For a more detailed analysis, consult "Numerical Methods" by R. Hornbeck [37]

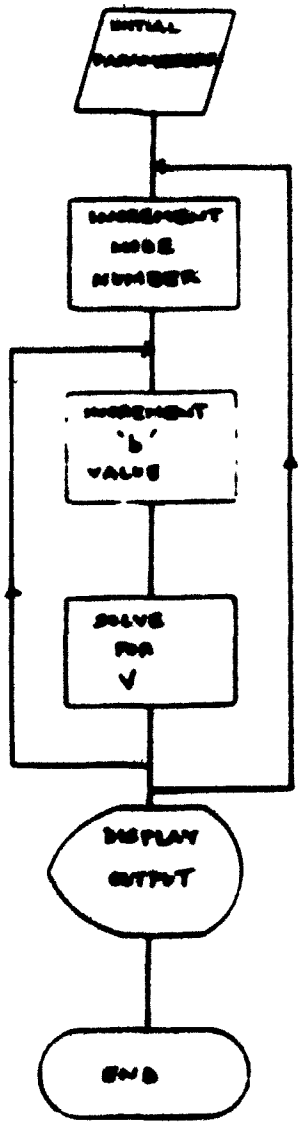

Homogeneous Dispersion Curve flow chart.
Figure B.1

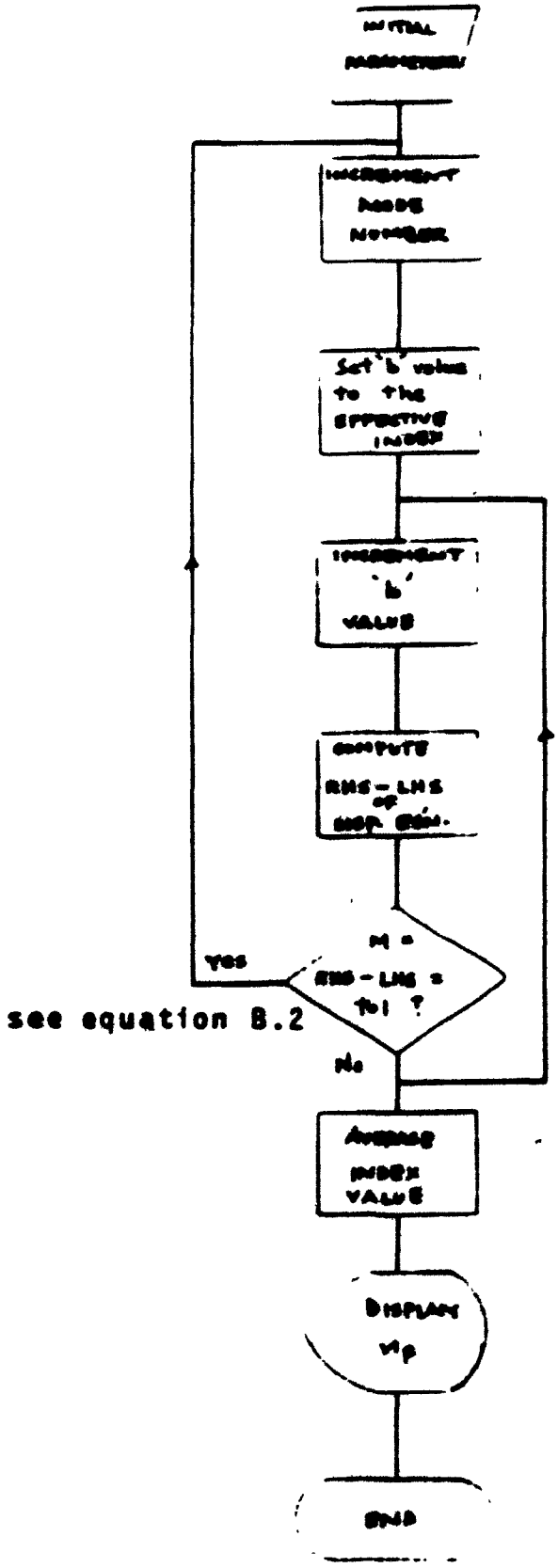

Film Index Approximation Flow Chart. Figure B.2

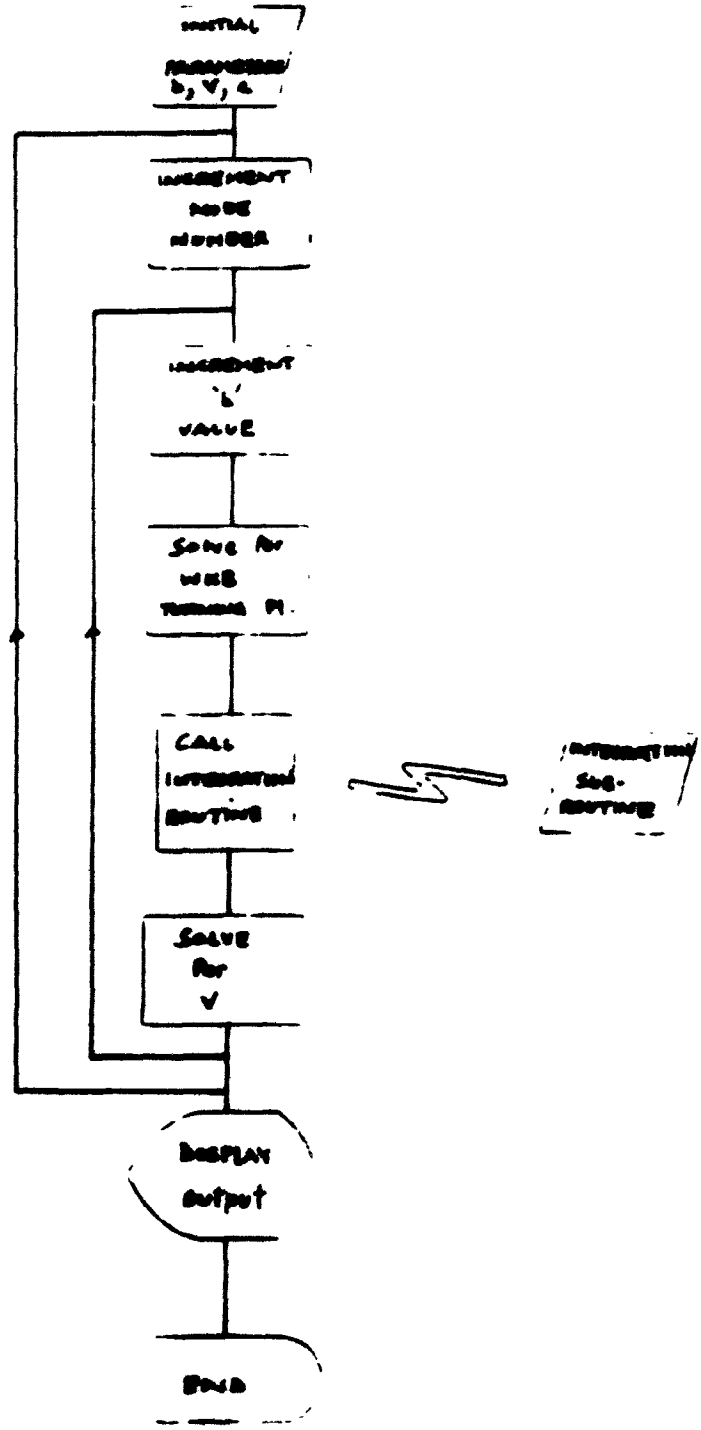

Graded Index Dispersion
Curve Flow Chart Figure 8.3

APPENDIX C

1. DERIVATION OF THE NORMALIZED DEPTH EQUATION FOR THE PROFILING ROUTINE

In order to derive equation (3.29), expand equation (3.26) as follows:

$$\sum_{k=1}^{M} \int_{\bar{z}_{k-1}}^{\bar{z}_k} \left(\{n(\bar{z})-n_m\}\cdot\{n(\bar{z}) + n_m\}\right)^{\frac{1}{2}} d\bar{z} \qquad (C.1)$$

Now use expression (3.28) to derive

$$\sum_{k=1}^{M} \int_{\bar{z}_{k-1}}^{\bar{z}_k} \left[(n(\bar{z}) - n_m) \cdot \frac{n_{k-1} + n_k + 2n_m}{2}\right]^{\frac{1}{2}} d\bar{z} \qquad (C.2)$$

and by employing (3.27) we rework equation (C.2) into

$$\sum_{k=1}^{M} \sqrt{\frac{n_{k-1} + n_k + 2n_m}{2}} \int_{\bar{z}_{k-1}}^{\bar{z}_k} \left[n_k + \frac{n_{k-1} - n_k}{\bar{z}_k - \bar{z}_{k-1}} \cdot (\bar{z}_k - z) - n_m\right]^{\frac{1}{2}} d\bar{z} \qquad (C.3)$$

Let $a = n_k - n_m$, $\quad b = \dfrac{n_{k-1} - n_k}{\bar{z}_k - \bar{z}_{k-1}}$

and consider $a + b\,(\bar{z}_k - \bar{z}) = x$

$$-\,b\,d\bar{z} = dx$$

$$d\bar{z} = -1/b\;dx$$

Using the above change in variables, equation (C.3) can be written as:

$$-\,1/b \int \sqrt{x}\;dx = \frac{-2}{3b}\;x^{3/2}$$

$$= \frac{-2}{3b}\left[a + b(\bar{z}_k - \bar{z}_k)\right]^{3/2}\Bigg|_{\bar{z}_{k-1}}^{\bar{z}_k} =$$

$$= -\frac{2}{3b}\,a^{3/2} + \frac{2}{3b}\left[a + b(\bar{z}_k - \bar{z}_{k-1})\right]^{3/2}$$

$$= \frac{2}{3b}\left(\left[a + b\,(\bar{z}_k - \bar{z}_{k-1})\right]^{3/2} - a^{3/2}\right) \qquad \text{(C.4)}$$

Now substitute for a and b in equation (C.4):

Now substitute for a and b in equation (C.4):

$$\sum_{k=1}^{M} \sqrt{\frac{n_k + n_{k-1} + 2n_m}{2}}$$

$$\times \frac{2}{3} \frac{\bar{z}_k - \bar{z}_{k-1}}{(n_{k-1} - n_k)} \left[\left[(n_k - n_m + \frac{n_{k-1} - n_k}{\bar{z}_k - \bar{z}_{k-1}}) (\bar{z}_k - \bar{z}_{k-1}) \right]^{3/2} - (n_k - n_m)^{3/2} \right]$$

$$= \frac{4m - 1}{8} \qquad \text{(C.5)}$$

By simplifying and breaking (C.5) into the m-1 and m^{th} term, we write

$$\sum_{k=1}^{M-1} \left(\frac{n_k + n_{k-1} + 2n_m}{2} \right)^{1/2} \cdot \frac{\bar{z}_k - \bar{z}_{k-1}}{n_{k-1} - n_k} \left[(n_{k-1} - n_m)^{3/2} - (n_k - n_m)^{3/2} \right] + \frac{2}{3} \left(\frac{3n_m + n_{m-1}}{2} \right)^{1/2}$$

$$\times \left[\frac{(n_{m-1} - n_m)^{3/2}}{n_{m-1} - n_m} - \frac{(n_m - n_m)^{3/2}}{n_{m-1} - n_m} \right] \left(\bar{z}_m - \bar{z}_{m-1} \right) = \frac{4m-1}{8} \qquad \text{(C.6)}$$

Rearrange the above expression to get the final expression for $\bar{z}_m$;

$$\bar{z}_m = \frac{3}{2} \left[\frac{3n_m - n_{m-1}}{2} \right]^{-1/2} \times (n_{m-1} - n_m)^{-1/2} \times \left[\frac{4m-1}{8} - \frac{2}{3} \sum_{k=1}^{M-1} \left(\frac{n_k + n_{k-1} + 2n_m}{2} \right)^{1/2} \right.$$

$$\left. \times \frac{\bar{z}_k - \bar{z}_{k-1}}{n_{k-1} - n_k} \left[(n_{k-1} - n_m)^{3/2} - (n_k - n_m)^{3/2} \right] \right] + \bar{z}_{m-1}$$

$$m = 2, 3, 4, \ldots M \qquad \text{(C.7)}$$

with $z_1 = 9/16 \left(\frac{n_o + 3n_1}{2} \right)^{-1/2} \cdot (n_o - n_1)^{-1/2}$ (C.8)

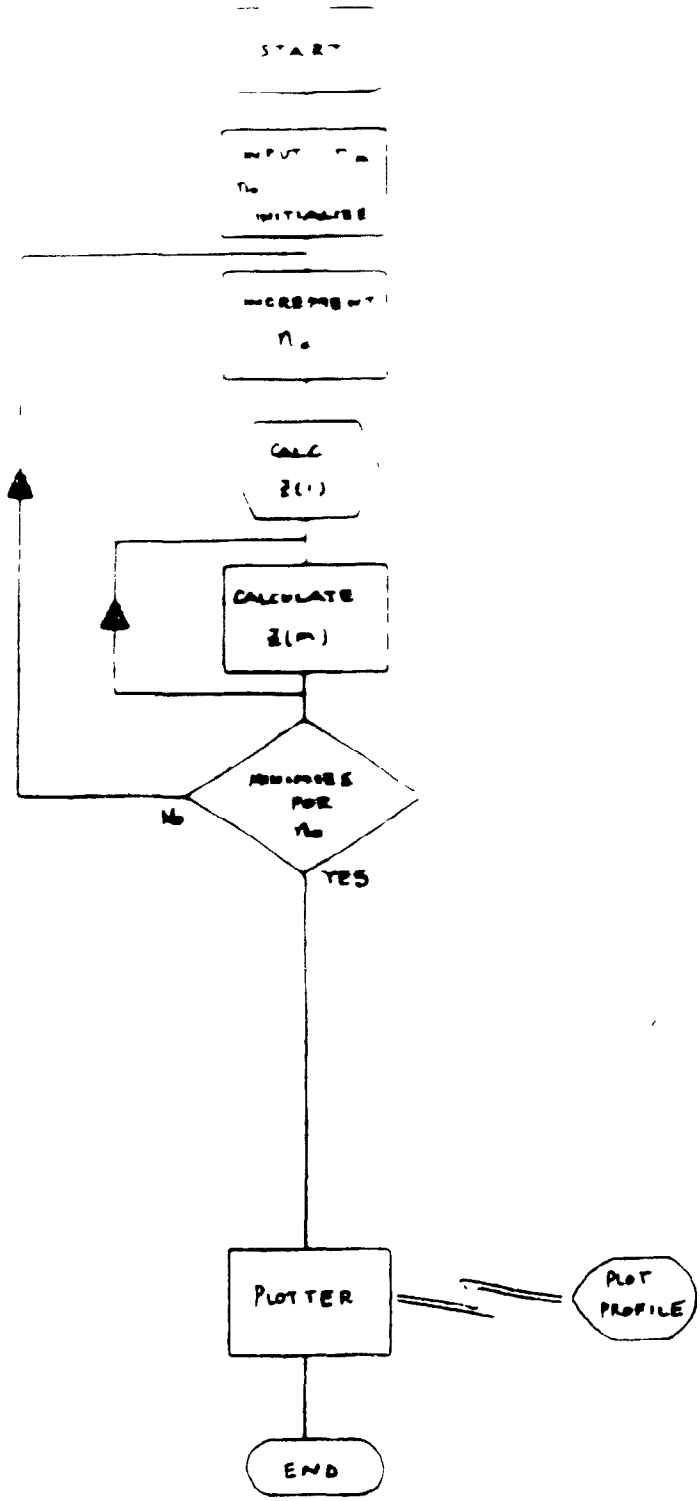
START
CALC
Z(1)
CALCULATE
Z(m)
NO
YES
PLOTTER
PLOT
PROFILE
END

APPENDIX

DISPERSION CURVES BY THE STEP APPROXIMATION METHOD

Discussion

As outlined in Chapter 3 the step approximation method models an inhomogeneous slab waveguide by dividing it into as many homogeneous layers necessary to achieve the desired accuracy The method is based on identifying the fields quantities in each layer and matching the $\bar{E}$ and $\bar{H}$ fields at the boundaries so as to comply with the condition of continuity of the tangential fields

In order to have the problem stated in a manner convenient for computer manipulation, the matrix form of the dispersion equation is adopted:

$$\Gamma x = 0 \qquad (D.1)$$

coefficient matrix x: field amplitude vector

The dispersion equation in matrix form is expressed as follows:

$$\det \Gamma = 0 \qquad (D.2)$$

The size of the coefficient matrix is directly proportional to the number of layers initially assumed. Because the number of

operations to be performed by the computer is dependent on the order of the matrix, it is important to choose the number of layers that will accurately model the profile, yet keep the number of operations manageable. As evident from the results presented in Chapter 3, five steps appear to yield reasonable accuracy while allowing ease of computation.

2 Program Overview

The program can be broken into three main sections. The first section defines the necessary transverse propagation constants, dependent on the value of $\bar{\beta}$ chosen. This calculation is done in the main program. The coefficient matrix is loaded, element by element in a subroutine entitled matrix. The root-searching portion of the program stores both the matrix subroutine and a determinant finding routine. The task flow is then:

(1) define transverse propagation constants

(2) formulate coefficient matrix

(3) find determinant of the matrix

(4) repeat (2) & (3) until a root is located

(5) change $\bar{\beta}$ and start at step (1)

Refer to flowchart D.1 for detailed logic.

Before the program can be run, it is necessary to perform a detailed, five step quantization as outlined in Chapter 3 The resulting information on normalized guide indices and transverse boundary locations is used as input data to the program

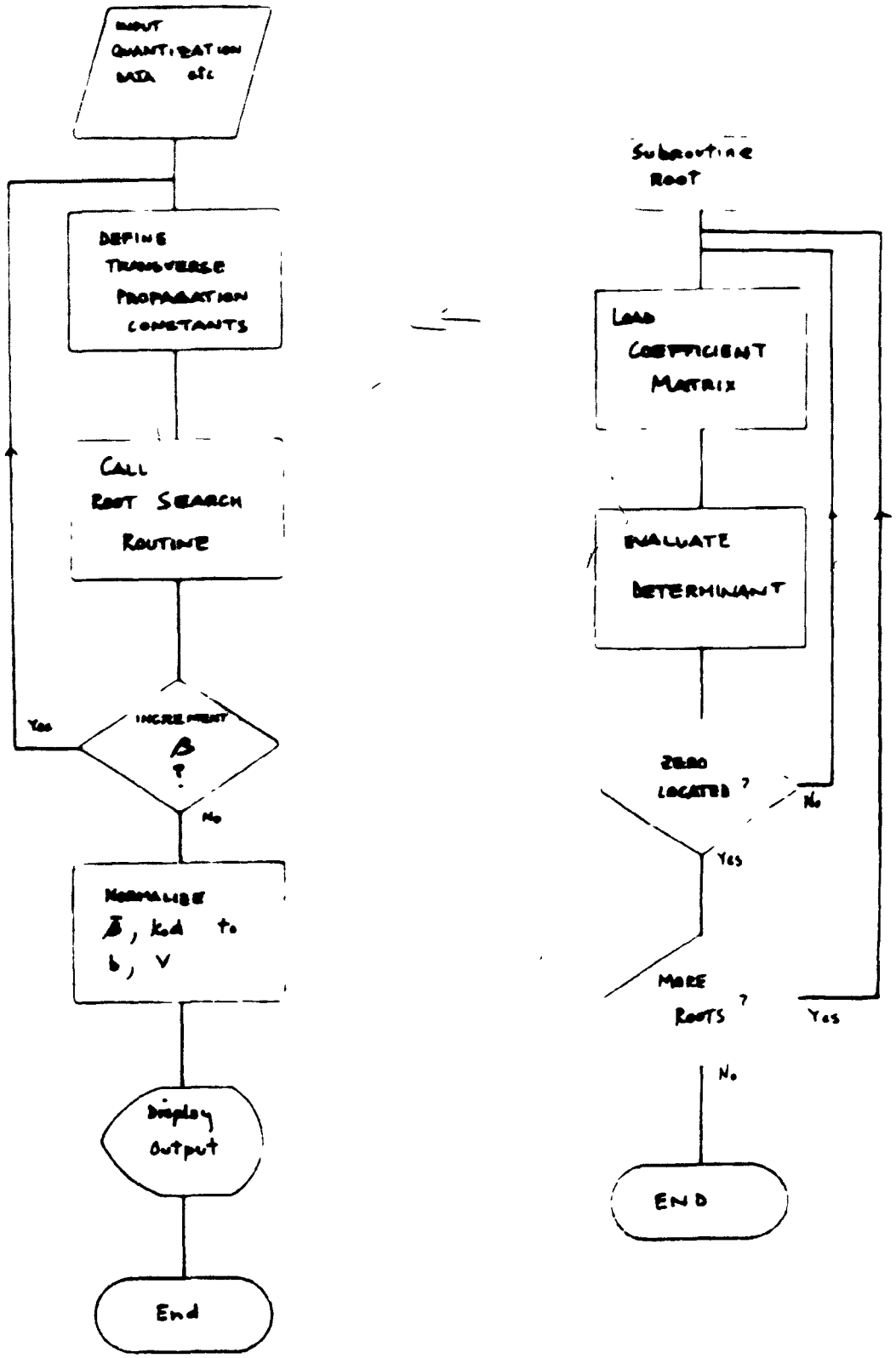

Step Approximation
Flow Chart. Figure D.1

APPENDIX E

Explanation of the "Newton Rings" Interference Pattern for location of a zero reference point

We use the Newton Rings in our laser measurement apparatus to locate the zero reference point of the prism in a precise manner. First consider the classic experiment with the lens and mirror;

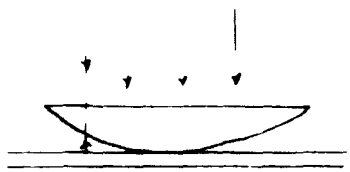

Incident light passes through the lens, strikes the mirror and upon reflection, it interferes either constructively a destructively with the incident light, depending on the phase shift incurred. Because the lens possesses a certain curvature, the path length of the reflected light varies and hence a ring pattern of dark and light fringes results.

We use this same interference phenomenon to precisely align one face of the prism such that it is perpendicular to the incident laser light. Consider the following diagram:

LASER MEASUREMENT APPARATUS

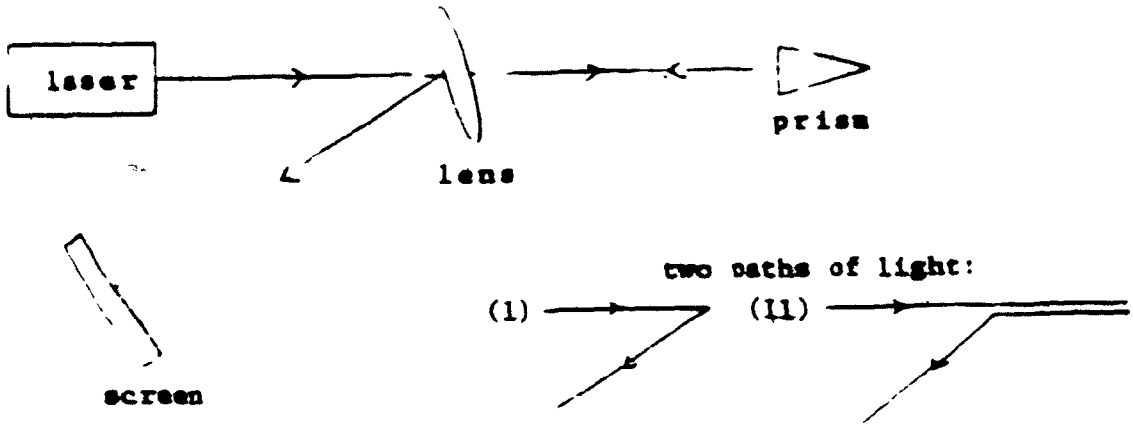

In this situation, since the wavelength of the HeNe laser is small, the prism (now acting as the mirror in the simple experiment) can be situated far from the lens while preserving the desired interference pattern. When the prism is aligned perpendicular to the incident laser light, we observed the ring interference pattern on the screen and are assured of an exact zero reference point. The photograph below illustrates the resulting ring pattern;

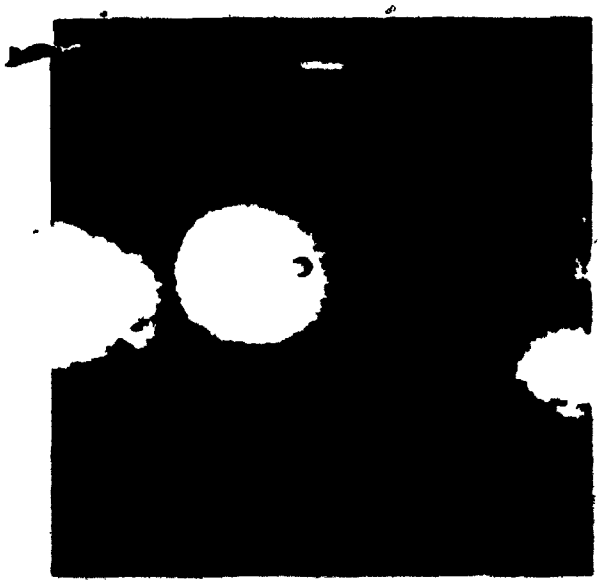

APPENDIX F

DILUTE MELT PREPARATION (Ag-Na SYSTEM)

Various diluted Ag+ melts were prepared to investigate the effect of Ag+ concentration on waveguides made by ion-exchange. As in Stewart & Laybourn (13), four melt-mode ratios were considered, and the melt preparation proceeded as follows:

capacity of boat: 22 grams $NaNO_3$

m_A : mole fraction of sodium

m_B : mole fraction of silver

To prepare a melt-mole ratio of $m_B/m_A = 0.001$, first calculate the number of moles of sodium, assuming a 22 gram base.

$$\# \text{ moles } NaNO_3 = 22(g)\ \frac{1}{85}\ \left(\frac{\text{mole}}{\text{gram}}\right) = 0.259$$

$$m_A = \frac{\#\text{moles of } NaNO_3}{\text{tot. \# of moles of all components}}$$

therefore

$$m_B/m_A = \frac{\#\text{ moles of } AgNO_3}{\#\text{ moles of } NaNO_3}$$

$$0.001 = \frac{\#\text{ moles } AgNO_3}{0.259}$$

required weight of $AgNO_3$ in grams: 0.044 g

REFERENCES

1. S.E. Miller, "Integrated Optics: An Introduction", B.S.T.J. Vol. 48, No.7, Sept. 1969.

2. E.A.J. Marcatilli, "Dielectric Rectangular Waveguide and Directional Coupler For Integrated Optics", B.S.T.J. Vol. 48, No.7, Sept. 1969.

3. J.E. Goell, "A Circular-Harmonic, Computer Analysis of Rectangular Dielectric Waveguides", B.S.T.J. Vol. 48, No.7, Sept. 1969.

4. G. Schulze, "Versche Über die Diffusion von Silber in Glas", Annalen der Physik, 40, 1913.

5. A.J. Burggraff & J. Cornelissen, "The Strengthening of Glass by Ion-Exchange", Physics and Chemistry of Glasses, Vol. 5, No.5, Oct. 1964.

6. R. H. Doremus, "Exchange and Diffusion of Ions in Glass", The Journal of Physical Chemistry, Vol. 68, No.8, Aug. 1964.

7. W.G. French & A.D. Pearson, "Refractive Index Changes Produced in Glass by Ion Exchange", Ceramic Bulletin, Vol. 49, No.11, 1970.

8. T.G. Giallorenzi, E.J. West, R. Kirk, R. Ginther, R.A. Andrews, "Optical Waveguides Formed by Thermal Migration of Ions in Glass", Applied Optics, Vol. 12, No.6, June 1973.

9. G. Stewart, C.A. Millar, P.J. Laybourne, C.D. Wilkinson, R.M. DelaRue, "Planar Optical Waveguides Formed by Silver-Ion Migration in Glass", IEEE Journal of Quantum Electronics, Vol. QE-13, No.4, April 1977.

10. C.A. Millar, R.H. Hutchins, "Manufacturing Tolerences For Silver-Sodium Ion-Exchanged Planar Optical Waveguides", Journal of Physics, D: Applied Phisics, Vol.11, 1978.

11. J. Finak, H. Jerominek, "Some Optical Properties of Planar Light Waveguides Formed by Silver-Ion Diffusion in Glass", Optica Applicata, Vol. XI, No.1, 1981.

12. G. Griffiths, P. Khan, "Analysis of Planar Optical Waveguide Fabrication by Ion Exchange in Glass", IEEE J. of Quantum Electronics, Vol. QE-17, No.4, April 1981.

13. G. Stewart, P. Laybourne, "Fabrication of Ion-Exchanged Optical Waveguides From Dilute Silver Nitrate Melts" IEEE J. of Quantum Electronics, Vol. QE-14, No.12, Dec. 1978.

14. H.J. Lilienhof, K.F. Heidemann, D. Ritter, E. Voges, "Index Profiles of Multimode Optical Strip Waveguides by Field-Enhanced Ion Exchange in Glasses", Optics Communications, Vol. 35, No. 1, Oct. 1980.

15. G.H. Chartier, P. Jaussaud, "Optical Waveguides Fabricated by Electric Field Controlled Ion Exchange in Glass", Electronics Letters, Vol. 14, No.5, March 1978.

16. G. Chartier, P. Jaussaud, A. deOliveira, O. Parriaux, "Fast Fabrication Method for Thick and Highly Multimode Optical Waveguides", Electronics Letters, Vol.13, No.25, Dec. 1977.

17. J. Crank, "The Mathematics of Diffusion", Oxford University Press, 2nd ed., 1975

18. H. Kirchoff, "The Solution of Maxwell's Equations For Inhomogeneous Dielectric Slabs", Arch Elek Übertragungstech 26,537, 1972.

19. D. Marcuse, "TE Modes of Graded Index Slab Waveguides", IEEE J. of Quantum Electronics, QE-9, 1000, 1973.

20. G.L. Yip, E. Colombini, "Analysis of an Inhomogeneous Symmetric Cladded Slab Optical Waveguide", Optical & Quantum Electronic, Vol. 10, 1978.

21. L. Brekhovskikh, "Waves in Layered Media", Academic Press, N.Y., 196

22. J. White, P. Herdrich, "Optical Waveguide Refractive Index Profiles Determined From Measurement of Mode Indices: A Simple Analysis", Applied Optics, Vol. 15, No.1, Jan. 1976.

23. B. Hocker, W. Burns, "Modes in Diffused Optical Waveguides of Arbitrary Index Profile", IEEE J. of Quantum Electronics, Vol. QE-11, No.6, June 1975.

24. T. Tamir, "Integrated Optics", Springer-Verlag, N.Y., April 1975.

25. B. Hocker, W. Burns, "Mode Dispersion in Diffused Channel Waveguides by the Effective Index Method", Applied Optics, Vol.16, No. 1, Jan. 1977.

26. B. Hocker, "Strip-Loaded Diffused Optical Waveguides", IEEE J. of Quantum Electronics, Vol QE-12, No 4, April 1976.

27. P. Simova, I. Savatinova, L. Tsonev, "Propagation Characteristics of Ag+ Ion-Exchanged Stripe Waveguides", Applied Physics, 22, 1980.

28. J. Gallagher, R. DeLaRue, "Single-Mode Stripe Optical Waveguide Formed by Silver Ion Exchange", Electronics Letters, Vol. 12, No.16, Aug. 1976.

29. S.E. Miller, "Coupled Wave Theory & Waveguide Applications" B.S.T.J , Vol. 33, No.3, May 1954.

30. M. Barnoski, "Introduction to Ingegrated Optics", Planum Press, N.Y.

31. A.S. Grove, "Physics and Technology of Semiconductor", Wiley, 1967.

32. V. Rothmund, G. Kornfeld, Z. Anorg Allgem Chem., Vol.103, p. 129, 1918.

33. F. Helfferich, "Ion Exchange", McGraw-Hill, 1962, N.Y.

34. Kuester, Chang, "Propagation, Attenuation & Dispersion Characteristics of Inhomogeneous Dielectric Slab Waveguides", IEEE Trans. on MTT 98, 1975.

35. E. Conwell, "WKB Approximation For Optical Guided Modes in a Medium with Exponentially Varying Index" J. Applied Physics, Vol. 46, 1975.

36 Gallagher, Phd Thesis, The University, Glasgow, 1977

37. R. Hornbeck, "Numerical Methods", Quantum Publishers, N.Y., p. 150.

38. P.K. Tien, App Optics, Vol 10, p 2395, Nov 1971

39 Knox, Toulios, "Proceedings of the MRI Symposium on Submillimeter Waves", Polytechnique Press, Brooklyn, N.Y , 1970.

40. Kogelnik, Ramaswamy, "Scaling Rules For Thin Film Optical Waveguides", App. Optics, Vol. 13, 1974.

41 M. Haruna, J. Koyama "Thermooptic Deflection and Switching in Glass", App Optics, Vol. 21, No. 19, 1982.